Title

Autophagosome development and chloroplast segmentation occur synchronously for piecemeal degradation of chloroplasts

Authors

Masanori Izumi[a,b,1], Sakuya Nakamura[a], Kohei Otomo[c,d,e,f,g], Hiroyuki Ishida[h], Jun Hidema[i], Tomomi Nemoto[c,d,e,f], Shinya Hagihara[a],

Affiliations

[a]Center for Sustainable Resource Science (CSRS), RIKEN, 351-0198 Wako, Japan
[b]Frontier Research Institute for Interdisciplinary Sciences (FRIS), Tohoku University, 980-8578 Sendai, Japan
[c]Exploratory Research Center on Life and Living Systems (ExCELLs), National Institutes of Natural Sciences, 444-8787 Okazaki, Japan
[d]National Institute for Physiological Sciences, National Institutes of Natural Sciences, 444-8787 Okazaki, Japan
[e]The Graduate University for Advanced Studies (SOKENDAI), 444-8787 Okazaki, Japan
[f]Research Institute for Electronic Science, Hokkaido University, 001-0020 Sapporo, Japan
[g]Graduate School of Medicine, Juntendo University, 113-8421 Tokyo, Japan
[h]Graduate School of Agricultural Science, Tohoku University, 980-8572 Sendai, Japan
[i]Graduate School of Life Sciences, Tohoku University, 980-8577 Sendai, Japan
[1]Address correspondence to: masanori.izumi@riken.jp

Author contributions

M.I. conceived the study. M.I. performed biochemical assays. M.I., K.O, and T.N. performed two-photon excitation microscopy observations. M.I., S.N., H.I., J.H., and S.H. performed confocal microscopy studies. M.I. wrote the manuscript with the support of all authors.

Funding

This work was supported, in part, by KAKENHI (grant numbers JP16H06280, JP18H04852, JP20H04916 to M.I., JP20H05352, JP22H04660 to S.N., JP22H04627 to H.I.), the Cooperative Research Program of "NJRC Mater. & Dev." (to M.I.), and the Joint Research by Exploratory Research Center on Life and Living Systems (ExCELLS program number 20-314 to M.I.).

Abstract

Plants distribute many nutrients to chloroplasts during leaf development and maturation. When leaves senesce or experience sugar starvation, the autophagy machinery degrades chloroplast proteins to facilitate efficient nutrient reuse. Here, we report on the intracellular dynamics of an autophagy pathway responsible for piecemeal degradation of chloroplast components. Through live-cell monitoring of chloroplast morphology, we observed the formation of chloroplast budding structures in sugar-starved leaves. These buds were then released and incorporated into the vacuolar lumen as an autophagic cargo termed a Rubisco-containing body. The budding structures did not accumulate in mutants of core autophagy machinery, suggesting that autophagosome creation is required for forming chloroplast buds. Simultaneous tracking of chloroplast morphology and autophagosome development revealed that the isolation membranes of autophagosomes interact closely with part of the chloroplast surface before forming chloroplast buds. Chloroplasts then protrude at the site associated with the isolation membranes, which divide synchronously with autophagosome maturation. This autophagy-related division does not require DYNAMIN-RELATED PROTEIN 5B, which constitutes the division ring for chloroplast proliferation in growing leaves. An unidentified division machinery may thus fragment chloroplasts for degradation in coordination with the development of the chloroplast-associated isolation membrane.

Introduction

Organelle morphology changes dynamically in response to fluctuations in cell functions, developmental stages, and environmental cues. Plastids are plant-specific organelles that differentiate into chloroplasts in green tissues to perform photosynthesis. Plastids further serve as hubs for metabolic pathways such as the biosynthesis of amino acids and plant hormones. Dynamic changes in plastid morphology also act as switches initiating biological programs (Osteryoung and Pyke, 2014). For instance, chloroplasts in leaf pavement cells form stroma-filled tubular extensions termed stromules to activate programmed cell death as an immune response upon perception of an invading pathogen, in a process regulated by the plant hormone salicylic acid (SA) (Caplan et al., 2015). Stromules are thin, tubular structures of plastid stroma less than 1 μm in diameter (Hanson and Sattarzadeh, 2011).

Leaf aging is closely associated with morphological and functional changes of plastids. At the early stage of leaf development, the undifferentiated form of plastids, termed proplastids, are converted to green chloroplasts as their population expands through active division. In Arabidopsis (*Arabidopsis thaliana*), the coordination of cytoplasmic ring structures comprising DYNAMIN-RELATED PROTEIN 5B (DRP5B), also called ACCUMULATION AND REPLICATION OF CHLOROPLASTS 5 (ARC5), and intrachloroplastic ring structures consisting of FILAMENTING TEMPERATURE-SENSITIVE Z (FTSZ) proteins mediates chloroplast division (Chen et al., 2018). In mature leaves, spherical chloroplasts occupy almost all of the cytoplasm and manifest high photosynthetic activity. When older leaves later senesce, the size and number of chloroplasts gradually decrease (Martinoia et al., 1983; Mae et al., 1984). Younger leaves closer to the shoot apex sometimes shade older leaves beneath them, thus perturbing photosynthesis by decreasing the amount of light reaching those leaves and causing local sugar starvation. In such sugar-starved leaves, senescence is accelerated to facilitate the relocation of nutrients into newly developing tissues (Weaver and Amasino, 2001; Ono et al., 2013; Law et al., 2018). Autophagy is an intracellular degradation machinery that contributes to the decline in chloroplast volume and numbers during leaf senescence (Wada et al., 2009).

Autophagy is a ubiquitous mechanism that transports cytoplasmic components to the vacuolar/lysosomal compartment for degradation in eukaryotic cells. The major autophagy pathway known as macroautophagy, or simply autophagy, begins with the assembly of a membrane termed the isolation membrane (also known as a phagophore) that forms a double-membrane structure termed the autophagosome and sequesters a portion of the cytoplasm. Core AUTOPHAGY (ATG) proteins (ATG1–10, 12–14, 16, and 18) are highly conserved among plants, yeasts, and mammals (Yoshimoto and Ohsumi, 2018; Nakamura et al., 2021a) and are required for the initiation and elongation of the isolation membrane (Nakatogawa, 2020). The outer membrane of autophagosomes fuses with the vacuolar/lysosomal membrane, resulting in the formation of autophagic bodies whose cargos are digested by vacuolar/lysosomal hydrolases. Our previous studies identified two types of autophagy for chloroplast degradation in mature leaves (Ishida et al., 2014; Nakamura and Izumi, 2018). Senescence and sugar starvation preferentially activate piecemeal degradation of chloroplast components involving a specific type of autophagosomal cargo termed a Rubisco-containing body (RCB), leading to smaller chloroplasts (Ishida et al., 2008; Wada et al., 2009; Izumi et al., 2015). The second type of autophagy, termed chlorophagy, removes entire unnecessary chloroplasts (Izumi et al., 2017; Nakamura et al., 2018), thereby modulating the number of chloroplasts in a cell (Wada et al., 2009; Izumi et al., 2017). Chlorophagy is likely another type of autophagy, termed microautophagy, during which the vacuolar membrane directly participates in sequestering the degradation target in the absence of encapsulation by autophagosomes (Nakamura et al., 2017; Lee et al., 2023).

Mitochondria are another type of energy-producing organelle derived from endosymbiosis. Dynamin-related proteins (DRPs) also mediate mitochondrial division (Giacomello et al., 2020); the involvement of DRP-mediated organelle division in

mitochondrion-targeted autophagy—termed mitophagy—in mammals and budding yeast (*Saccharomyces cerevisiae*) has been under debate (Chen et al., 2022). Drp1 and Dnm1 (Dynamin-related 1) participate in mitochondrial fission in mammals and budding yeast, respectively. Previous studies have suggested that segmented mitochondria resulting from Drp1/Dnm1-mediated fission become a target for degradation by autophagosomes (Twig et al., 2008; Rambold et al., 2011; Abeliovich et al., 2013). Notably, Drp1/Dnm1-independent mitophagy has also been observed (Yamashita et al., 2016), whereby mitochondrial division occurs concomitantly with the development of the mitochondrion-associated isolation membrane, forming an autophagosome that specifically contains mitochondrial components termed the mitophagosome. A recent study identified the mitochondrial intermembrane-space protein mitofissin (also called Atg44), required for mitochondrial fission during yeast mitophagy (Fukuda et al., 2023).

Plant autophagic bodies and RCBs are typically around 1 μm in diameter (Chiba et al., 2003; Yoshimoto et al., 2004), which is smaller than chloroplasts. Thus, piecemeal-type chloroplast autophagy via RCBs must start with division of the chloroplast segments that are to be degraded. However, how a fragment of a chloroplast can be transported to the vacuole remains poorly understood. Here, to characterize the underlying intracellular dynamics, we performed high-resolution imaging analyses in living cells of Arabidopsis leaves. We used time-lapse microscopy to observe the segmentation of chloroplast budding structures and their transport to the vacuolar lumen. Use of multiple organelle markers revealed that the development of the chloroplast-associated isolation membrane and the formation of RCBs occur simultaneously. These morphological changes did not correspond to the emergence of stromules or to DRP5b-mediated chloroplast division. Therefore, a previously undescribed chloroplast division machinery may be in play during chloroplast autophagy.

Results

Chloroplast budding structures containing stroma and envelope are released in response to sugar starvation

To observe the intracellular dynamics of the piecemeal-type of chloroplast autophagy, we subjected the mature leaves of Arabidopsis plants to incubation in darkness, as this treatment induces sugar starvation and accelerates leaf senescence, thus activating the RCB-mediated chloroplast autophagy (Izumi et al., 2010). Exogenous application of concanamycin A (concA), an inhibitor of vacuolar H^+-ATPase, allows the vacuolar accumulation of autophagic cargos, including RCBs, facilitating their visualization (Yoshimoto et al., 2004; Ishida et al., 2008). Following the excision and incubation in darkness of leaves harboring chloroplast stroma–targeted fluorescent protein markers such as RUBISCO SMALL SUBUNIT (RBCS) fused to monomeric red fluorescent protein (mRFP) in the presence of concA, we observed the accumulation of many small puncta containing the RBCS-mRFP signal in the vacuole, i.e., RCBs (Figure 1–figure supplement 1A and 1C). Although co-incubation of dark-treated leaves with concA and mineral nutrient–rich Murashige and Skoog (MS) salts did not block the RCB accumulation, the addition of sucrose did, by rescuing the sugar-starved leaf (Figure 1–figure supplement 1A and 1C). We detected no RCBs when we subjected the leaves of a mutant for the core *ATG* gene *ATG7* to dark incubation in sucrose-free solution (Figure 1–figure supplement 1B and 1C). These observations indicate that RCBs are a type of autophagic cargo involved in the degradation of chloroplast fragments in response to sugar starvation. Therefore, in this study, we monitored chloroplast morphology in sugar-starved leaves resulting from their incubation in darkness in a sugar-free solution.

We wished to monitor the changes in the three-dimensional (3D) morphology of chloroplasts during autophagic degradation of chloroplast fragments. We thus used a two-photon excitation microscope equipped with a confocal spinning-disk unit (Otomo et al., 2015),

Fig. 1

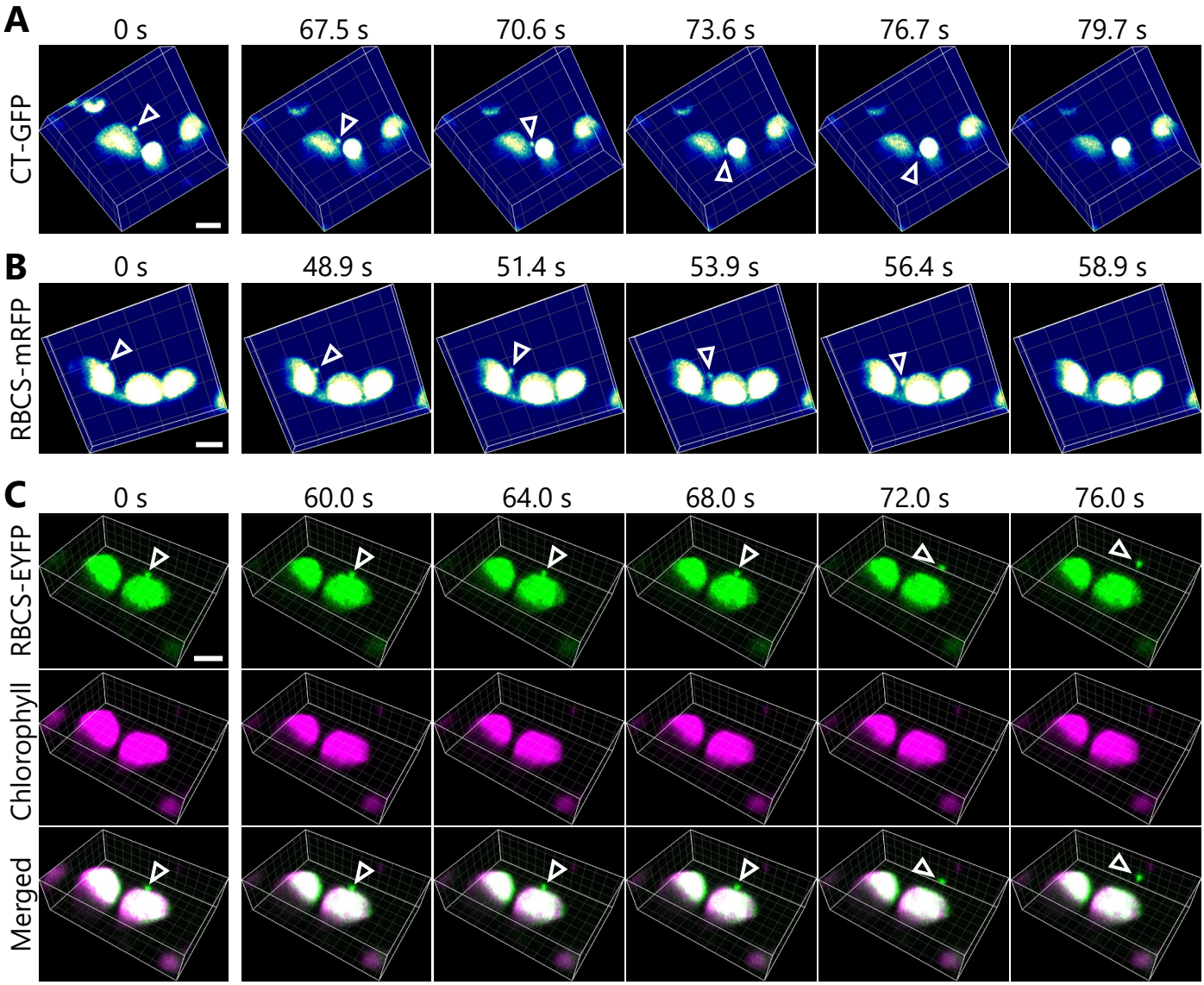

Figure 1. Chloroplast buds are released in sugar-starved leaves.
Time-lapse observations of 3D-reconstructed chloroplast morphology in Arabidopsis mesophyll cells accumulating chloroplast stroma–targeted fluorescent markers. A leaf from a plant accumulating chloroplast stroma–targeted GFP (CT-GFP) (A), RBCS-mRFP (B), or RBCS-EYFP (C) was incubated in sugar-free solution in darkness for 5 h from dawn (A), 21 h (B), or 24 h from the period in light (C) and then observed through a two-photon excitation microscope equipped with a confocal spinning-disk unit. Second rosette leaves from 20- to 22-d-old plants were used. Images in (A–C) are still frames from Videos 1, 2, and 3, respectively. Time scales above the images indicate the elapsed time from the start of the respective videos. Arrowheads indicate chloroplast budding structures. Scale bars, 5 µm. In (C), green, RBCS-EYFP; magenta, chlorophyll fluorescence. In the merged images, the overlapping regions of RBCS-EYFP and chlorophyll signals appear white.

Figure 1-figure supplement 1

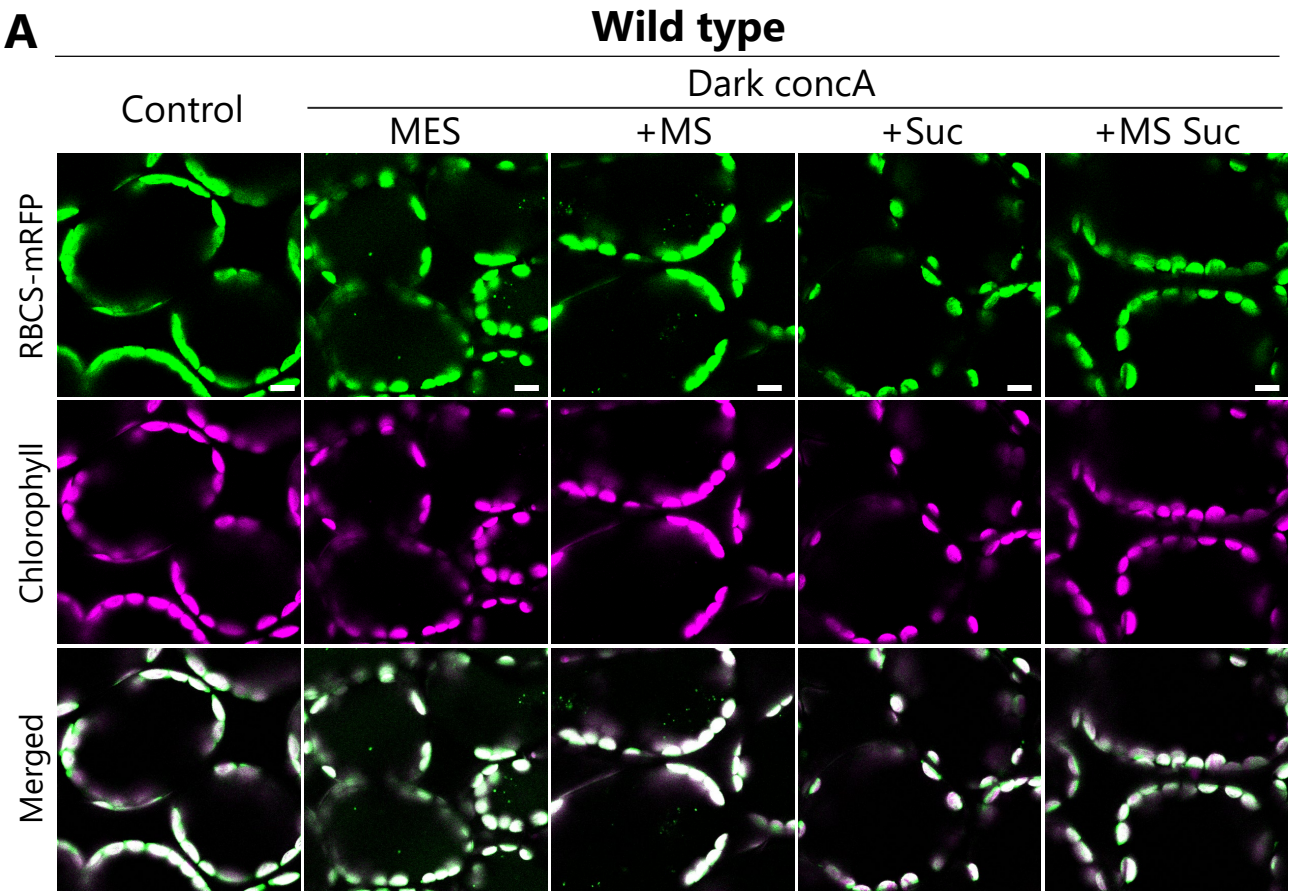

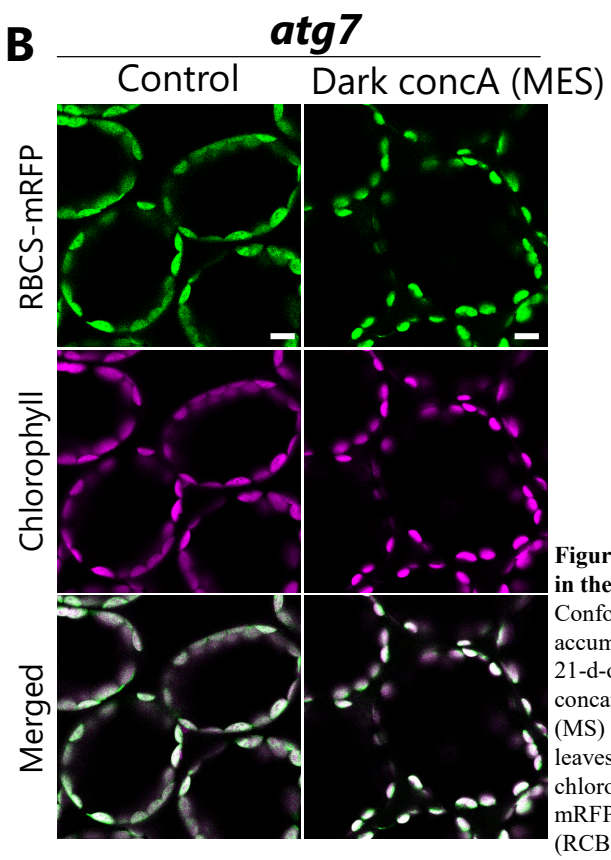

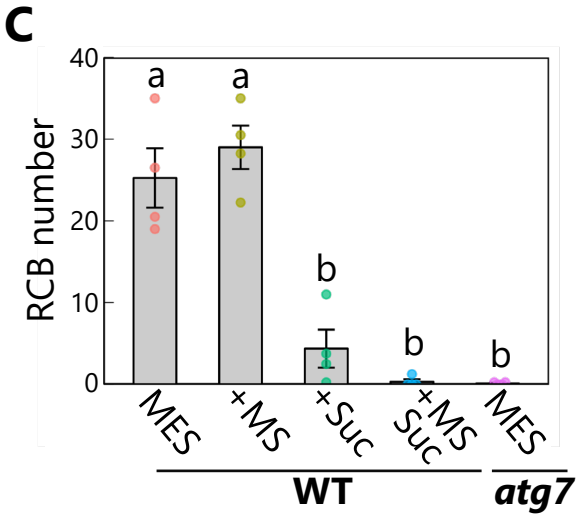

Figure 1–figure supplement 1. Accumulation of chloroplast stroma components in the vacuole via autophagy.

Confocal images of mesophyll cells from wild-type (A) or *atg7* (B) plants accumulating the chloroplast stroma marker RBCS-mRFP. Second rosette leaves of 21-d-old plants were excised and incubated in 10 mM MES-NaOH containing 1 μM concanamycin A (concA) in darkness for 1 d. Sucrose (Suc) or Murashige and Skoog (MS) salts were added as an energy or nutrient source, respectively. Second rosette leaves from nontreated plants are shown as control. Green, RBCS-mRFP; magenta, chlorophyll fluorescence. Scale bars, 10 μm. The small puncta containing RBCS-mRFP without chlorophyll signal appear green and are Rubisco-containing bodies (RCBs) in the vacuole. (C) Number of accumulated RCBs from the observations described in (A) and (B). Different lowercase letters denote significant differences based on Tukey's test ($P < 0.05$). Values are means ± SE ($n = 4$). Dots represent individual data points.

Figure 1-figure supplement 2

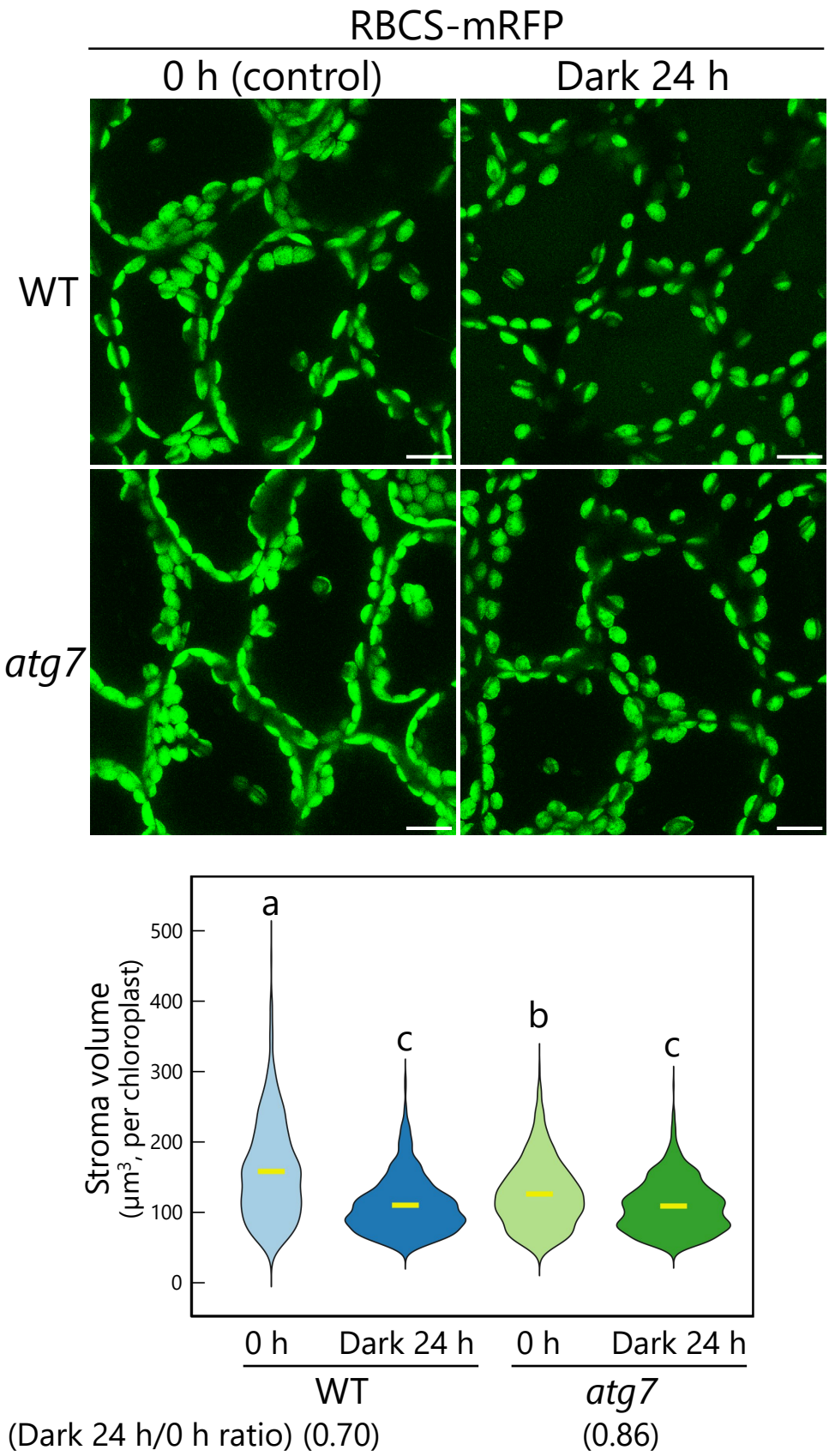

Figure 1–figure supplement 2. The release of chloroplast buds by autophagy contributes to the decline in chloroplast stroma volume. (A) Orthogonal projections produced from *z*-stack images (30 μm in depth) of mesophyll cells from WT or *atg7* leaves accumulating the chloroplast stroma marker RBCS-mRFP. Second rosette leaves of 21-d-old plants were excised at dawn and incubated in 10 mM MES-NaOH in the dark for 24 h. Mesophyll cells were observed before (0 h) and after (Dark 24 h) the treatment. Green, RBCS-mRFP. Scale bars, 10 μm. (B) Violin plot showing the volume of chloroplast stroma labeled by RBCS-mRFP, measured from the observations described in (A). Different lowercase letters denote significant differences based on Tukey's test ($P < 0.05$). Yellow bars indicate mean values. Five individual plants were observed, and the volumes of 564 (WT, 0 h), 554 (WT, dark 24 h), 597 (*atg7*, 0 h), and 725 (*atg7*, dark 24 h) chloroplasts were scored.

which facilitates the monitoring of changes in the 3D cellular structures of living plant cells (Sasaki et al., 2019; Nakamura et al., 2021b). Using dark-incubated leaves from transgenic plants harboring chloroplast-targeted *GFP* (*CT-GFP*) or *RBCS-mRFP* transgenes, we determined that mesophyll chloroplasts form a type of budding structure containing stromal components (Figure 1A and 1B, arrowheads). We observed these structures budding off from their associated chloroplasts within a few minutes (Figure 1A and 1B, Videos 1 and 2). Dual detection of the chloroplast stromal marker RBCS fused to enhanced yellow fluorescent protein (RBCS-EYFP) and of chlorophyll autofluorescence confirmed that the budding structure specifically contained stroma material (EYFP positive) without any chlorophyll signal, a marker of thylakoid membrane (Figure 1C, Video 3). These time-lapse observations reveal that chloroplasts form budding structures that are released in sugar-starved leaves. The chloroplast buds are cytoplasmic spherical bodies (approximately 0.5 to 1.5 μm in diameter) that are labeled by a chloroplast stroma marker and are adjacent to a main chloroplast body.

To estimate the impact of the release of chloroplast buds on the decline in chloroplast volume, we measured the volume of RBCS-mRFP signals in wild-type (WT) and *atg7* leaves before and after incubation in the dark for 24 h (Figure 1–figure supplement 2). Chloroplasts accumulate starch during the day and consume most of this starch during the night (Smith and Stitt, 2007). To minimize the effects of starch metabolism on the changes in chloroplast volume, we began sugar starvation treatment at the end of the night when a major portion of the starch has been consumed. After the treatment, stroma volume decreased in both genotypes (Figure 1–figure supplement 2B). However, the decline in volume was smaller in *atg7* leaves (14%) than in WT leaves (30%). The vacuolar transport of chloroplast budding structures as RCBs did not occur in *atg7* leaves (Figure 1–figure supplement 1). These results suggest that the release of chloroplast buds contributes to the decrease in chloroplast stroma volume in sugar-starved leaves.

We then performed a simultaneous detection of three organelle markers using conventional confocal microscopes to determine if the chloroplast buds contained membrane-bound proteins. Accordingly, we incubated leaves from plants accumulating the chloroplast outer envelope marker TRANSLOCON AT THE OUTER MEMBRANE OF CHLOROPLASTS 64 (TOC64) fused to mRFP and the stromal marker RBCS-GFP in darkness as described above. Under these conditions, we observed TOC64-mRFP signal surrounding a chloroplast bud (Figure 2A, arrowheads, Figure 2–figure supplement 1A). We then monitored chloroplasts in leaves accumulating the chloroplast inner envelope membrane protein K^+ EFFLUX ANTIPORTER 1 (KEA1) fused to mRFP along with RBCS-GFP after dark incubation. The chloroplast buds contained KEA1-mRFP signal but no chlorophyll signal (Figure 2–figure supplement 1B). We also captured the transport of an RCB with TOC64-mRFP or KEA1-mRFP signal (Figure 2B, Video 4, Figure 2–figure supplement 2, Video 5). These results indicate that the budding structures contained chloroplast envelope components. In another set of experiments, we generated transgenic plants accumulating the thylakoid membrane marker ATP synthase gamma subunit (ATPC1) fused to tagRFP and stromal RBCS-GFP. The ATPC1-tagRFP fluorescent signal fully overlapped with that of chlorophyll autofluorescence, with both originating from the thylakoid membrane (Figure 2C and 2D). In the chloroplast budding structures, however, we detected no ATPC1-tagRFP signal, in contrast to the strong stromal RBCS-GFP signal (Figure 2C, arrowheads, Figure 2–figure supplement 1C). In agreement with this observation, we captured a released RCB that did not contain any ATPC1-tagRFP or chlorophyll signals, but accumulated plentiful RBCS-GFP (Figure 2D, Video 6). These observations support the notion that the chloroplast buds containing stromal and envelope proteins are released as RCBs without thylakoid membranes. These live-cell imaging results are consistent with an immuno-electron microscopy study of RCBs in wheat (*Triticum aestivum*) leaves (Chiba et al., 2003).

Fig. 2

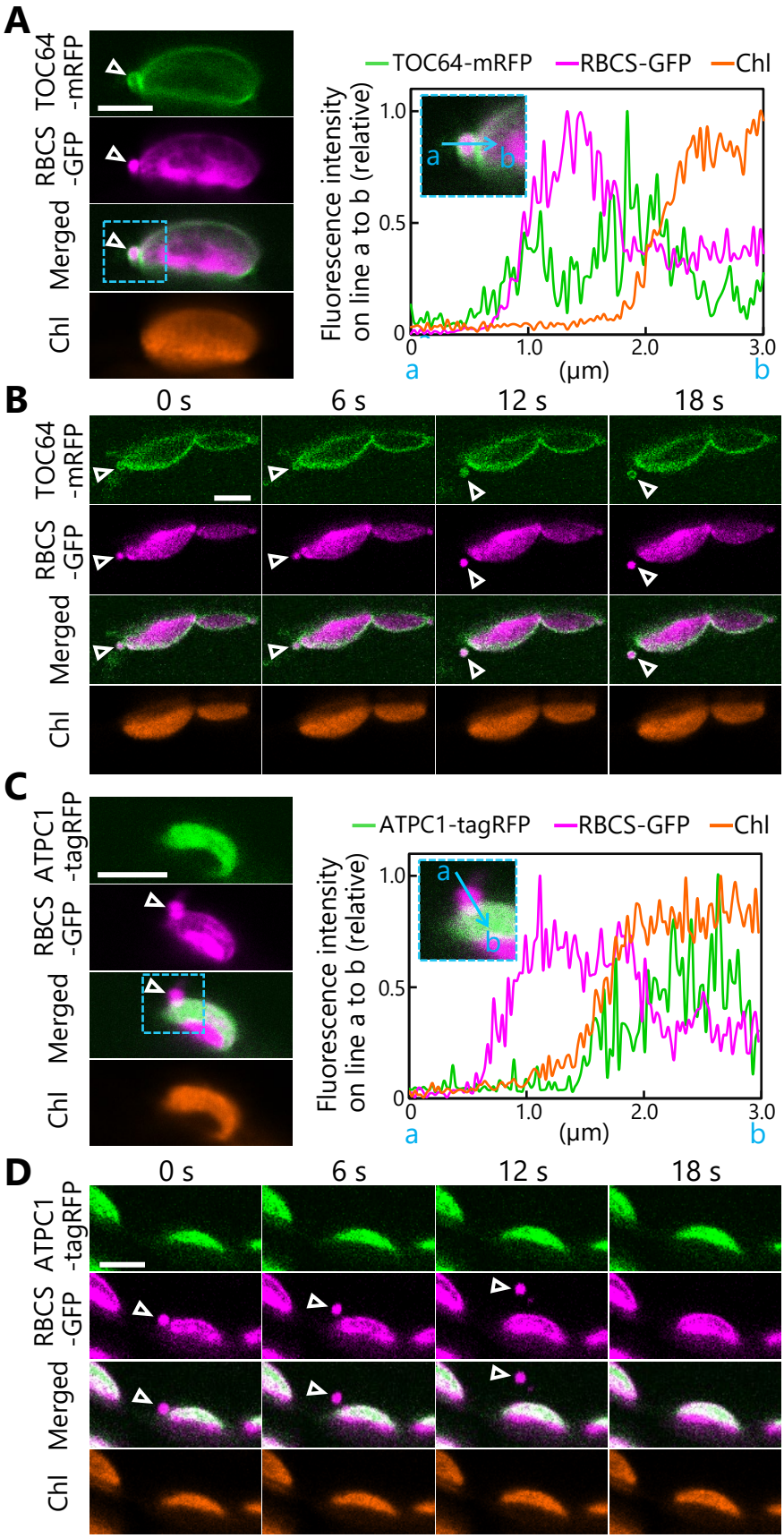

Figure 2. Chloroplast buds containing stroma and envelope components are released from the chloroplasts.

Time-lapse observations of Arabidopsis mesophyll cells accumulating the chloroplast stroma marker along with an envelope marker or a thylakoid membrane marker. Leaves accumulating stromal RBCS-GFP along with outer envelope–bound TOC64-mRFP (A and B) or with thylakoid membrane–bound ATPC1-tagRFP (C and D) were incubated in sugar-free solution in darkness for 5 to 9 h from dawn and then observed. Second rosette leaves from 21- to 22-d-old plants were used. Images in (B) or (D) are still frames from Videos 4 and 6, respectively. Time scales above the images indicate the elapsed time from the start of the respective videos. Arrowheads indicate chloroplast budding structures. Scale bars, 5 μm. Green, TOC64-mRFP or ATPC1-tagRFP; magenta, RBCS-GFP; orange, chlorophyll (Chl) fluorescence. The graphs in (A and C) show fluorescence intensities along the blue lines (a to b) in the magnified images of the area indicated by dashed blue boxes. The intensities are shown relative to the maximum intensity for each fluorescence channel, set to 1.

Figure 2-figure supplement 1

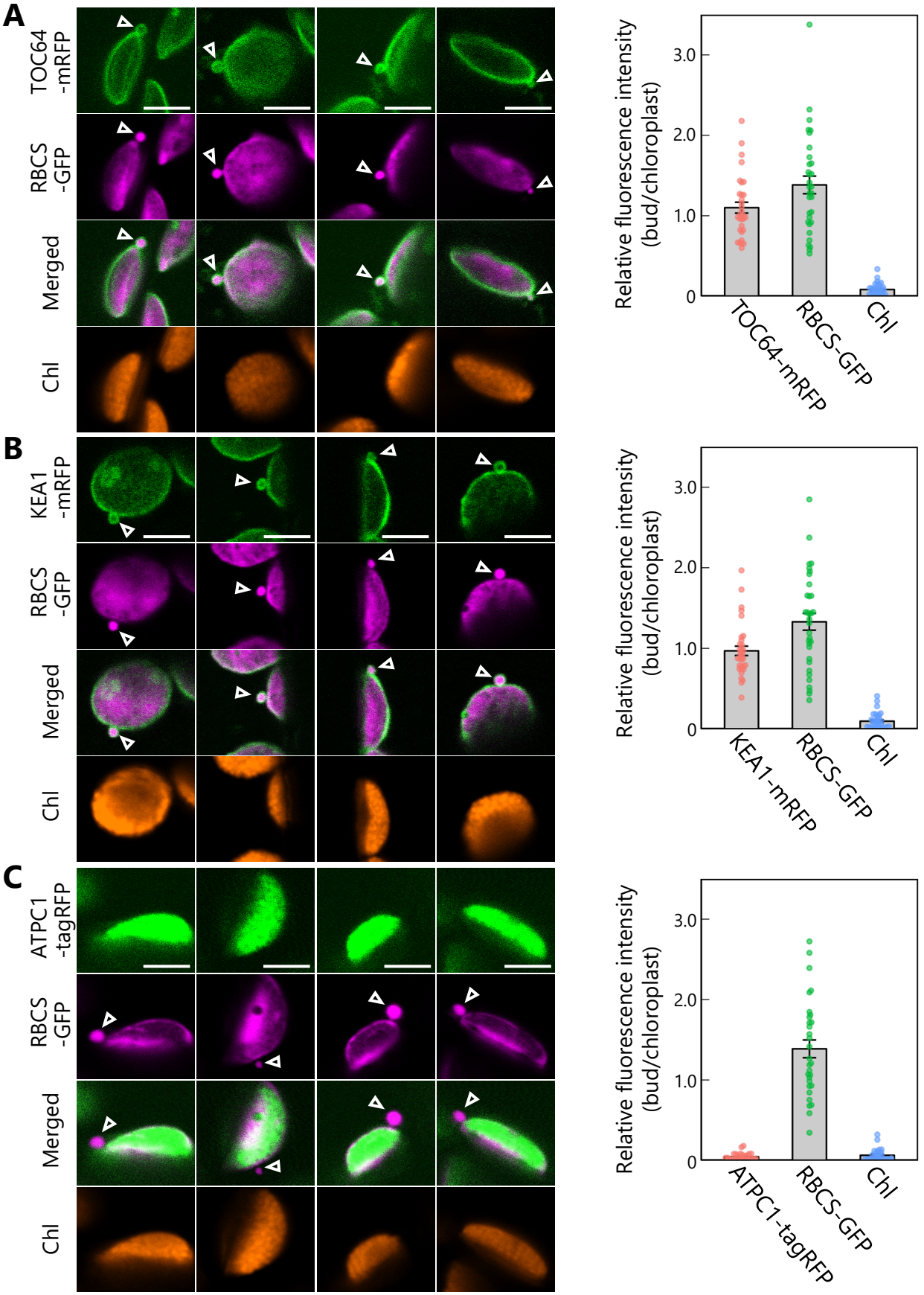

Figure 2–figure supplement 1. Chloroplast buds contain stroma and envelope proteins.
Second rosette leaves accumulating stromal RBCS-GFP along with outer envelope membrane–bound TOC64-mRFP (A), inner envelope membrane–bound KEA1-mRFP (B), or thylakoid membrane–bound ATPC1-tagRFP (C) were incubated in sugar-free solution in the dark for 5 to 9 h from dawn, and chloroplast budding structures were observed. Second rosette leaves from 21- to 22-d-old plants were used. Arrowheads indicate chloroplast budding structures. Four representative images of chloroplast buds are shown for each plant line. Scale bars, 5 µm. Green, TOC64-mRFP, KEA1-mRFP, or ATPC1-tagRFP; magenta, RBCS-GFP; orange, chlorophyll (Chl) fluorescence. The graphs show the relative ratio of GFP, RFP, or chlorophyll fluorescence intensity per unit area within chloroplast budding structures vs. their neighboring chloroplasts (bud/chloroplast). The intensities from 33 (A), 32 (B), or 30 (C) chloroplast buds from 8 individual plants were measured. Values are means ± SE (n = 30–33). Dots represent individual data points in each graph.

Figure 2-figure supplement 2

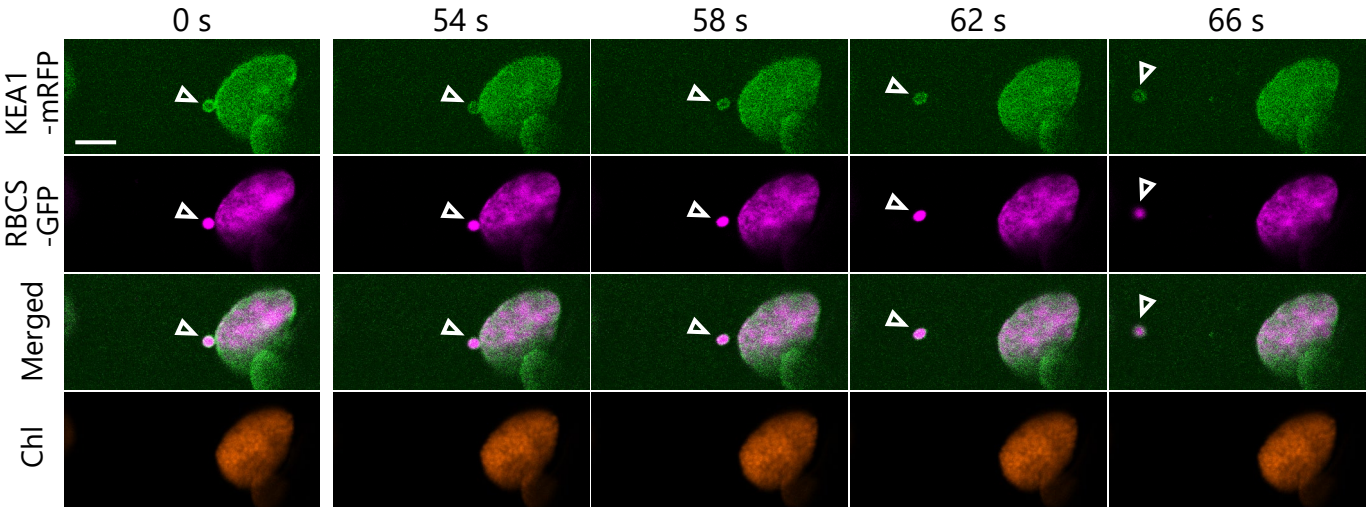

Figure 2–figure supplement 2. A released chloroplast bud contains an inner envelope marker protein.
Time-lapse observations of Arabidopsis mesophyll cells accumulating the chloroplast stroma marker RBCS-GFP along with inner envelope membrane–bound KEA1-mRFP. The second rosette leaf from a 22-d-old plant was incubated in sugar-free solution in the dark for 6 h from dawn and observed. The images are still frames from Video 5. Time scales above the images indicate the elapsed time from the start of the video. Arrowheads indicate chloroplast budding structures. Scale bars, 5 µm. Green, KEA1-mRFP; magenta, RBCS-GFP; orange, chlorophyll (Chl) fluorescence.

The vacuolar membrane dynamically interacts with chloroplast stromal components to incorporate them into the vacuolar lumen

We tracked the trafficking of RCBs in mesophyll cells further and obtained a two-dimensional (2D) sequential series of images of the release and transport of an RCB in leaves accumulating stromal CT-GFP (Figure 3A, Video 7). This time series included two phases during which the punctum moved quickly (Figure 3B, 24.4–34.8 s and 73.8–90.5 s). A tracking analysis for the RCB indicated that during the early phase (24.4–34.8 s), the punctum moved rather smoothly in one general direction (Figure 3C, Video 7); however, during the later phase (73.8–90.5 s), the punctum appeared to move more randomly, akin to Brownian movement (Figure 3C, Video 7). Other tracking series of dark-incubated leaves accumulating RBCS-tagRFP or RBCS-EYFP also showed RCBs starting to exhibit random movement: after 185 s in Figure 3–figure supplement 1A (Video 8) or after 25 s in Figure 3–figure supplement 1B (Video 9). Previous studies showed that autophagic bodies accumulating into the vacuolar lumen exhibit such random movements (Ishida et al., 2008). We thus reasoned that the incorporation of RCBs into the vacuolar lumen from the cytoplasm takes place when these structures start to exhibit random movement.

We therefore turned our attention to the dynamics of the vacuolar membrane when it is incorporating RCBs into the vacuolar lumen in transgenic plants accumulating the vacuolar membrane marker VACUOLAR H^+-PYROPHOSPHATASE 1 (VHP1) fused to mGFP (Segami et al., 2014) along with the stromal marker RBCS-mRFP (Figure 4). From one of our time-lapse imaging series, we identified still frames of an RCB present in the cytoplasm being engulfed by the vacuolar membrane (Figure 4A, open arrowheads from 25.4–30.5 s, Video 10). Later in the time series, we observed the opening of the part of the vacuolar membrane that had engulfed the RCB, resulting in the RCB being released into the vacuolar lumen (Figure 4A, filled arrowheads from 47.0–52.0 s, Video 10). We captured another instance of the dynamics of the vacuolar membrane in another time series, with the vacuolar membrane first surrounding the RCB (52.6–57.4 s) before releasing it (65.3–72.9 s) into the vacuolar lumen (Figure 4B, Video 11). Figure 4–figure supplement 1 and Videos 12–14 show similar membrane dynamics that were observed in three individual plants. An RCB marked by RBCS-mRFP was engulfed by the vacuolar membrane at 48.0–54.0 s (Figure 4–figure supplement 1A, Video 12), 6.0–15.0 s (Figure 4–figure supplement 1B, Video 13), and 111.0–123.0 s (Figure 4–figure supplement 1C, Video 14). The RCBs were then released into the vacuolar lumen. Our time-lapse imaging approach thus allowed us to successfully visualize the cytoplasm-to-vacuole transport progression of chloroplast stroma material via autophagy.

Formation and segmentation of chloroplast buds occur simultaneously with autophagosome maturation

Based on the observation of spherical structures budding off from chloroplasts (Figures 1–3), we hypothesized that these structures are formed in response to sugar starvation and are subsequently recognized and sequestered by the autophagosomal membranes. We thus expected the leaves of autophagy-deficient mutants to accumulate multiple extended structures of chloroplast stroma as chloroplast protrusions upon exposure to sugar starvation. This hypothesis seemed consistent with the observations of stromule-rich cells in hypocotyls or dark-incubated leaves of autophagy-deficient *atg5* or *atg7* mutants, compared with non-mutants (Ishida et al., 2008; Spitzer et al., 2015), assuming that the accumulation of chloroplast protrusions precedes stromule formation in *atg* mutants. To test this hypothesis, we subjected the leaves of *atg5* and *atg7* mutants, each defective in the function of a core ATG protein, to darkness-induced sugar starvation and treatment with concA for 1 d (Figure 5). We then evaluated the appearance of RCBs and chloroplast protrusions comprising extended structures of chloroplast stroma labeled by RBCS-mRFP, approximately 0.5 to 1.5 μm long. We detected no RCB in the leaves of either mutant (Figure 5A and 5B); however, in both the WT and the mutants, we noticed fewer chloroplast protrusions in dark-incubated leaves treated with concA compared with the

Fig. 3

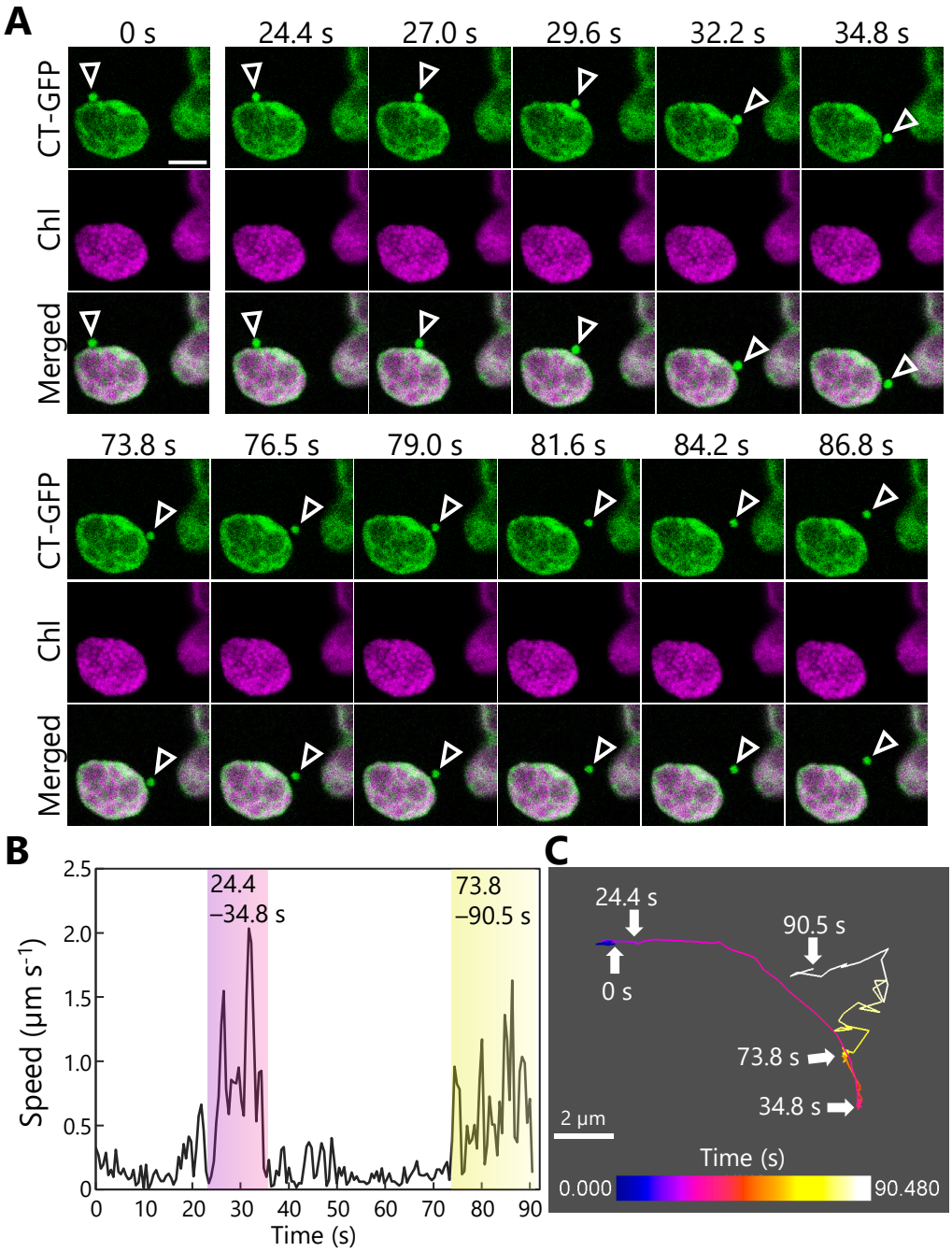

Figure 3. Tracking the transport of a Rubisco-containing body.
A leaf accumulating chloroplast stroma–targeted GFP (CT-GFP) was incubated in sugar-free solution in darkness for 6 h from dawn, and the transport of a Rubisco-containing body (RCB) was tracked. The second rosette leaf from a 21-d-old plant was used. (A) Confocal images during the periods when the RCB moved quickly (24.4–34.8 and 73.8–90.5 s). Arrowheads indicate an RCB. The images are still frames from Video 7. Time scales above the images indicate the elapsed time from the start of the video. Green, CT-GFP; magenta, chlorophyll (Chl) fluorescence. Scale bar, 5 μm. (B) Calculated speed of the tracked RCB in (A). (C) The track of the RCB. The color of the track line changes over time, as indicated by the color bar. Scale bar, 2 μm.

Figure 3-figure supplement 1

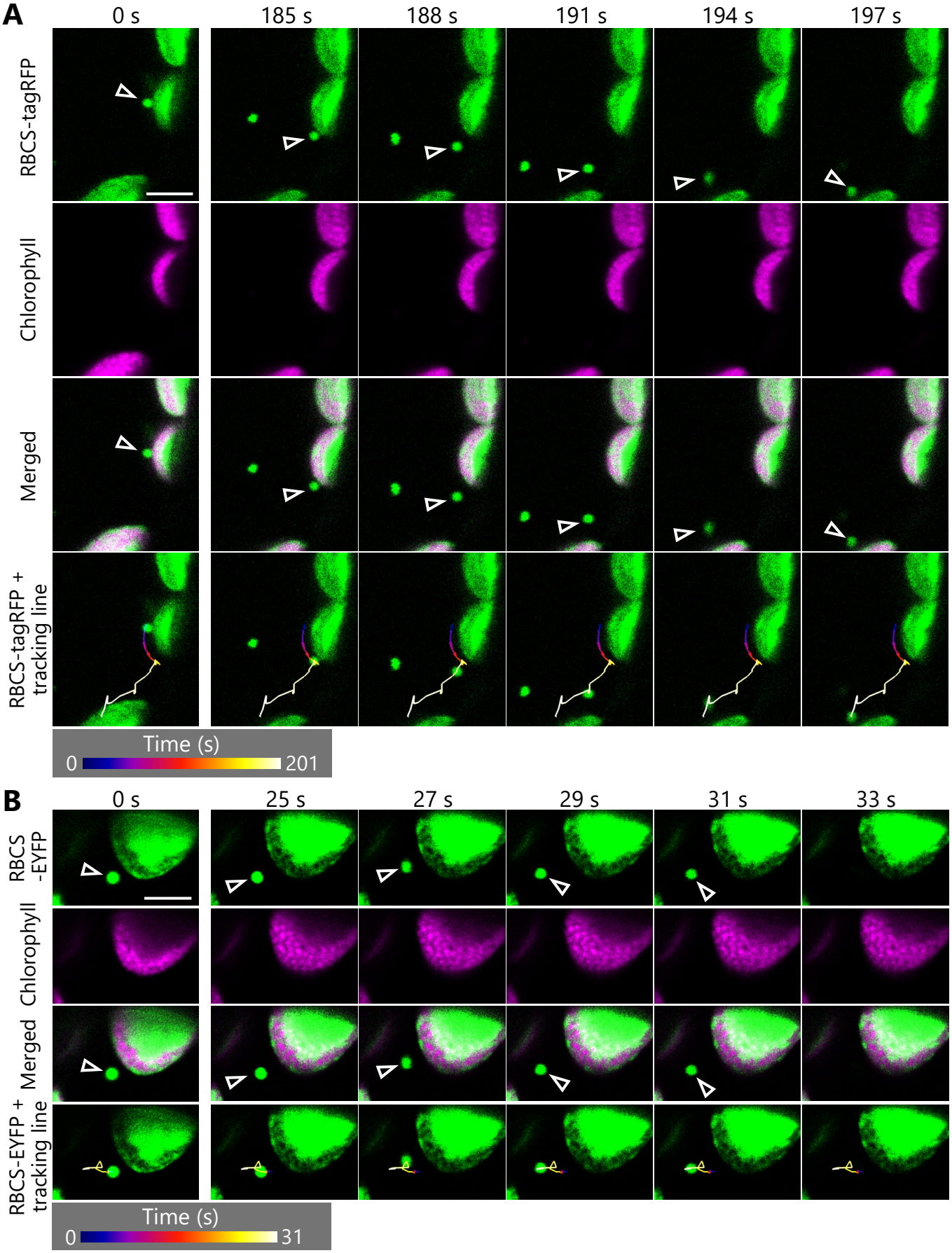

Figure 3–figure supplement 1. Rubisco-containing bodies appear to begin random movement during their tracking.
A leaf accumulating RBCS-tagRFP (A) or RBCS-EYFP (B) was incubated in sugar-free solution in the dark for 7 to 8 h from dawn, and the transport of a Rubisco-containing body was tracked. Second rosette leaves from 22-d-old plants were used. Arrowheads indicate a tracked RCB. The images are still frames from Videos 8 (A) or 9 (B), respectively. The images show the time when RCBs appeared to begin random movement (185–197 s in A or 25–33 s in B). Time scales above the images indicate the elapsed time from the start of the respective videos. Green, RBCS-tagRFP or RBCS-EYFP; magenta, chlorophyll fluorescence. Scale bars, 5 µm. The color of the track line changes over time, as indicated by the color bars below the images.

Fig. 4

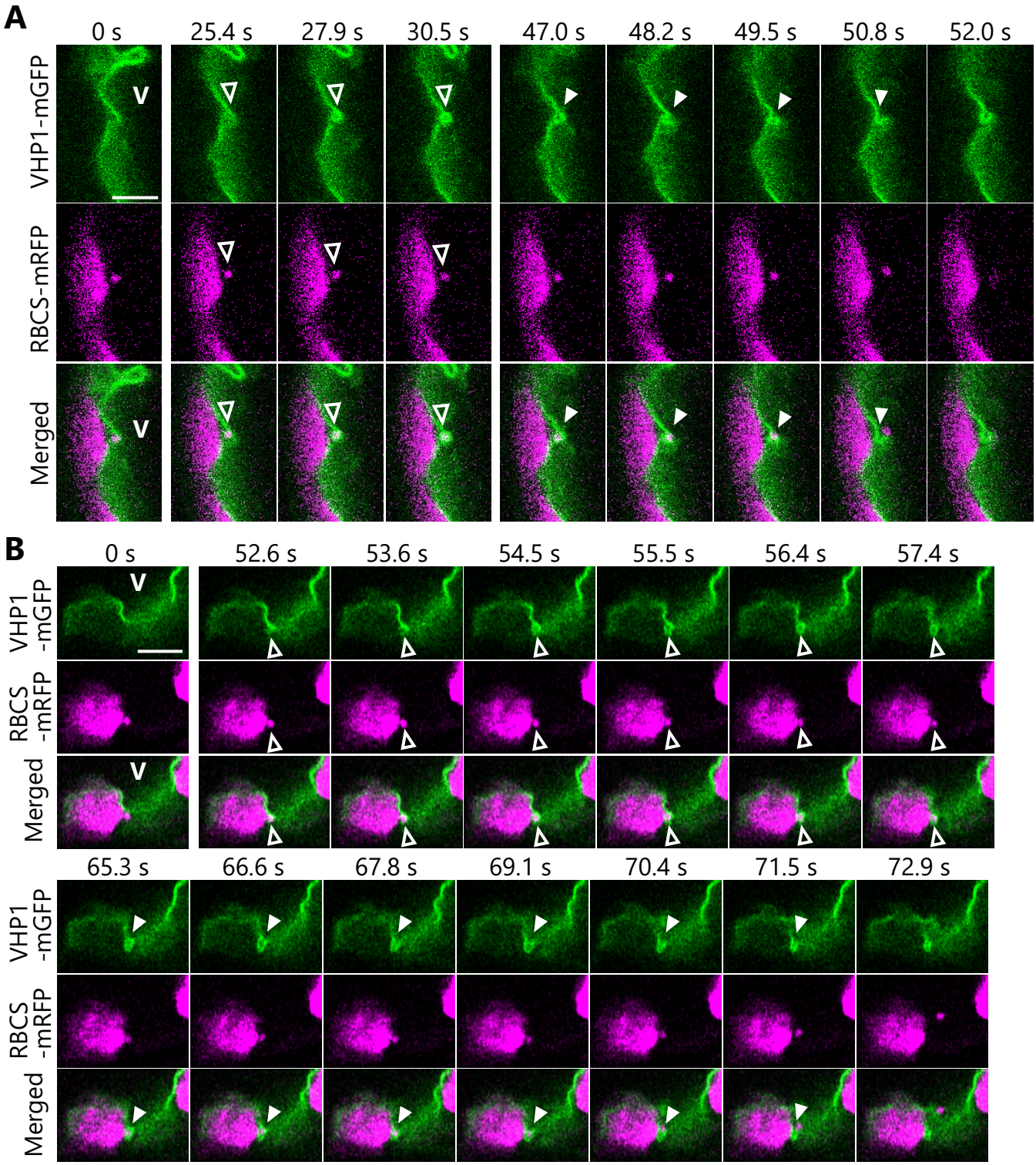

Figure 4. Dynamics of the vacuolar membrane during the incorporation of Rubisco-containing bodies.
Leaves accumulating the chloroplast stroma marker RBCS-mRFP along with the vacuolar membrane marker VHP1-mGFP were incubated in sugar-free solution in darkness for 6 to 8 h from dawn, and the behavior of cytosolic RCBs was monitored. Second rosette leaves from 21- or 23-d-old plants were used. The images when the vacuolar membrane engulfs an RCB (25.4–30.5 s in A and 52.6–57.4 s in B) and when an RCB is incorporated into the vacuolar lumen (47.0–52.0 s in A and 65.3–72.9 s in B) are shown. The images in (A) and (B) are still frames from Videos 10 and 11, respectively. Time scales above the images indicate the elapsed time from the start of the respective videos. Open arrowheads indicate an RCB engulfed by the vacuolar membrane. Closed arrowheads indicate the open site of the vacuolar membrane for the incorporation of an RCB. V indicates the region of the vacuolar lumen. Green, VHP1-mGFP; magenta, RBCS-mRFP. Scale bars, 5 µm.

Figure 4-figure supplement 1

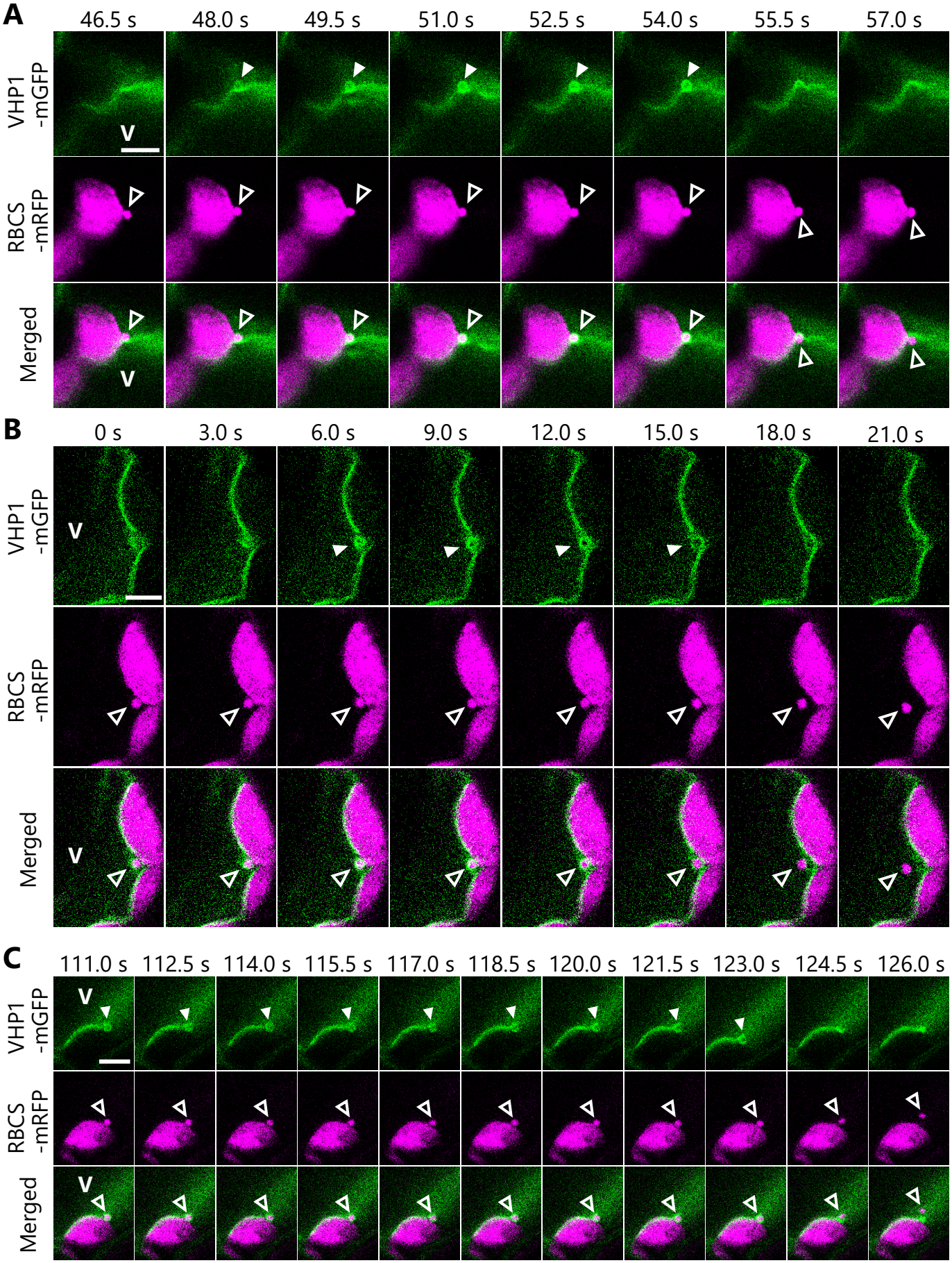

Figure 4–figure supplement 1. Additional observations of the incorporation of Rubisco-containing bodies into the vacuolar lumen. Additional time-lapse data of the experiments described in Figure 4. The second rosette leaves from 21- (A) or 24-d-old (B, C) plants were used. The images in (A), (B), and (C) are still frames from Videos 12, 13, and 14, respectively. Time scales above the images indicate the elapsed time from the start of the respective videos. Open arrowheads indicate an RCB engulfed by the vacuolar membrane. Closed arrowheads indicate the vacuolar membrane structure that engulfs an RCB. V indicates the region of the vacuolar lumen. Green, VHP1-mGFP; magenta, RBCS-mRFP. Scale bars, 5 μm.

Fig. 5

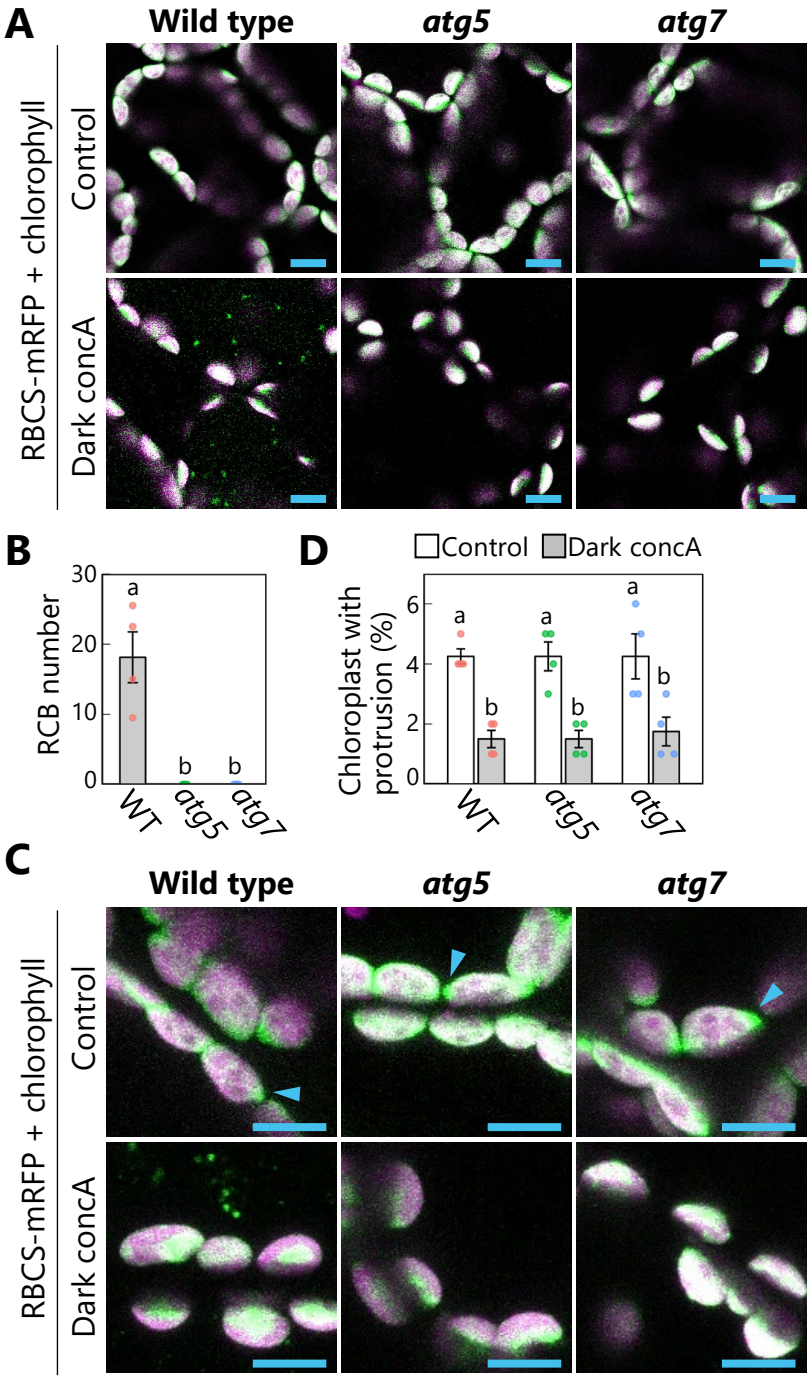

Figure 5. Autophagy deficiency does not increase the number of chloroplast protrusions during a 1-d dark treatment.
Leaves from wild-type (WT), *atg5*, or *atg7* plants accumulating the chloroplast stroma marker RBCS-mRFP were incubated in sugar-free solution containing 1 µM concanamycin A (concA) for 1 d in darkness. Second rosette leaves from 21-d-old plants were used. 2D images of mesophyll cells were acquired (A), and the number of accumulated RCBs in the vacuoles was scored (B). Small puncta containing RBCS-mRFP without the chlorophyll signal appear green and are RCBs in the vacuole. Leaves from untreated plants are shown as control. The appearance of chloroplast protrusions was observed from orthogonal projections created from *z*-stack images (15 µm in depth; C), and the proportion of chloroplasts forming protrusion structures out of 50 chloroplasts was scored (D). Scale bars, 10 µm. Green, RBCS-mRFP; magenta, chlorophyll fluorescence. Only the merged channels are shown. The overlapping regions of RBCS-mRFP and chlorophyll signals appear white. Arrowheads indicate the structures that were counted as a chloroplast protrusion in (D). Different lowercase letters denote significant differences based on Tukey's test ($P < 0.05$). Values are means ± SE ($n = 4$). Dots represent individual data points in each graph.

Figure 5-figure supplement 1

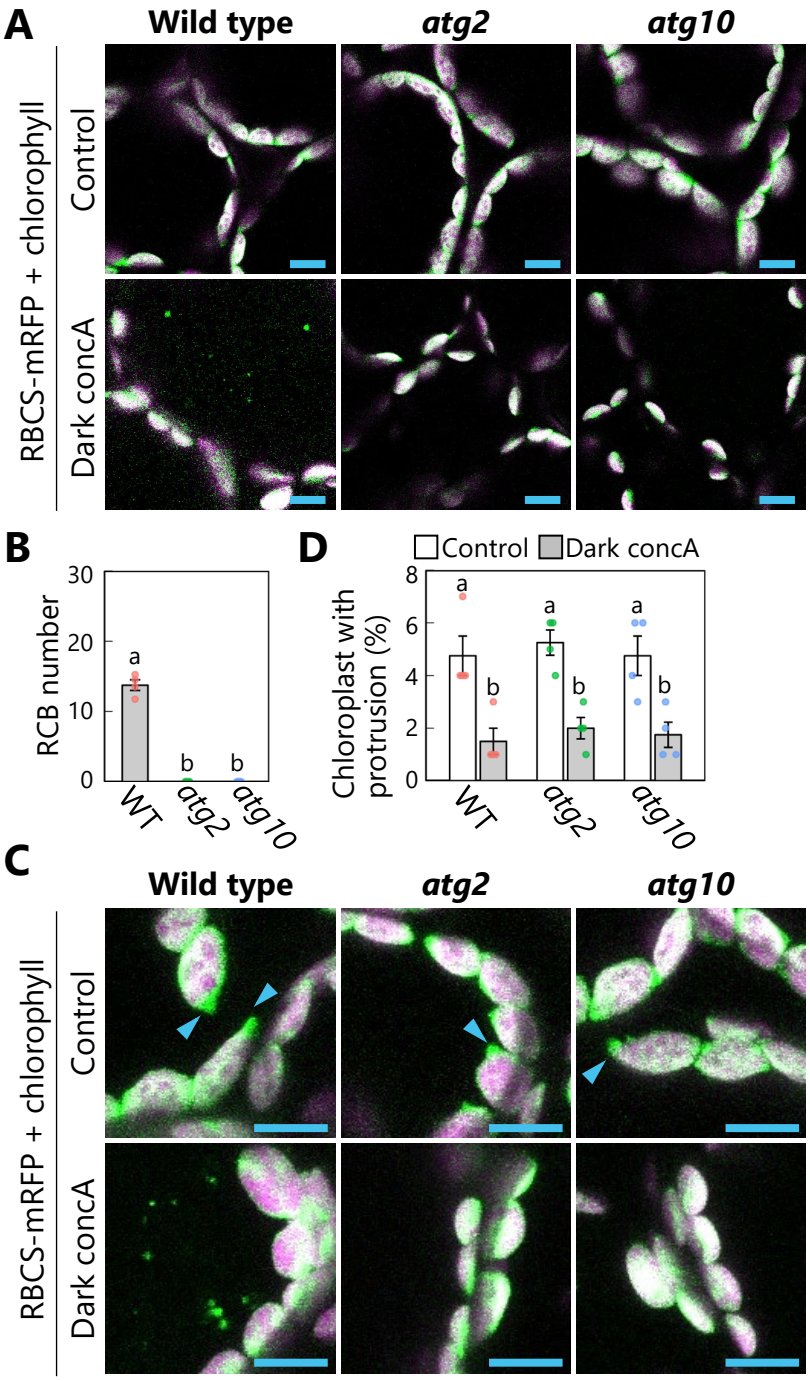

Figure 5–figure supplement 1. Chloroplast protrusions do not increase in *atg2* or *atg10* mutant leaves during a 1-d dark treatment. The experiments described in Figure 5 were performed on leaves from wild-type (WT), *atg2*, or *atg10* plants accumulating the chloroplast stroma marker RBCS-mRFP. Scale bars, 10 µm. Green, RBCS-mRFP; magenta, chlorophyll fluorescence. Only the merged channels are shown. The overlapping regions of RBCS-mRFP and chlorophyll signals appear white. Small puncta containing RBCS-mRFP without chlorophyll signal appear green and are RCBs in the vacuole. Arrowheads indicate the structures that were counted as a chloroplast protrusion in (D). Different lowercase letters denote significant differences based on Tukey's test ($P < 0.05$). Values are means ± SE ($n = 4$). Dots represent individual data points in each graph.

respective untreated control leaves, contrary to our hypothesis (Figure 5C and 5D). We checked single mutants of *ATG2* and *ATG10* (*atg2* and *atg10*) to investigate other core ATGs and obtained similar results (Figure 5–figure supplement 1): The number of chloroplast protrusions did not increase in *atg2* or *atg10* leaves during a 1-d incubation in darkness.

We therefore posited that autophagosome formation might be required for the production of chloroplast buds. To test this idea, we observed the behavior of autophagosomes in transgenic plants accumulating the isolation membrane marker AUTOPHAGY8a (ATG8a) fused to GFP (as GFP-ATG8a) along with stromal RBCS-mRFP or chloroplast stroma–targeted (CT)-DsRed (Figure 6). Following incubation of leaves in darkness and confocal microscopy observation, we observed isolation membranes (marked by GFP-ATG8a) that were tightly associated with the chloroplast surface before any budding structure was visible (Figure 6A and 6B, 0 s). Over time, however, fluorescence monitoring of the same area revealed that the isolation membrane–associated site from the chloroplast side gradually protruded and eventually formed a spherical body containing RBCS-mRFP or CT-DsRed and surrounded by GFP-ATG8a signal, i.e., an autophagosome containing an RCB (Figure 6A and 6B, arrowheads; Videos 15 and 16).

Using the time-series data shown in Figure 6B (Video 16), we evaluated the time-dependent changes of the size of the chloroplast bud and the ratio between the major axis and the minor axis of the GFP-ATG8a-labeled autophagosome (Figure 6C). This ratio dropped to 1 as the isolation membrane became a spherical autophagosome. During this observation period, the ratio between the major and minor axes started to decrease at around 40 s and approached 1 at around 100 s. The chloroplast budding structure appeared at around 50 s and gradually increased in size until around 120 s. These data support the notion that the chloroplast bud appears as the isolation membrane develops and becomes a segmented RCB when the spherical autophagosome forms. We identified another example in an independent image series (Figure 6–figure supplement 1, Video 17) where the ratio between the major and minor axes of the isolation membrane started to decrease at approximately 40 s and the chloroplast bud appeared at around 50 s. In the third set of images, we observed the formation of chloroplast buds and later of RCBs near GFP-ATG8a-associated sites on multiple chloroplasts and sequentially (Figure 6–figure supplement 2, Video 18). Therefore, we conclude that the development of the chloroplast-associated isolation membrane precedes the production of chloroplast buds and of RCBs for piecemeal-type chloroplast autophagy.

We then evaluated the proportion of chloroplast buds associated with GFP-ATG8a signal when leaves accumulating RBCS-mRFP and GFP-ATG8a were incubated in the dark for 5 to 9 h from the end of night (Figure 6–figure supplement 3). Of the chloroplast buds examined, 64% were GFP-ATG8a positive (Figure 6–figure supplement 3A–3C). The formation of GFP-ATG8a-labeled chloroplast buds increased in response to the dark treatment (Figure 6–figure supplement 3D), but the buds did not appear in leaves from *atg7* plants exposed to dark treatment (Figure 6–figure supplement 3E). Therefore, a large portion of chloroplast buds may form synchronously with the development of the isolation membrane under sugar-starvation treatment. We then turned our attention to the isolation membrane and evaluated the proportion of GFP-ATG8a-labeled structures associated with chloroplasts (Figure 6–figure supplement 4). Of the isolation membranes examined, 23% localized on the chloroplast surface as flattened structures (Figure 6–figure supplement 4A and 4D), and 20% localized with chloroplast buds as spherical or curved structures (Figure 6–figure supplement 4B and 4D). Therefore, 43% of the GFP-ATG8a-labeled structures participated in chloroplast degradation during the dark treatment in this study. These results support the notion that chloroplast budding accompanied by autophagosome development substantially contributes to the degradation of chloroplast components in sugar-starved leaves.

Fig. 6

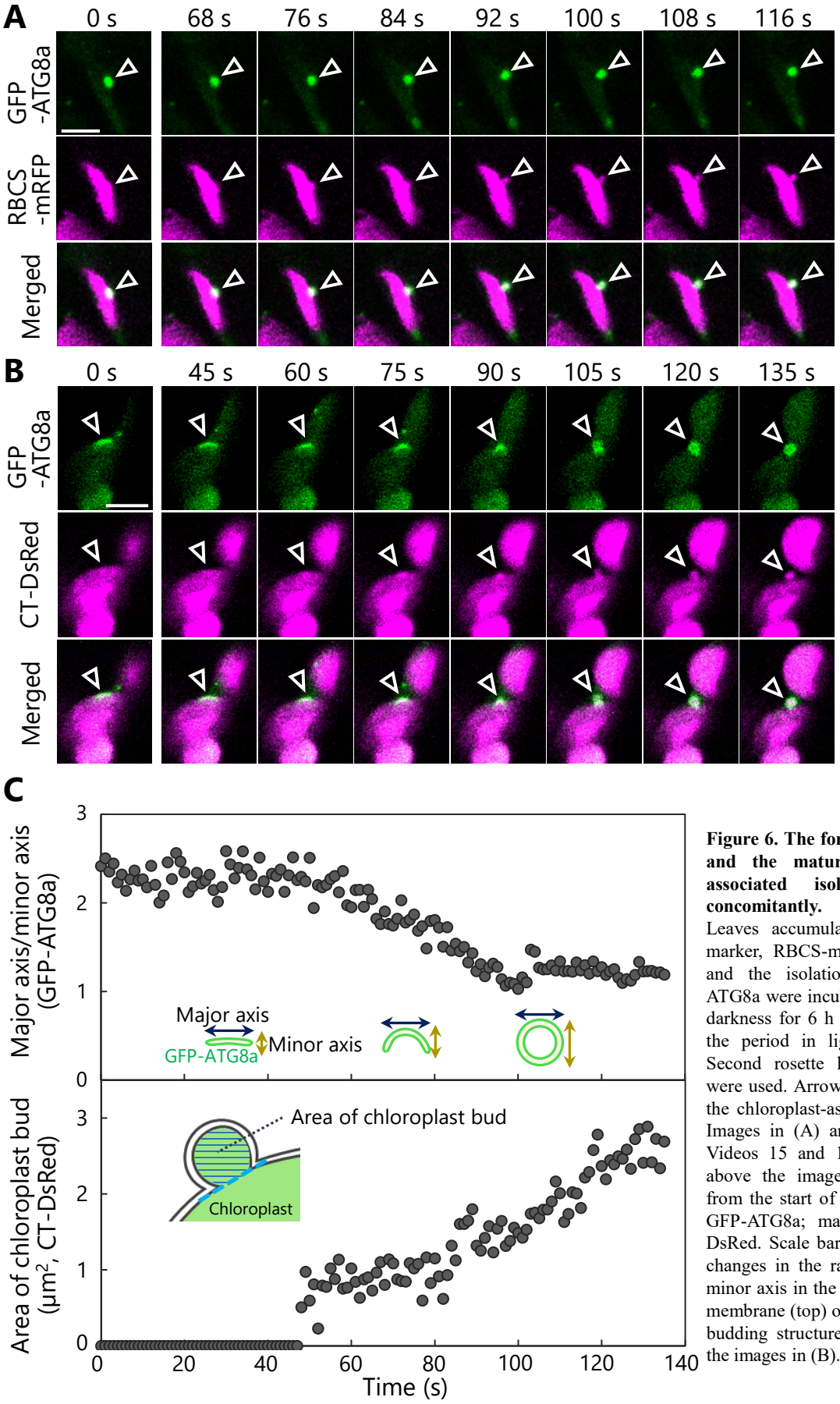

Figure 6. The formation of a chloroplast bud and the maturation of the chloroplast-associated isolation membrane occur concomitantly.

Leaves accumulating the chloroplast stroma marker, RBCS-mRFP (A) or CT-DsRed (B), and the isolation membrane marker GFP-ATG8a were incubated in sugar-free solution in darkness for 6 h from dawn (A) or 21 h from the period in light (B) and then observed. Second rosette leaves from 23-d-old plants were used. Arrowheads indicate the position of the chloroplast-associated isolation membrane. Images in (A) and (B) are still frames from Videos 15 and 16, respectively. Time scales above the images indicate the elapsed time from the start of the respective videos. Green, GFP-ATG8a; magenta, RBCS-mRFP or CT-DsRed. Scale bars, 5 μm. (C) Time-dependent changes in the ratio of the major axis to the minor axis in the GFP-ATG8a-labeled isolation membrane (top) or in the area of the chloroplast budding structure (bottom) as measured from the images in (B).

Figure 6-figure supplement 1

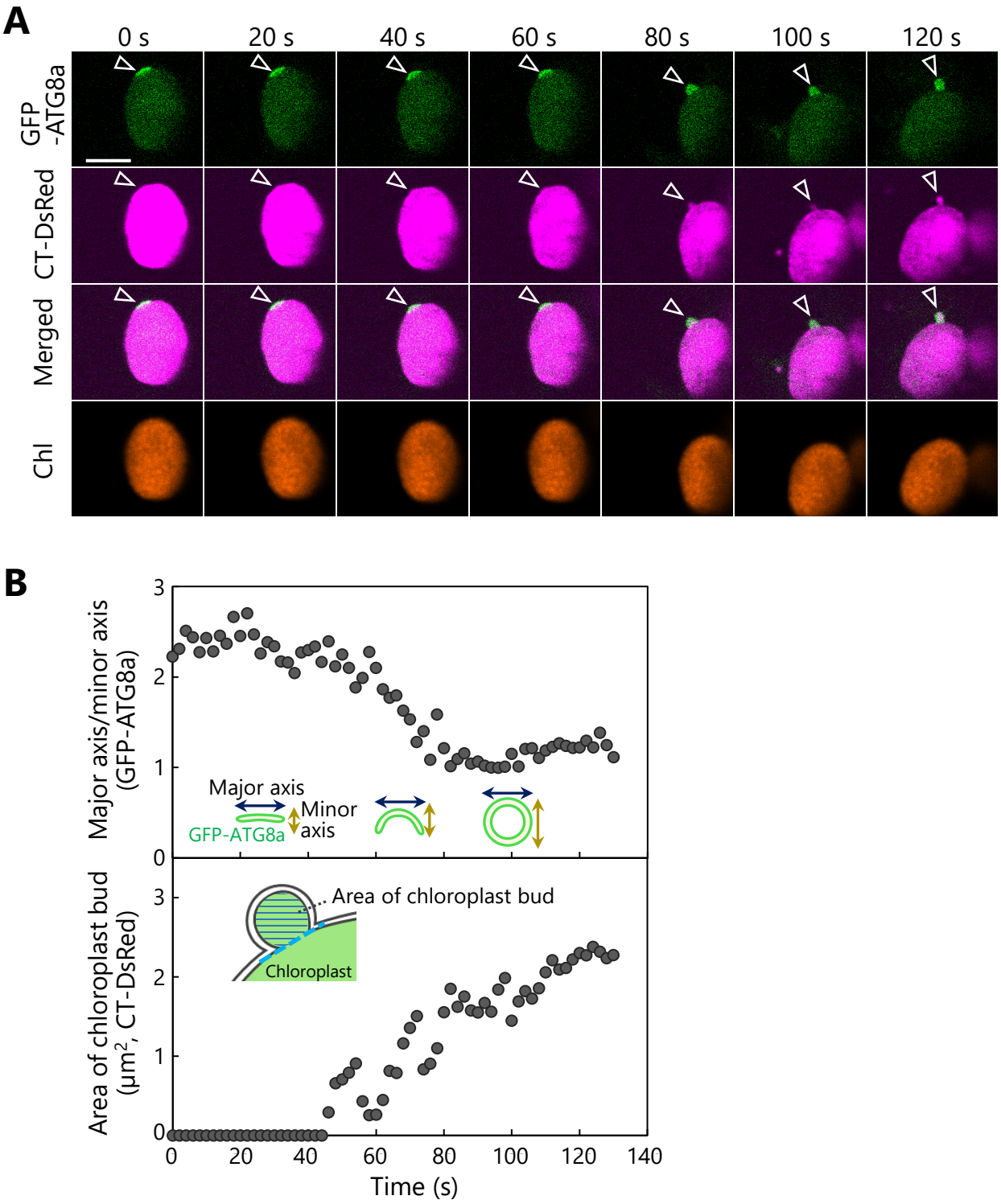

Figure 6–figure supplement 1. Another observation of the budding of the isolation membrane–associated site in a chloroplast.
A leaf accumulating the chloroplast stroma marker CT-DsRed and the isolation membrane marker GFP-ATG8a was incubated in sugar-free solution in darkness for 6 h from dawn and then observed. A second rosette leaf from a 22-d-old plant was used. Arrowheads indicate the position of the chloroplast-associated isolation membrane. The images are still frames from Video 17. Time scales above the images indicate the elapsed time from the start of the video. Green, GFP-ATG8a; magenta, CT-DsRed. Scale bars, 5 μm. (B) Time-dependent changes in the ratio of the major axis to the minor axis in the GFP-ATG8a-labeled isolation membrane (top) or in the area of the chloroplast budding structure (bottom), as measured from the images in (A).

Figure 6-figure supplement 2

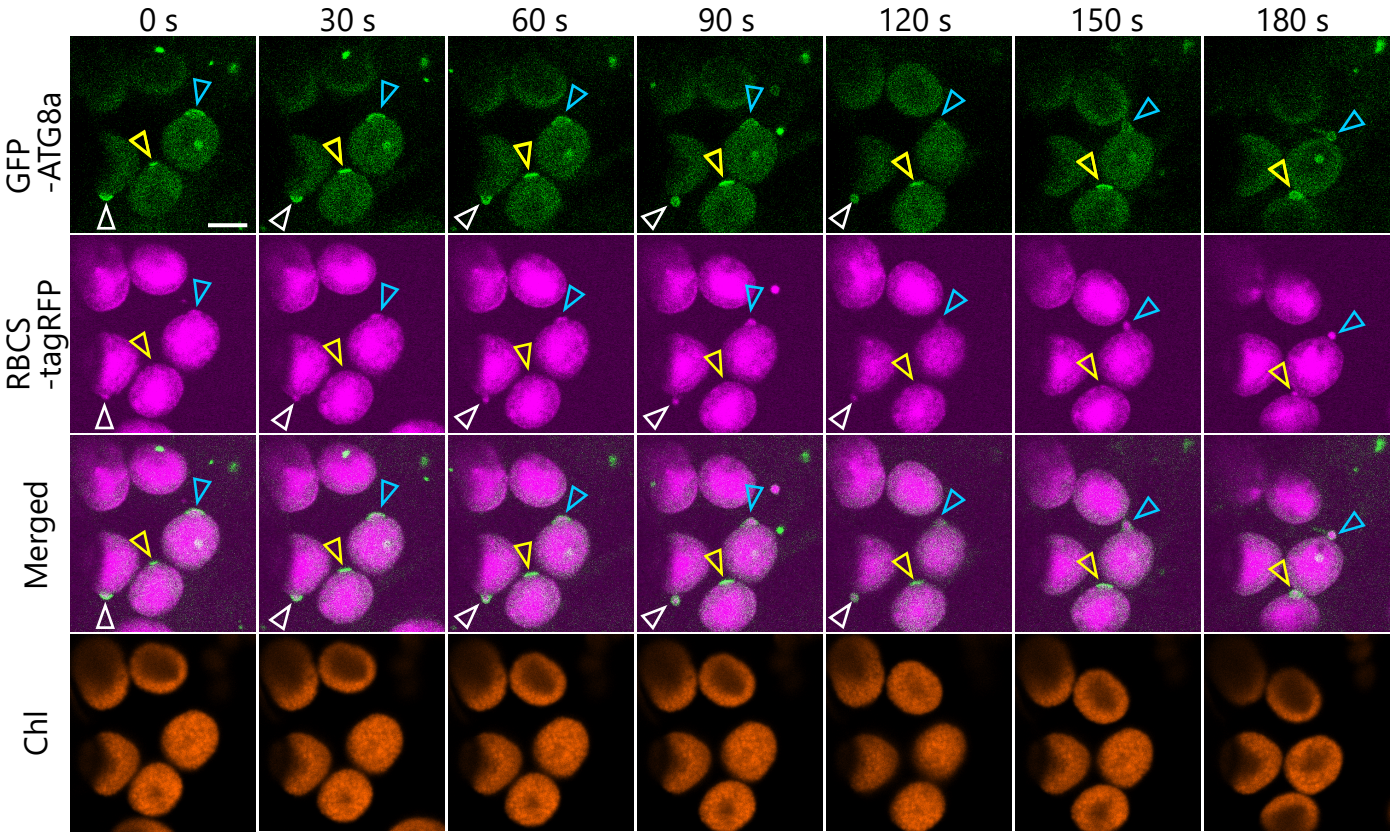

Figure 6–figure supplement 2. Chloroplast buds surrounded by the isolation membrane appear in multiple chloroplasts.
A leaf accumulating the chloroplast stroma marker RBCS-tagRFP and the isolation membrane marker GFP-ATG8a was incubated in sugar-free solution in darkness for 5 h from dawn and then observed. A second rosette leaf from a 21-d-old plant was used. White, yellow, and blue arrowheads indicate the isolation membrane–associated site in different chloroplasts, respectively. The images are still frames from Video 18. Time scales above the images indicate the elapsed time from the start of the video. Green, GFP-ATG8a; magenta, RBCS-tagRFP; orange, chlorophyll (Chl) fluorescence. Scale bars, 5 μm.

Figure 6-figure supplement 3

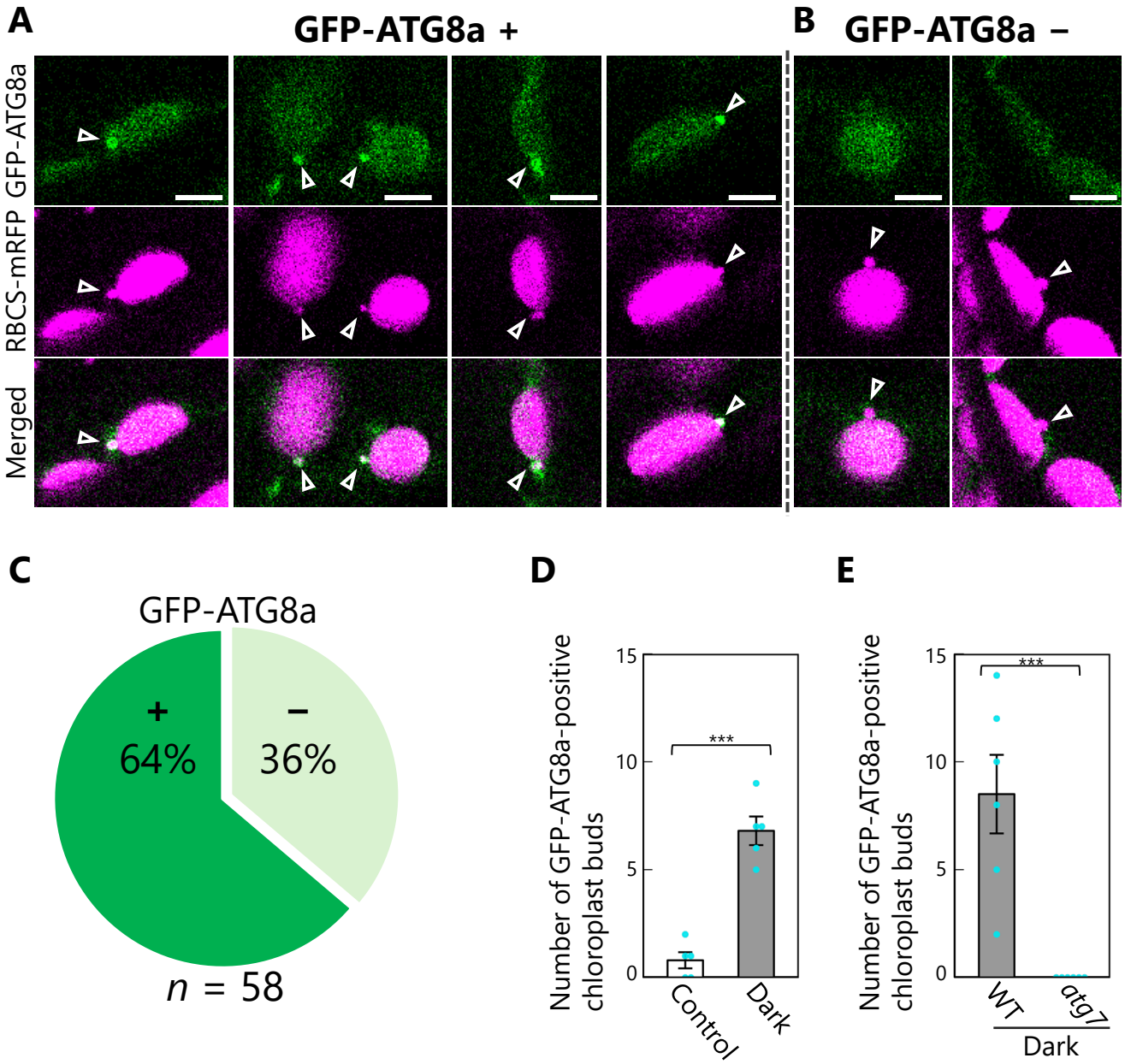

Figure 6–figure supplement 3. Proportion of chloroplast buds engulfed by GFP-ATG8a-labeled isolation membranes.
Leaves accumulating the chloroplast stroma marker RBCS-mRFP and the isolation membrane marker GFP-ATG8a were incubated in sugar-free solution in the dark for 5 to 9 h from dawn, and chloroplast budding structures were observed. Second rosette leaves from 22- to 23-d-old plants were used. (A and B) Four representative images of chloroplasts buds that are surrounded by GFP-ATG8a signals (A) or two representative images of chloroplast buds that are not labeled by GFP-ATG8a signals (B) are shown. Arrowheads indicate chloroplast budding structures. Green, GFP-ATG8a; magenta, RBCS-mRFP. Scale bars, 5 µm. (C) The proportions of chloroplast buds that are labeled by GFP-ATG8a signals (+) or not (–) were calculated from observations of 58 chloroplast buds from 8 individual plants. (D) The number of GFP-ATG8a-positive chloroplast buds, as shown in (A), were counted in the fixed regions from leaves incubated in the dark for 5 to 9 h from dawn (Dark) or from untreated leaves of plants grown under normal conditions (Control). Five individual plants were observed. (E) Leaves from wild-type (WT) or *atg7* plants accumulating RBCS-mRFP and GFP-ATG8a were incubated in the dark for 5 to 9 h from dawn, and the number of GFP-ATG8a-positive chloroplast buds was counted. Six individual plants were observed. Values are means ± SE (n = 5–6). Asterisks denote significant differences based on t-test (***, $P < 0.001$). Dots represent individual data points in each graph.

Figure 6-figure supplement 4

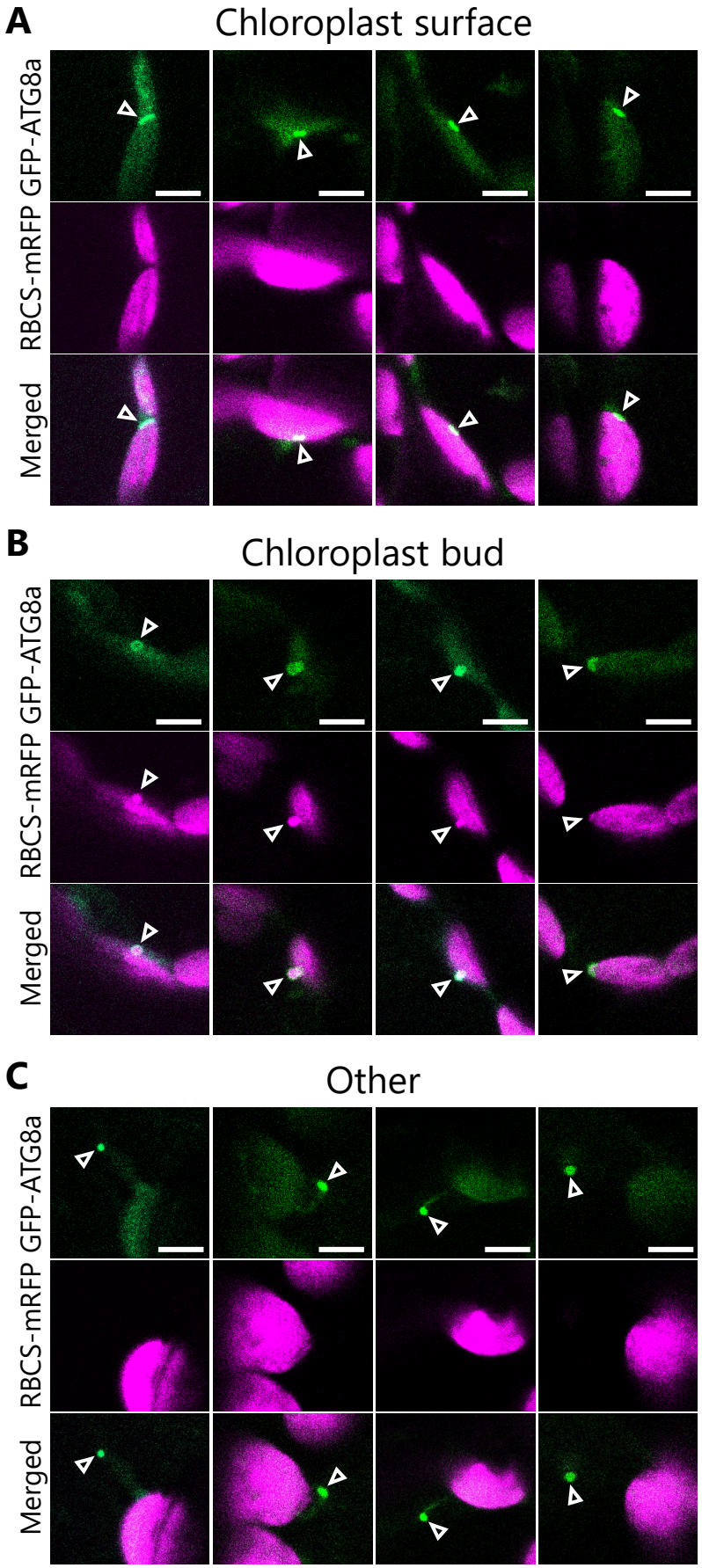

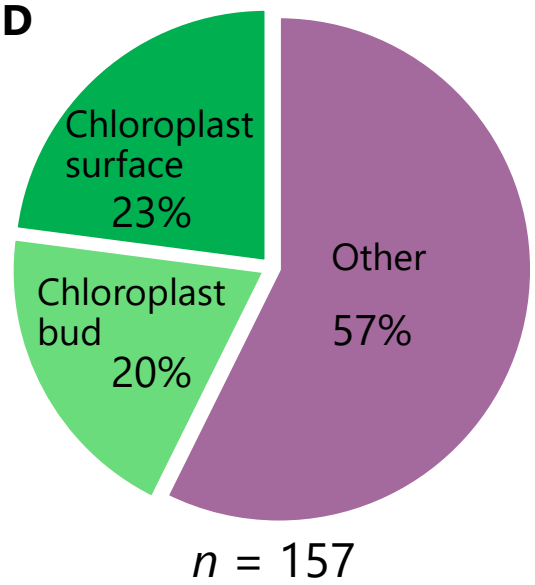

Figure 6–figure supplement 4. Proportion of GFP-ATG8a-labeled structures that are associated with chloroplasts. Leaves accumulating the chloroplast stroma marker RBCS-mRFP and the isolation membrane marker GFP-ATG8a were incubated in sugar-free solution in the dark for 5 to 9 h from dawn, and GFP-ATG8a-labeled structures in mesophyll cells were observed. Second rosette leaves from 22-d-old plants were used. (A to C) GFP-ATG8a-positive structures were classified into three types: flattened structures associated with the chloroplast surface (A), spherical or curved structures associated with chloroplast budding structures (B), and other structures (C). Four representative images of each type are shown. Green, GFP-ATG8a; magenta, RBCS-mRFP. Scale bars, 5 µm. (D) The proportions of the three types of GFP-ATG8a-labeled structures were calculated from observations of 157 GFP-ATG8a-labeled structures from 13 individual plants.

302 **SA influences stromule formation in autophagy-deficient mutants**

303 Our initial hypothesis was that stromules are related to RCBs: Stromule-rich cells appeared
304 because of impaired RCB production in *atg* mutants. However, our imaging assays above
305 revealed that RCBs emerge from mesophyll chloroplasts in the absence of prior formation of
306 stromules or protrusions (Figure 6), pointing to the existence of another factor responsible for
307 the elevated stromule formation seen in *atg* mutant leaves. A previous study reported the
308 hyperaccumulation of SA in senescing Arabidopsis *atg* mutants (Yoshimoto et al., 2009). Since
309 SA signaling stimulates immune responses, including stromule formation (Caplan et al., 2015),
310 we speculated that SA might contribute to stromule formation in autophagy-deficient mutants.
311 To investigate this possibility, we generated transgenic plants in the *atg5* mutant background
312 accumulating stromal GFP (CT-GFP) and a construct carrying NahG, encoding a bacterial SA
313 hydroxylase that catabolizes SA (Delaney, 1994; Yoshimoto et al., 2009). In these plant lines,
314 we evaluated the frequency of chloroplasts forming stromules, which are thin, tubular structures
315 of chloroplast stroma less than 1 μm in diameter (Hanson and Sattarzadeh, 2011; Brunkard et al.,
316 2015). We examined chloroplasts in guard cells, as this cell type actively forms many more
317 stromules than the mature chloroplasts of mesophyll cells (Ishida and Yoshimoto, 2008).
318 Chloroplasts in the guard cells of the *atg5* mutant formed more stromules than WT and NahG-
319 expressing plants (Figure 7A and 7B). The introduction of the NahG construct into the *atg5*
320 mutant background (*atg5* NahG) largely abolished stromule formation (Figure 7A and 7B). To
321 further explore the role of SA in stromule formation, we generated double mutants of
322 *SALICYLIC ACID INDUCTION DEFICIENT 2* (*SID2*), encoding the SA biosynthetic enzyme
323 ISOCHORISMATE SYNTHASE 1, and *ATG5* or *ATG7* (*sid2 atg5* and *sid2 atg7*). The *sid2*
324 mutation also resulted in fewer stromules in the double mutant relative to the respective *atg5*
325 and *atg7* single mutants in guard cells (Figure 7C and 7D).

326 We next observed stromule formation in mesophyll chloroplasts accumulating CT-GFP
327 or RBCS-mRFP and found that many chloroplasts formed stromules in senescent leaves of 36-
328 d-old *atg5* and *atg7* plants (Figure 7E and 7F, Figure 7–figure supplement 1). In cells from the
329 third rosette leaves of 36-d-old plants accumulating CT-GFP, we observed stromules in 22.5%
330 or 15.3% of chloroplasts from the *atg5* or *atg7* single mutants, respectively; however, the
331 introduction of the *sid2* mutation in *sid2 atg5* and *sid2 atg7* led to fewer stromules (9.8% or
332 2.5% in *sid2 atg5* or *sid2 atg7*, respectively; Figure 7E and 7F). In the leaves of 20-d-old plants,
333 we did not detect stromules in any genotype (Figure 7–figure supplement 2). These results
334 support the notion that SA accumulation due to autophagy deficiency activates stromule
335 formation during leaf senescence.

336 The frequency of stromules was higher in the *sid2 atg5* and *sid2 atg7* double mutants
337 than in WT plants and the *sid2* single mutant (Figure 7). We measured the content of hydrogen
338 peroxide (H_2O_2) in all plants, since reactive oxygen species also trigger stromule formation
339 (Caplan et al., 2015). In 36-d-old plants, *atg5* or *atg7* leaves contained 2.7 or 2.8 times more
340 H_2O_2 than WT leaves (Figure 7G). Notably, the presence of the *sid2* mutation in the *sid2 atg5*
341 and *sid2 atg7* double mutants did not alleviate H_2O_2 accumulation (Figure 7G). Such ROS
342 accumulation may thus be one factor responsible for the greater number of stromules in *sid2*
343 *atg5* and *sid2 atg7* compared with WT and *sid2* plants. Moreover, NahG expression did not
344 counteract the increase in H_2O_2 level caused by the *atg5* mutation (Figure 7–figure supplement
345 3). ROS accumulation in *atg* leaves may not depend on stimulation of SA signaling. These
346 results are consistent with the results of histochemical ROS staining of Arabidopsis leaves in a
347 previous study (Yoshimoto et al., 2009).

348

349 **DRP5b is not required for autophagy of chloroplast fragments**

350 Simultaneous progression of autophagosome formation and organelle segmentation has been
351 previously observed during mitophagy in mammals and budding yeast (Yamashita et al., 2016;
352 Fukuda et al., 2023). This autophagy-related mitochondrial division does not require the

Fig. 7

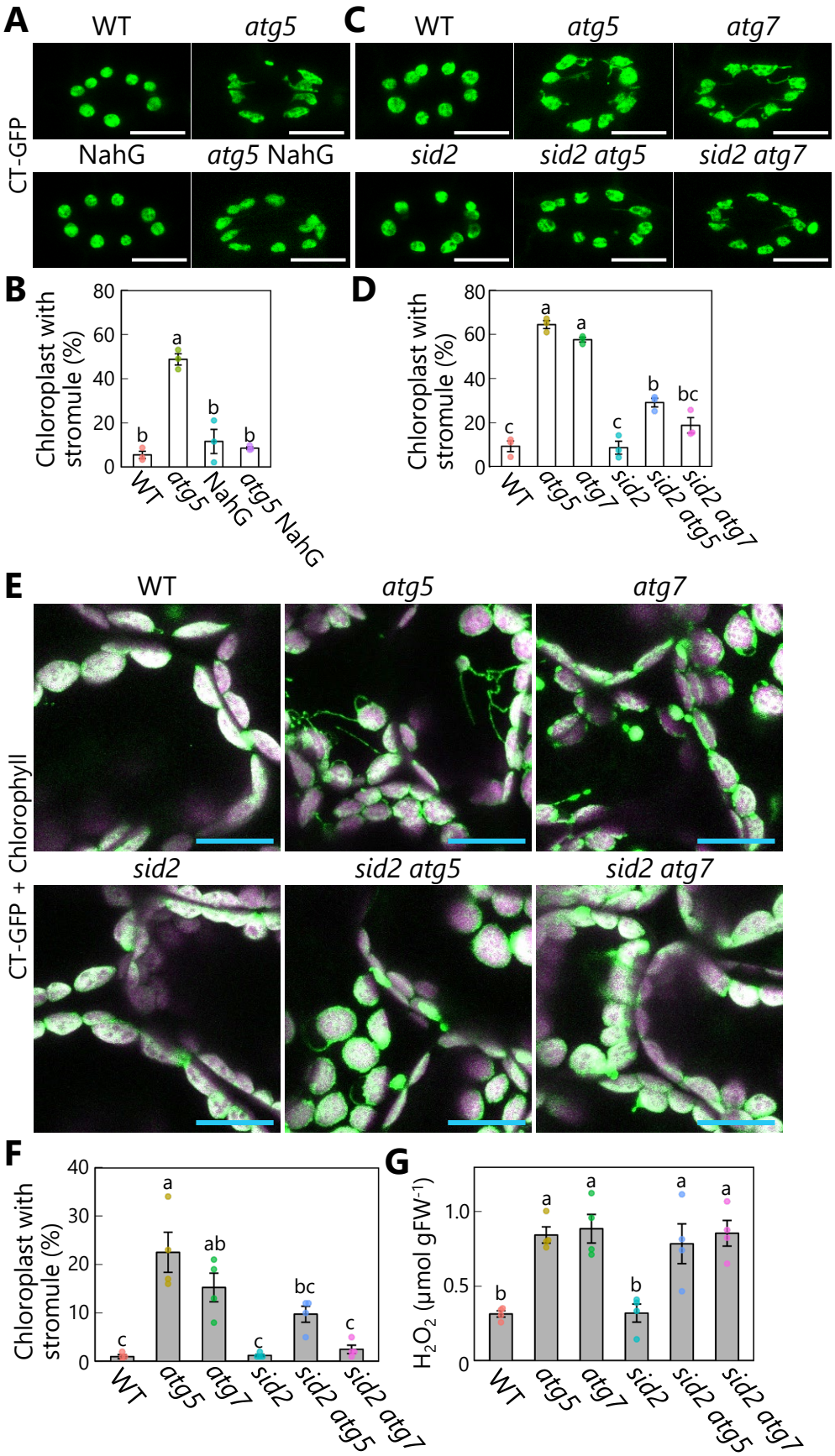

Figure 7. Diminished salicylic acid signal suppresses stromule formation in autophagy-deficient mutants.
(A) Orthogonal projections produced from *z*-stack images (10 μm in depth) of guard cells from wild-type (WT), *atg5*, NahG, and *atg5* NahG leaves accumulating chloroplast stroma–targeted GFP (CT-GFP). Second rosette leaves from 13-d-old plants were used. Scale bars, 10 μm. (B) Percentage of chloroplasts forming stromules in 10 stomata, from the observations described in (A). (C) Orthogonal projections produced from *z*-stack images (10 μm in depth) of guard cells from WT, *atg5*, *atg7*, *sid2*, *sid2 atg5*, and *sid2 atg7* leaves accumulating CT-GFP. Scale bars, 10 μm. (D) Percentage of chloroplasts forming stromules in 10 stomata, from the observations described in (C). (E) Orthogonal projections produced from *z*-stack images (15 μm in depth) of mesophyll cells from WT, *atg5*, *atg7*, *sid2*, *sid2 atg5*, and *sid2 atg7* leaves accumulating CT-GFP. Third rosette leaves from 36-d-old plants were observed. Green, CT-GFP; magenta, chlorophyll fluorescence. Only the merged channels are shown. Scale bars, 20 μm. (F) Percentage of chloroplasts forming stromules out of 50 chloroplasts in mesophyll cells, from the observations described in (E). (G) Hydrogen peroxide (H_2O_2) content in third rosette leaves from 36-d-old WT, *atg5*, *atg7*, *sid2*, *sid2 atg5*, and *sid2 atg7* plants. Different lowercase letters denote significant differences based on Tukey's test ($P < 0.05$). Values are means ± SE ($n = 3$ in B and D or 4 in F and G). Dots represent individual data points in each graph.

Figure 7-figure supplement 1

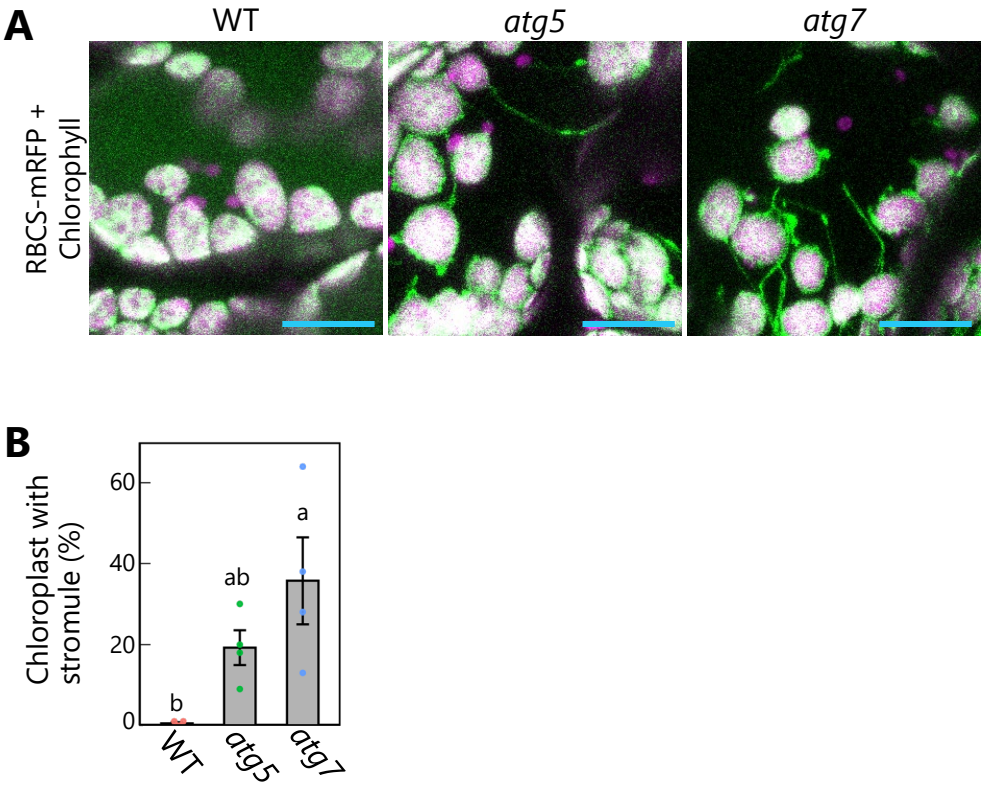

Figure 7–figure supplement 1. Autophagy deficiency activates stromule formation from mesophyll chloroplasts accumulating RBCS-mRFP in senescing leaves.

(A) Orthogonal projections produced from *z*-stack images (15 µm in depth) of mesophyll cells from leaves of WT, *atg5*, and *atg7* plants accumulating RBCS-mRFP. Third rosette leaves from 36-d-old plants were observed. Green, RBCS-mRFP; magenta, chlorophyll fluorescence. Only the merged channels are shown. Spherical bodies only exhibiting chlorophyll signal represent a portion of chloroplasts in pavement cells. Scale bars, 20 µm. (B) Percentage of chloroplasts forming stromules out of 50 chloroplasts in mesophyll cells, from the observations described in (A). Different lowercase letters denote significant differences based on Tukey's test ($P < 0.05$). Values are means ± SE ($n = 4$). Dots represent individual data points in the graph.

Figure 7-figure supplement 2

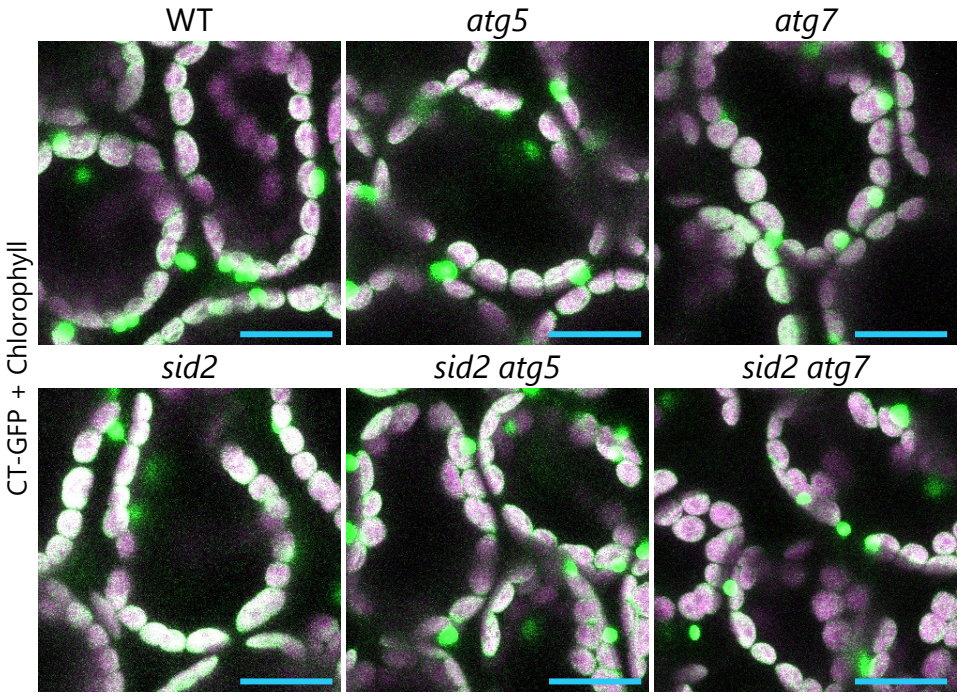

Figure 7–figure supplement 2. Autophagy deficiency does not activate stromule formation from mesophyll chloroplasts in young leaves.
Orthogonal projections produced from *z*-stack images (15 µm in depth) of mesophyll cells from WT, *atg5*, *atg7*, *sid2*, *sid2 atg5*, and *sid2 atg7* leaves accumulating CT-GFP. Third rosette leaves from 20-d-old plants were observed. Green, CT-GFP; magenta, chlorophyll fluorescence. Only the merged channels are shown. Scale bars, 20 µm.

Figure 7-figure supplement 3

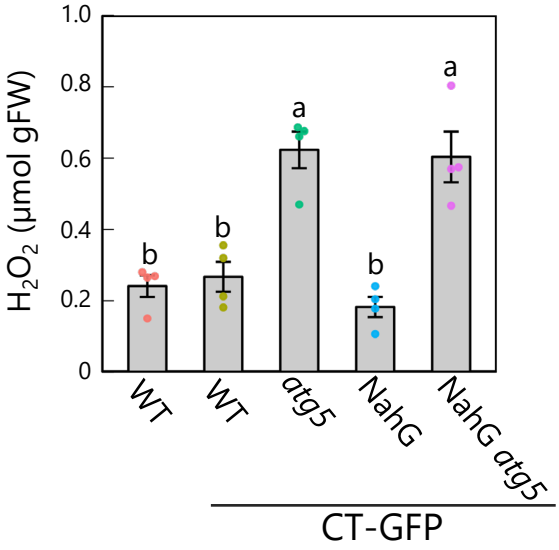

Figure 7–figure supplement 3. NahG expression does not counteract the increase in hydrogen peroxide content produced by the *atg5* mutation.

Hydrogen peroxide (H_2O_2) contents in third rosette leaves from 36-d-old plants. WT plants without any transgenic construct and CT-GFP-expressing plants in the WT, *atg5*, NahG, and *atg5* NahG backgrounds were used. Different lowercase letters denote significant differences based on Tukey's test ($P < 0.05$). Values are means ± SE ($n = 4$). Dots represent individual data points.

353 mammalian Drp1- or yeast Dnm1-dependent division machinery, respectively. Here, we
354 examined whether the DRP5B-mediated chloroplast division participates in chloroplast
355 autophagy and RCB production.
356 To this end, we generated *drp5b* mutant lines accumulating the stromal marker RBCS-
357 mRFP or stromal GFP (CT-GFP). Although the mature leaves of *drp5b* had larger chloroplasts
358 than WT leaves, reflective of the impaired chloroplast division during cell expansion typical of
359 this mutant, many RCBs accumulated when the leaves were incubated in darkness in the
360 presence of concA (Figure 8A and 8B, Figure 8–figure supplement 1). We detected no RCB in
361 the leaves of the *drp5b atg5* double mutant (Figure 8–figure supplement 1). These results
362 indicate that RCB-mediated chloroplast autophagy is active in the *drp5b* mutant. To obtain an
363 independent confirmation of this result, we performed an immunoblot assay of autophagy flux,
364 based on the detection of free mRFP derived from the vacuolar cleavage of RBCS-mRFP (Ono
365 et al., 2013). When we incubated the leaves of plants accumulating RBCS-mRFP in darkness
366 without concA, free mRFP levels increased in leaves of WT but not *atg5* or *atg7* plants (Figure
367 8C and 8D), indicating the occurrence of autophagy-dependent degradation of stromal proteins
368 in response to sugar starvation in WT plants. The accumulation of free mRFP in the *drp5b*
369 mutant was at least as high as that seen in WT plants (Figure 8C). The ratio of free mRFP to
370 RBCS-mRFP increased in WT and *drp5b* plants after dark treatment (6.1 or 4.1 times higher
371 compared with control conditions in WT plants or *drp5b*, respectively), consistent with
372 autophagy-mediated degradation of chloroplast fragments (Figure 8D). Confocal microscopy
373 observations of mesophyll cells also showed the spread of mRFP signal in the vacuolar lumen in
374 dark-treated leaves of WT and *drp5b* plants (Figure 8–figure supplement 2). These results
375 indicate that the autophagic degradation of chloroplast stroma is active in both genotypes. The
376 accumulation of free mRFP was 3.2 times higher in untreated leaves of *drp5b* compared with
377 untreated WT leaves (Figure 8D); therefore, the activity of chloroplast autophagy might be
378 constitutively higher in leaves of *drp5b* than in those of WT plants.
379 We observed the budding off of chloroplast fragments in leaves of the *drp5b* mutant.
380 We incubated a leaf from the *drp5b* mutant accumulating RBCS-mRFP in darkness, which
381 allowed us to observe the formation of a chloroplast bud and its release (Figure 9A, arrowheads;
382 Video 19). In a leaf of the *drp5b* mutant accumulating RBCS-mRFP and GFP-ATG8a, we
383 detected the vesiculation of a chloroplast fragment starting at the site to which the isolation
384 membranes, labeled by GFP-ATG8a, were tightly associated (Figure 9B). The isolation
385 membranes were anchored at two sites of a large chloroplast in a leaf of the *drp5b* mutant
386 (Figure 9B, white and blue arrowheads); the chloroplast gradually protruded before releasing
387 RCBs surrounded by autophagosomes (Figure 9B, Video 20). We conclude that DRP5B is
388 dispensable for the autophagy-related division of chloroplast fragments.

389 ## Discussion

390

391 ### Chloroplast division machinery functioning in piecemeal-type chloroplast autophagy

392 We previously demonstrated that chloroplast components in mesophyll cells are transported to
393 the vacuole as a type of autophagic cargo termed RCBs to facilitate amino acid recycling (Ishida
394 et al., 2008; Hirota et al., 2018). However, how a portion of chloroplasts is mobilized into the
395 vacuolar lumen remained uncertain. In this study, high-resolution time-lapse imaging techniques
396 allowed us to visualize the trafficking progression of chloroplast fragments from their parental
397 chloroplasts to the vacuolar lumen. Importantly, we established that the development of the
398 chloroplast-associated isolation membrane and the division of the chloroplast fragment occur
399 simultaneously. This autophagy-related chloroplast division does not rely on DRP5B-mediated
400 chloroplast division. Likewise, the formation of chloroplast buds is unlikely to be linked to the
401 formation of stromules. Therefore, an unknown division machinery may be required for the
402 autophagy-related division of chloroplast fragments. A similar organelle division mechanism
403 takes place during mitophagy in mammals and budding yeast. The site of a mitochondrion that

Fig. 8

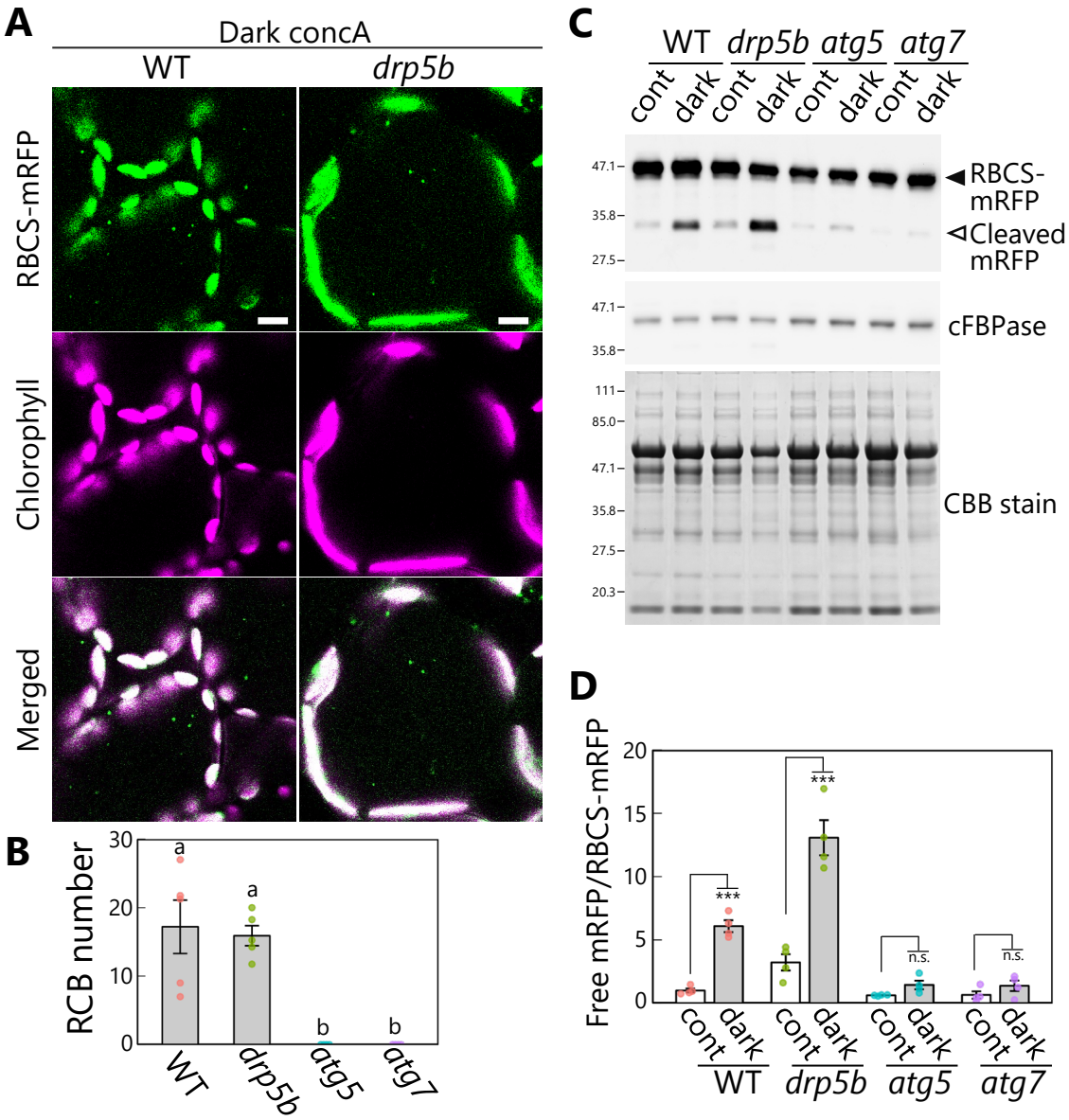

Figure 8. DRP5b is dispensable for chloroplast autophagy in sugar-starved leaves.
(A) Confocal images of mesophyll cells from wild-type (WT) and *drp5b* leaves accumulating the stroma marker RBCS-mRFP. Second rosette leaves from 21-d-old plants were incubated in sugar-free solution containing 1 µM concanamycin A (concA) in darkness for 1 d. Green, RBCS-mRFP; magenta, chlorophyll fluorescence. Scale bars, 10 µm. (B) Number of accumulated RCBs in WT, *drp5b*, *atg5*, and *atg7* leaves, counted from the observations of leaves incubated in the dark with concA described in (A). Different lowercase letters denote significant differences based on Tukey's test ($P < 0.05$). Values are means ± SE ($n = 4$–5). (C) Biochemical detection of autophagy flux for chloroplast stroma based on a free RFP assay. RFP and cFBPase (loading control) were detected by immunoblotting of soluble protein extracts from leaves of WT, *drp5b*, *atg5*, and *atg7* plants accumulating RBCS-mRFP. Protein extracts from either untreated control leaves (cont) or leaves after 2 d of incubation in darkness (dark) were used. Total protein was detected by Coomassie Brilliant Blue (CBB) staining as a loading control. The filled arrowhead indicates RBCS-mRFP fusion, and the open arrowhead indicates free mRFP derived from the cleavage of RBCS-mRFP. (D) Quantification of the free mRFP/RBCS-mRFP ratio shown relative to that of untreated WT plants, which was set to 1. Asterisks denote significant differences based on *t*-test (***, $P < 0.001$; n.s., not significant). Values are means ± SE ($n = 4$). Dots represent individual data points in each graph.

Figure 8–figure supplement 1

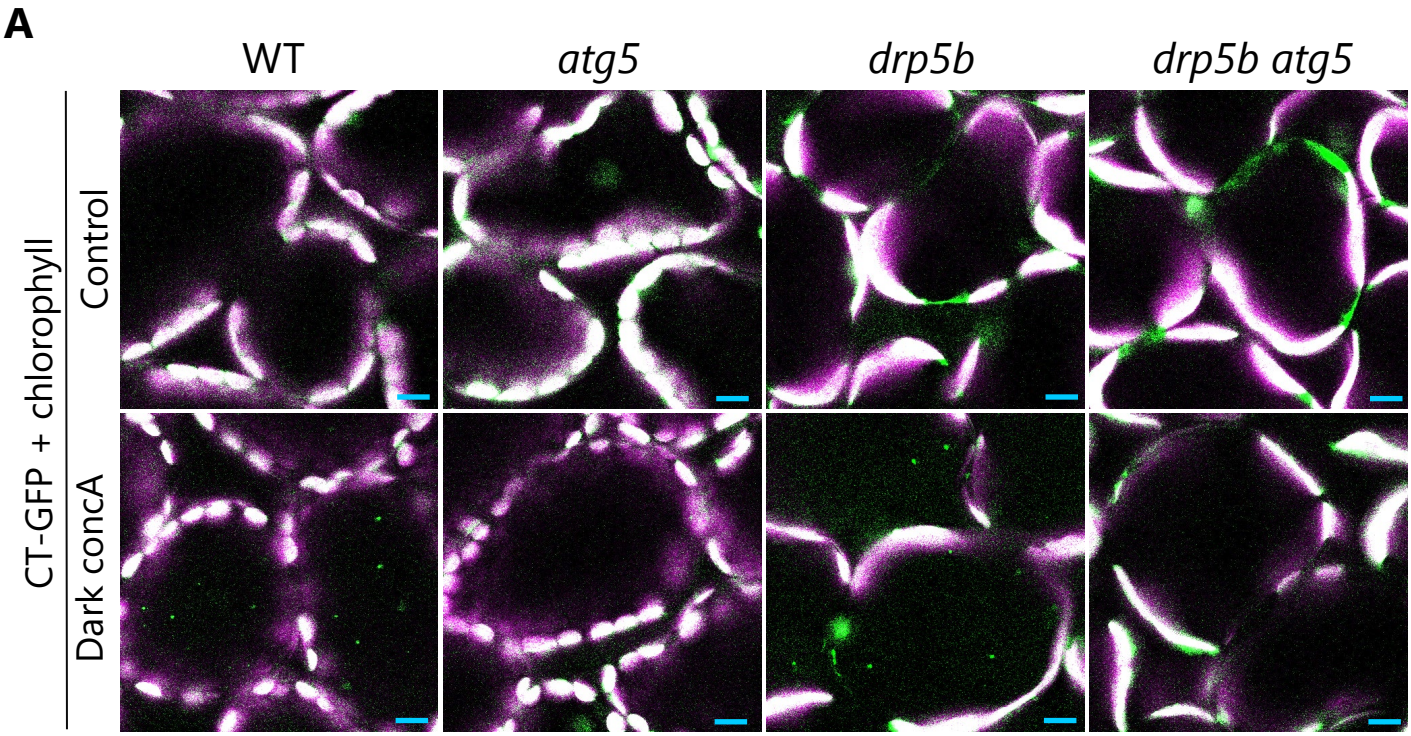

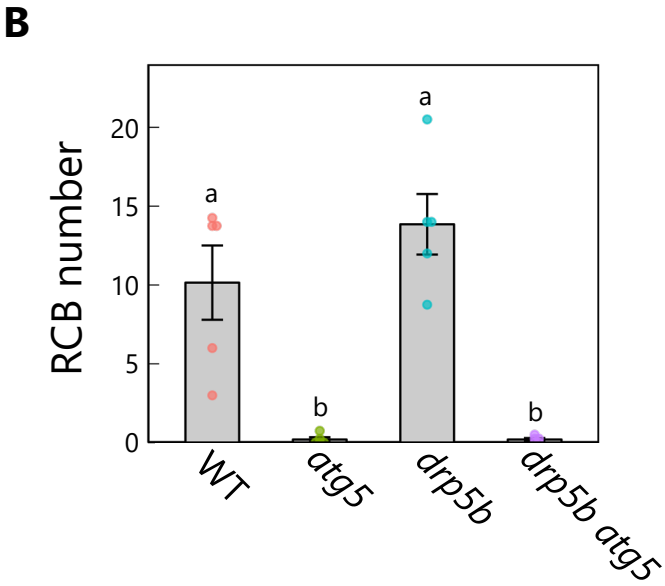

Figure 8–figure supplement 1. Production of Rubisco-containing bodies in *drp5b* mutants is ATG5 dependent.
(A) Confocal images of mesophyll cells from wild-type (WT), *atg5*, *drp5b*, and *drp5b atg5* leaves accumulating the stroma marker CT-GFP. Second rosette leaves from 21-d-old plants were incubated in sugar-free solution containing 1 µM concanamycin A (concA) in darkness for 1 d. Second rosette leaves from untreated plants were used as control. Green, CT-GFP; magenta, chlorophyll fluorescence. Only the merged channels are shown. Small puncta containing CT-GFP without chlorophyll signal appear as green and are RCBs in the vacuole. Scale bars, 10 µm. (B) Number of accumulated RCBs, counted from the observations of leaves incubated in the dark with concA described in (A). Different lowercase letters denote significant differences based on Tukey's test ($P < 0.05$). Values are means ± SE ($n = 5$). Dots represent individual data points.

Figure 8–figure supplement 2

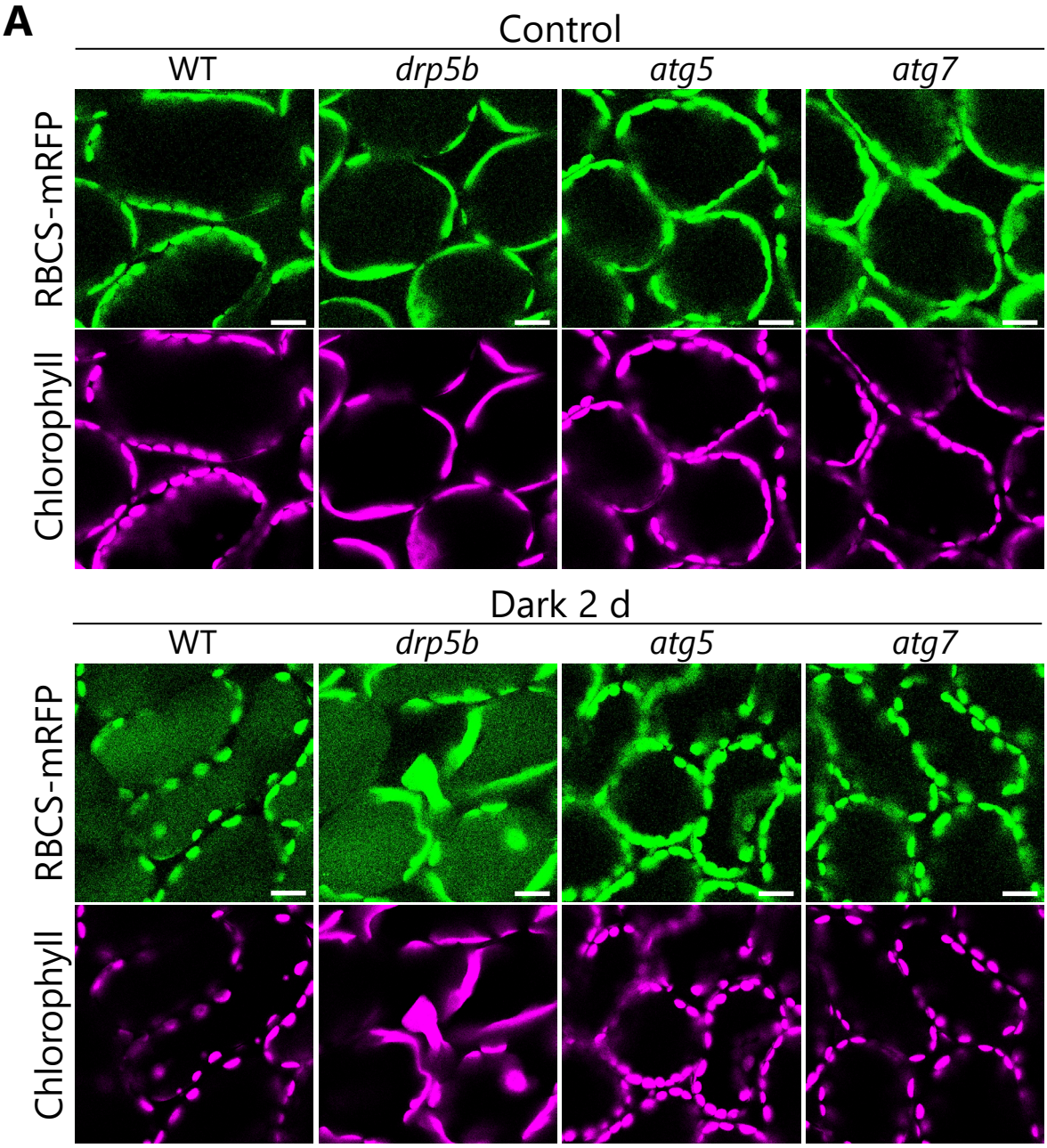

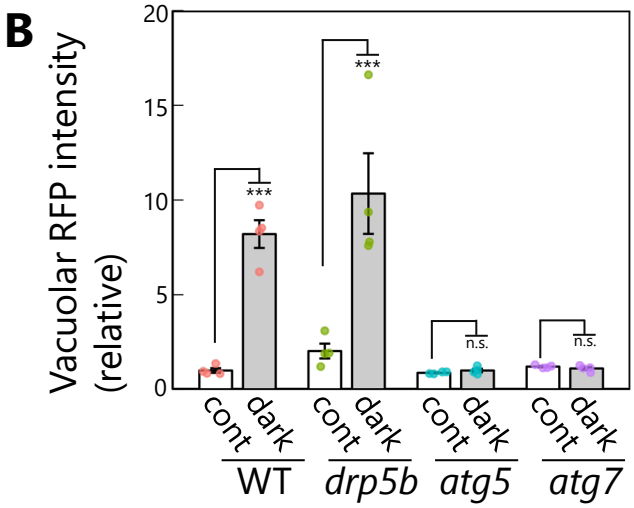

Figure 8–figure supplement 2. Vacuolar accumulation of stromal marker proteins in sugar-starved leaves.
(A) Confocal images of mesophyll cells from wild-type (WT), *drp5b*, *atg5*, and *atg7* leaves accumulating the stroma marker RBCS-mRFP. Second rosette leaves from 21-d-old plants were incubated in sugar-free solution in darkness for 2 d. Second rosette leaves from untreated plants are shown as control. Green, RBCS-mRFP; magenta, chlorophyll fluorescence. Scale bars, 20 µm. (B) RFP intensity in the vacuolar lumen, as measured from the observations described in (A) and shown relative to that of untreated WT plants, which was set to 1. Asterisks denote significant differences based on *t*-test (***, $P < 0.001$; n.s., not significant). Values are means ± SE ($n = 4$). Dots represent individual data points.

Fig. 9

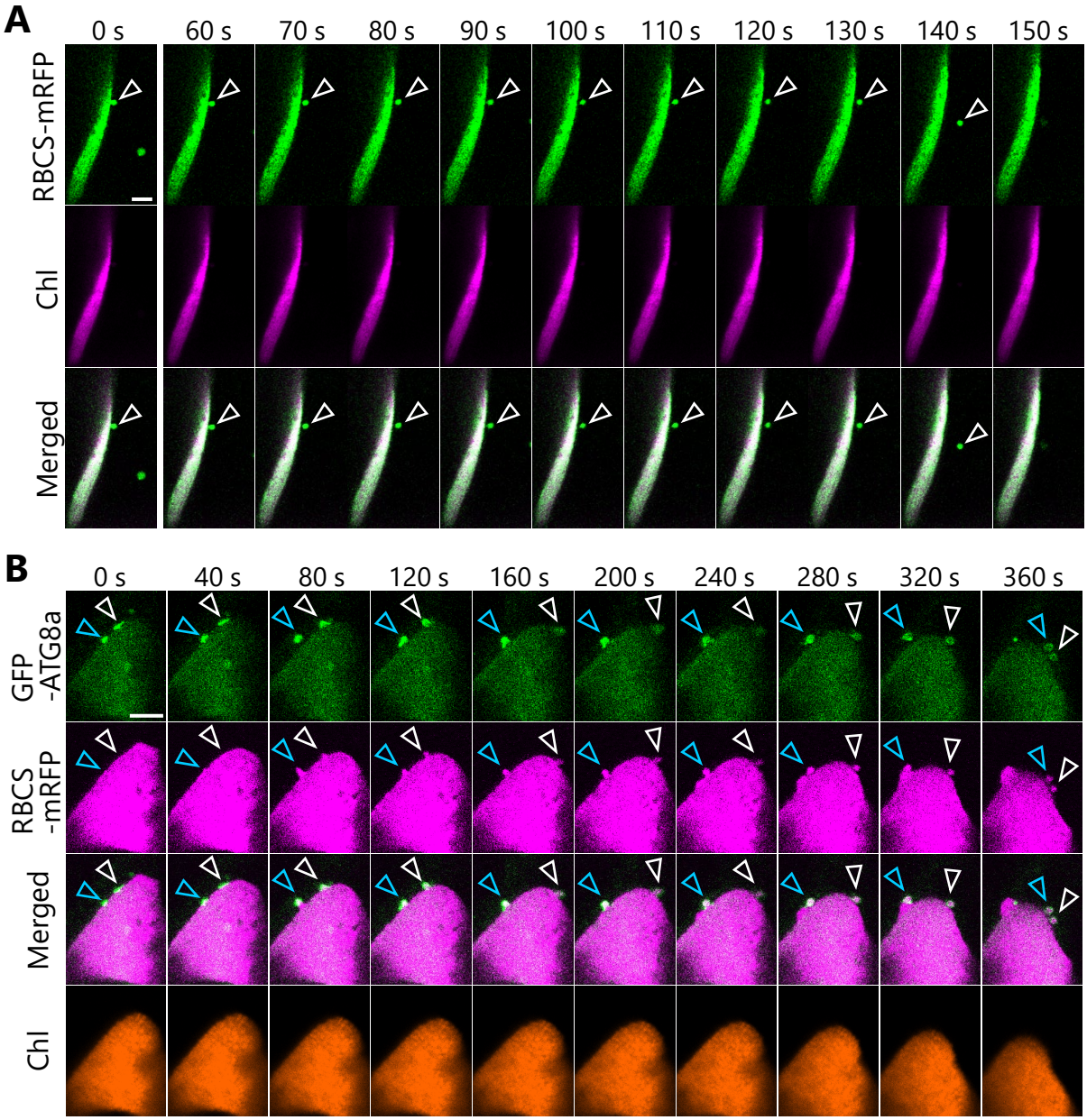

Figure 9. Formation and segmentation of chloroplast buds in leaves of the *drp5b* mutant.
(A) A leaf from the *drp5b* mutant accumulating the stroma marker RBCS-mRFP was incubated in sugar-free solution in darkness for 5 h from dawn and then observed. Arrowheads indicate a chloroplast bud. Green, RBCS-mRFP; magenta, chlorophyll fluorescence (Chl). (B) A leaf from the *drp5b* mutant accumulating the stroma marker RBCS-mRFP and the isolation membrane marker GFP-ATG8a were incubated in sugar-free solution in darkness for 6 h from dawn and then observed. Second rosette leaves from 21- to 22-d-old plants were used. Arrowheads indicate the position of the chloroplast-associated isolation membrane. White and blue arrowheads indicate different isolation membrane–associated sites in a chloroplast. Images in (A) and (B) are still frames from Videos 19 and 20, respectively. Time scales above the images indicate the elapsed time from the start of the respective videos. Green, GFP-ATG8a; magenta, RBCS-mRFP; orange, chlorophyll (Chl) fluorescence. Scale bars, 5 µm.

is associated with the isolation membrane protrudes and divides as the isolation membrane develops and becomes an enclosed autophagosome (Yamashita et al., 2016). This type of mitochondrial division is independent of Drp1 and Dnm1. In yeast, the mitochondrial intermembrane-space protein mitofissin/Atg44 divides the mitochondrial fragment in coordination with autophagosome maturation (Fukuda et al., 2023). A functionally equivalent protein has not been identified in mammals.

Numerous studies have explored the molecular mechanisms of chloroplast division during the development of juvenile leaves (Chen et al., 2018). For instance, in Arabidopsis plants, ARC6 and PARALOG OF ARC6 (PARC6) mediate the tethering of the FTSZ ring on the chloroplast inner envelope (Vitha et al., 2003). PLASTID DIVISION 1 (PDV1) and PDV2 recruit DRP5B to the division site on the chloroplast outer envelope (Miyagishima et al., 2006). The ARC6–PDV2 and PARC6–PDV1 complexes may control the coordination of the stromal FTSZ ring and the cytosolic DRP5B ring (Wang et al., 2017; Chen et al., 2018). Therefore, the controlled division of plastids requires the cooperation of multiple protein complexes across the inner and outer envelopes. Nevertheless, whether chloroplasts divide during their piecemeal degradation has not been evaluated. It seems likely that autophagy-related division of chloroplast fragments needs to be carefully regulated, as the size of the segment has to fit into the autophagosome. Since the volume occupied by chloroplasts per cell is tightly regulated during cell expansion (Pyke and Leech, 1994), the decline of chloroplast volume during starvation or senescence might also be highly controlled. Further studies are needed to elucidate the molecular machinery underlying the autophagy-related division of chloroplast fragments for degradation.

In our evaluation of chloroplast buds associated with GFP-ATG8a in excised leaves exposed to darkness (Figure 6–figure supplement 3), 36% of chloroplast budding structures were not labeled by GFP-ATG8a. Since endogenous ATG8 family members (ATG8a–8i) were functional, such structures might have formed due to the activities of non-labeled ATG8 proteins. Another possibility is that autophagy-independent chloroplast budding might occur. For example, stromule-related structures might form. CHLOROPLAST VESICULATION (CV)–containing vesicles are also observed as autophagy-independent puncta released from chloroplasts for degradation (Wang and Blumwald, 2014; Pan et al., 2023). However, biochemical assays for chloroplast autophagy flux suggested that ATG-dependent pathways were the main routes for the vacuolar degradation of stromal components during the darkness-induced sugar starvation treatment used in this study (Figure 8). Previous studies have revealed that CV plays a role in plant responses to abiotic stress, such as drought or salt stress (Wang and Blumwald, 2014; Pan et al., 2023). A recent study suggested that autophagy, but not CV-dependent pathways, is the main contributor to the adaptative response of metabolism to sugar starvation (Barros et al., 2023). Overall, these insights support the notion that, during the early phase of sugar starvation (such as 1 to 2 d of extended darkness), the autophagy-associated machinery is mainly responsible for chloroplast segmentation and degradation. It is unclear what type of process contributed to the decrease in chloroplast stroma volume in leaves of *atg7* plants exposed to dark treatment (Figure 1–figure supplement 2).

An assay of autophagic flux of RBCS-mRFP protein in leaves from *drp5b* mutants suggested the possibility that chloroplast autophagy activity is constitutively higher in leaves of *drp5b* than in WT plants (Figure 8). The impaired chloroplast division due to the *drp5b* mutation might affect photosynthesis-mediated energy production and reduce energy availability, thereby activating chloroplast autophagy without dark treatment. As described in the Introduction, entire organelle–type autophagy (chlorophagy) mediates the degradation of chloroplasts in their entirety. Mesophyll cells in leaves of *drp5b* mutants contain few chloroplasts (approximately 4 per cell), whereas those in WT leaves contain approximately 60 chloroplasts (Miyagishima et al., 2006). Since the volume in a cell occupied by chloroplasts is similar between genotypes, chloroplasts from *drp5b* are much larger than WT chloroplasts.

Chloroplasts that are too large might show inhibited chlorophagy, resulting in the alternative activation of piecemeal-type chloroplast autophagy. Analyzing how chloroplasts are degraded in mutants of chloroplast division ring components might provide insight into the interplay between entire organelle–type autophagy and piecemeal-type autophagy during chloroplast degradation.

Autophagy receptor and adapter proteins for the degradation of mature chloroplasts

Organelle-selective autophagy is typically controlled by receptor proteins that recognize the target organelles and act as a bridge between the organelles and isolation membrane–anchored ATG8 (Farre and Subramani, 2016). The observation of a chloroplast-associated isolation membrane (Figure 6) suggests that the receptors for chloroplast autophagy connect the isolation membrane to the chloroplast envelope. Such interaction might facilitate the localization of the isolation membrane on the region of subsequent chloroplast budding and its development along the chloroplast surface. In budding yeast, the accumulation of the mitophagy receptor Atg32 is required for the formation of the mitophagosome. Atg32 binds to the mitochondrial outer membrane and interacts with Atg8 and Atg11, the latter being a scaffold protein recruiting other ATG members, for autophagosome formation. In fission yeast (*Schizosaccharomyces pombe*), Atg43 located on the mitochondrion outer membrane binds to Atg8 to stabilize the autophagosomal membrane for mitophagosome formation during starvation (Fukuda et al., 2020). In mammalian mitophagy, five types of mitophagy receptors have been identified that bind to LC3 (light chain 3) or GABARAP proteins, the mammalian orthologs of ATG8 (Onishi et al., 2021). Whether similar receptors work for chloroplast autophagy in mature leaves has not been established. Atg39 is the receptor for nucleophagy in budding yeast (Mochida et al., 2015), during which the condensation of Atg39 enables the protrusion of the nuclear membrane to be sequestered by the autophagosome (Mochida et al., 2022). The accumulation of receptor proteins might contribute to chloroplast budding to form RCBs.

Another important regulator of the selective autophagy of organelles is the ubiquitination of the targets of this process. One well-characterized process is mammalian mitophagy regulated by PTEN-induced kinase 1 (PINK1) and Parkin (Ohnishi et al., 2021). PINK1 accumulates on the surfaces of damaged mitochondria, facilitating the ubiquitination of the mitochondria by the E3 ubiquitin ligase Parkin. Subsequently, autophagy adapter proteins connect the ubiquitin chain to LC3/GABARAP proteins for the selective elimination of the ubiquitinated mitochondria via autophagosomes (Lazarou et al., 2015). Five autophagy adaptor proteins have been identified in mammals: p62/Sequestosome-1 (SQSTM1), Next to BRCA1 gene 1 (NBR1), Tax1-binding protein 1 (TAX1BP1), nuclear dot protein52 (NDP52), and optineurin (OPTN). Among these, a plant ortholog of NBR1 has been identified (Svenning et al., 2011). A recent study found that Arabidopsis NBR1 accumulates on damaged chloroplasts to induce their removal in their entirety (Lee et al., 2023). NBR1 may participate in the recognition of damaged chloroplasts during the entire organelle–type degradation of chloroplasts by chlorophagy. Another study demonstrated that NBR1 regulates the selective degradation of the outer envelope–bound TOC protein complexes that control cytoplasm-to-plastid protein import (Wan et al., 2023). TOC proteins are ubiquitinated under stress conditions such as ultraviolet-B exposure or high temperature and are then degraded by autophagosomes through NBR1-mediated recognition. These findings suggest that NBR1 plays an important role in the degradation of damaged chloroplast proteins. Whether ubiquitination and NBR1 participate in the degradation of portions of chloroplasts via RCBs under sugar-starvation conditions has not been evaluated.

Roles of stromules

The molecular functions of stromules are not completely understood. We predicted a functional

link between stromules and RCBs such that stromule-associated structures are vesiculated and become RCBs for autophagic degradation. However, our imaging assays revealed that chloroplast stromule formation is not essential for RCB formation in mesophyll cells (Figure 6). The use of the *sid2* mutant and NahG transgenic lines indicated the close association between enhanced SA signaling and the elevated stromule formation observed in *atg* mutants (Figure 7). This finding is consistent with the suggested role of stromules in inducing programmed cell death as an SA-dependent immune response (Caplan et al., 2015). We attribute the enhanced stromule formation in *atg* mutant leaves to the higher SA and ROS levels, alone or in combination with the excess stromal fraction accumulating in these mutants due to impaired RCB formation.

In root cells, an association of the isolation membrane with stromules of non-green plastids was reported (Spitzer et al., 2015). Stromule formation is more common in the non-green plastids of tissues without photosynthetic activity than in the mature chloroplasts in leaf mesophyll cells (Ishida and Yoshimoto, 2008; Hanson and Sattarzadeh, 2008). Therefore, the interaction between stromules and the isolation membrane might be important for the efficient degradation of non-green plastids by autophagy. Our study focused on the degradation mechanism of mature chloroplasts in leaves, since mature chloroplasts are rich in nutrients and amino acids and their degradation is particularly important for plant nutrient recycling (Makino and Osmond, 1991). There might also be differences in the degradation mechanism of plastids among cell types.

Intracellular dynamics for the transport of RCBs

Soluble *N*-ethylmaleimide-sensitive factor attachment protein receptors (SNAREs) mediate versatile membrane fusion events (Ito and Uemura, 2022). Multiple SNARE proteins participate in the fusion of the lysosomal/vacuolar membrane to the autophagosomal membrane in mammals and budding yeast. A recent study reported the involvement of the Arabidopsis SNARE proteins, VESICLE-ASSOCIATED MEMBRANE PROTEIN 724 (VAMP724) and VAMP726, in autophagosome formation (He et al., 2022). In this study, we observed an interesting morphology of vacuolar membranes that incorporate RCBs into the vacuole (Figure 4). A similar phenomenon was previously observed during the transport of pexophagosomes (autophagosomes containing peroxisome components) in Arabidopsis leaves (Oikawa et al., 2022). Thus, the transient engulfment of an autophagosome by the vacuolar membrane might be a common phenomenon for vacuolar incorporation in leaf mesophyll cells. However, the underlying mechanisms are unknown. In mammals, two autophagosomal membrane–anchored SNAREs, Syntaxin 17 (Stx17) and Ykt6, independently contribute to autophagosome–lysosome fusion (Itakura et al., 2012; Matsui et al., 2018). Stx17 translocates to the closed autophagosome transiently, enabling its fusion with the lysosome (Tsuboyama et al., 2016). Such a translocation system might allow the recruitment of the vacuolar membrane for its fusion with the mature autophagosomes containing RCBs in plant cells.

Concluding remarks

The current study revealed how a type of piecemeal autophagy transports chloroplast stroma and envelope components into the vacuole for degradation in mature Arabidopsis leaves. The key event is the development of the isolation membrane along the chloroplast surface, which may lead to the budding and segmentation of the membrane-contact site of a chloroplast. Proteins mediating chloroplast segmentation and the interaction between the chloroplast surface and the isolation membrane remain to be uncovered. This study developed a live-cell tracking method for piecemeal-type chloroplast autophagy, which will help future studies elucidate the underlying mechanisms of the intracellular dynamics of this type of autophagy.

556 **Materials and Methods**

557 **Plant materials**

558 Arabidopsis (*Arabidopsis thaliana*) plants from the Columbia accession (Col) were used in this
559 study. Plants were grown in soil in growth chambers at 23°C under a 12-h-light/12-h-dark
560 photoperiod with illumination from fluorescent lamps or LEDs (90–130 μmol m^{-2} s^{-1}). The T-
561 DNA-insertion mutants for *ATG5* (*atg5-1*; SAIL_129_B07), *ATG7* (*atg7-2*; GABI_655B06),
562 *ATG2* (*atg2-1*; SALK_076727), *ATG10* (*atg10-1*; SALK_084434), and *DRP5B* (*arc5-2*;
563 SAIL_71_D11) have been described previously (Doelling et al., 2002; Thompson et al., 2005;
564 Miyagishima et al., 2006; Phillips et al., 2008; Yoshimoto et al., 2009). The *sid2-2* mutant and a
565 transgenic line expressing NahG have been reported previously (Delaney et al., 1994;
566 Yoshimoto et al., 2009). The transgenic plants expressing a construct encoding chloroplast
567 stroma–targeted GFP (GFP fused to the transit peptide of RECA protein) under the control of
568 the cauliflower mosaic virus (CaMV) 35S promoter (*Pro35S:CT-GFP*; Kohler et al., 1997),
569 chloroplast stroma–targeted DsRed (DsRed fused to the transit peptide of RECA protein) from
570 the CaMV 35S promoter (*Pro35S:CT-DsRed*; Ishida et al., 2021), RBCS2B-GFP from the
571 Arabidopsis *RBCS2B* promoter (*ProRBCS:RBCS-GFP*; Ishida et al., 2008), VHP1-mGFP from
572 the Arabidopsis *VHP1* promoter (*ProVHP1:VHP1-mGFP*; Segami et al., 2014), GFP-ATG8a
573 from the Arabidopsis *UBQ10* promoter (*ProUBQ:GFP-ATG8a*; Nakamura et al., 2021b), and
574 TOC64-mRFP from the Arabidopsis *TOC64* promoter (*ProTOC64:TOC64-mRFP*; Kusano et al.,
575 2023) have been reported in previous studies. Transgenic plants expressing *RBCS2B-EYFP*,
576 *RBCS2B-mRFP*, or *RBCS2B-tagRFP* from the *RBCS2B* promoter (*ProRBCS:RBCS-EYFP*,
577 *ProRBCS:RBCS-mRFP*, and *ProRBCS:RBCS-tagRFP*) were generated as follows. A genomic
578 fragment encompassing the promoter region and the full-length coding region of *RBCS2B*
579 (At5g38420), cloned into the pENTR/D/TOPO vector (Ishida et al., 2008), was inserted into the
580 Gateway vectors pGWB540, pGWB553, or pGWB559 (Nakagawa et al., 2007) via LR clonase
581 (Invitrogen) reaction to generate constructs encoding RBCS2B-EYFP, RBCS2B-mRFP, or
582 RBCS2B-tagRFP, respectively.

583 Transgenic plants expressing *ATPC1-tagRFP* (*ProATPC1:ATPC1-tagRFP*) were
584 produced as follows. A genomic fragment containing the promoter region and full-length coding
585 region of *ATPC1* (At4g04640) was amplified from Col-0 genomic DNA by PCR using
586 PrimeSTAR DNA polymerase (TaKaRa) and the primers ATPC1_F
587 (CACCCATGGAGAGGGCTCGTACCTTAC) and ATPC1_R
588 (AACCTGTGCATTAGCTCCAG), cloned into pENTR/D-TOPO (Invitrogen), and then
589 recombined into the vector pGWB559 via LR reaction. Transgenic plants expressing *KEA1-*
590 *mRFP* (*ProKEA1:KEA1-mRFP*) were produced as follows. A genomic fragment containing the
591 promoter region and full-length coding region of *KEA1* (At1g01790) was amplified from Col-0
592 genomic DNA by PCR using the primers KEA1_F
593 (AGGAACCAATTCAGTCGACTCATGATCATAACAAGTCTC) and KEA1_R
594 (AAAGCTGGGTCTAGATATCCGATTACGACTGTGCCTCCTTC), cloned into pENTR1A
595 (Invitrogen) using NEBuilder HiFi DNA Assembly master mix (New England Biolabs), and
596 recombined into the vector pGWB553 via LR reaction. The resulting construct was introduced
597 into Arabidopsis plants by the floral dip method (Clough and Bent, 1998) using Agrobacterium
598 (*Agrobacterium tumefaciens*) strain GV3101. Transgenic plants expressing two types of
599 fluorescent markers and mutant plants expressing fluorescent markers were generated by
600 crossing or additional transformations.

601

602 **Live-cell imaging by confocal microscopy**

603 The second rosette leaves of 20- to 24-d-old plants were used for time-lapse imaging of living
604 cells. The leaves were excised, infiltrated with sugar-free solutions, and incubated in darkness
605 for 5 to 24 h, followed by confocal microscopy observations. When the dark treatment was
606 started at the end of the night, the incubation time was around 5–9 h. When the treatment was

607 started during the light period, the incubation time was around 20–24 h. The sugar-free solutions
608 contained 10 mM MES-NaOH, pH 5.5, alone or with full-strength Murashige and Skoog salts
609 (Shiotani M. S.) or the photosynthesis inhibitor 3-(3,4-dichlorophenyl)-1,1-dimethylurea
610 (DCMU).
611 Time-lapse imaging in Figure 1 was performed as previously described with a two-
612 photon excitation confocal microscope with a spinning-disk unit (Otomo et al. 2015). The GFP
613 signal was excited by 920-nm femtosecond light pulses generated by a mode-locked titanium-
614 sapphire laser light source (Mai Tai eHP DeepSee; Spectra Physics). The YFP, RFP, and
615 chlorophyll signals were excited by 1040-nm femtosecond light pulses generated by an
616 ytterbium laser light source (femtoTrain; Spectra Physics). The fluorescent signals were
617 observed under an inverted microscope (IX-71; Olympus) equipped with a spinning-disk
618 scanner with 100-μm-wide pinholes aligned with a Nipkow disk (CSU-MPϕ100; Yokogawa
619 Electric) and a water-immersion lens (UPLSAPO60XW, numerical aperture [NA] = 1.20,
620 Olympus). The fluorescence images were captured by an EM-CCD camera (EM-C2; Qimaging
621 or iXon Ultra 897; Andor Technology) through a bandpass filter for GFP and YFP (BrightLine
622 528/38; Semrock), RFP (D630/60M; Chroma Technology), or chlorophyll autofluorescence
623 (BrightLine 685/40; Semrock). For the simultaneous detection of YFP and chlorophyll signals,
624 fluorescence was detected through image-splitting optics (W-View Gemini; Hamamatsu
625 Photonics) including a dichroic mirror (FF580-FDi01-25 36; Semrock) and the bandpass filters.
626 Z-Scans were performed with a piezo actuator (P-721; PI). The acquired images were processed
627 and analyzed using NIS-Elements C software (Nikon) or Imaris software (Bitplane).
628 Time-lapse imaging analysis by confocal laser-scanning microscopy was performed
629 with LSM800 (Carl Zeiss), LSM880 (Carl Zeiss), LSM900 (Carl Zeiss), or SP8 (Leica) systems.
630 A water-immersion objective lens (C-Apochromat 40x, NA = 1.2 or LD C-Apochromat 63x, NA
631 = 1.15; Carl Zeiss) or an oil-immersion objective lens (HC PL APO 63x, NA = 1.40, Leica) was
632 used. Fast Airyscan mode was used for the observation displayed in Figure 4B with the
633 LSM880 system.
634
635 **Quantification of microscopy images**
636 Confocal images used for the quantification of RCB numbers (Figure 1–figure supplement 1,
637 Figure 5, Figure 8), chloroplast protrusions (Figure 5), stromules (Figure 7), or vacuolar RFP
638 intensity (Figure 8–figure supplement 2) were acquired with a C2 system (Nikon) equipped with
639 a water-immersion objective lens (CFI Apochromat LWD Lambda S 40XC, NA = 1.15; Nikon).
640 RFP emission was detected at 580–630 nm (bandpass filter RPB580–630; Omega optical) after
641 excitation with a 559.8-nm diode laser; chlorophyll autofluorescence was detected at 660–720
642 nm following excitation by a 636.5-nm diode laser; the two signals were detected
643 simultaneously. For the simultaneous detection of GFP and chlorophyll, GFP emission was
644 detected at 500–550 nm (bandpass filter RPB500–550; Omega Optical) following excitation by
645 a 489.6-nm diode laser; chlorophyll autofluorescence was detected at 660–720 nm following
646 excitation by a 489.6-nm diode laser.
647 For the quantification of RCBs and chloroplast protrusions, the second rosette leaves
648 of 21-d-old plants were excised, infiltrated with 10 mM MES-NaOH, pH 5.5, containing 1 μM
649 concanamycin A (Santa Cruz), and incubated for 1 d in darkness at 23°C. The stock solution
650 was 100 μM concanamycin A in DMSO. Sucrose (1%, w/v) or full-strength MS salts was added
651 as energy source or nutrients, respectively. The number of accumulated RCBs in a fixed area
652 (215.04 × 215. 04 μm each) was counted. The mean number from four areas of one second
653 rosette leaf per plant was calculated from four or five independent plants. The *z*-stack images of
654 the 3D region (215.04 × 215.04 × 15 μm each) were observed, and the proportion of
655 chloroplasts forming protrusions out of 50 chloroplasts was scored in the region. The protruding
656 structures of chloroplast stroma (approximately 0.5 to 1.5 μm long) containing the chloroplast
657 stroma marker RBCS-mRFP without the chlorophyll signal were defined as chloroplast

658 protrusions in Figure 5. The mean from two different regions of one second rosette leaf per plant
659 was calculated from four independent plants.
660 Chloroplast stromule formation in guard cells was observed in the second rosette
661 leaves of 13-d-old seedlings. The proportion of chloroplasts forming stromules in each pair of
662 guard cells was scored from the *z*-stack images (251.04 × 251.04 × 20 μm each). The mean
663 from 10 stomata of one second rosette leaf per plant was calculated from three individual
664 seedlings. Chloroplast stromule formation in mesophyll cells was observed in the third rosette
665 leaves of 20- or 36-d-old plants. The proportion of chloroplasts forming stromules out of 50
666 chloroplasts was scored in the *z*-stack images (215.04 × 215.04 × 15 μm each). The mean from
667 two different regions of one third rosette leaf per plant was calculated from four individual
668 plants. Thin, extended tubular structures (less than 1 μm in diameter) containing a chloroplast
669 stroma marker (CT-GFP or RBCS-mRFP) without chlorophyll signals were defined as
670 stromules, as described previously (Hanson and Sattarzadeh, 2011; Brunkard et al., 2015). For
671 the quantification of vacuolar RFP intensity, the second rosette leaves of 21-d-old plants were
672 excised and incubated in 10 mM MES-NaOH, pH 5.5, for 2 d in darkness at 23°C. The RFP
673 intensity in the central area of a mesophyll cell (15.2 × 15.2 μm each) was measured. The mean
674 from 12 cells of one second rosette leaf per plant was calculated from four individual plants.
675 Confocal images used to evaluate chloroplast stroma volume (Figure 1-figure
676 supplement 2), chloroplast buds, and GFP-ATG8a-labeled structures (Figure 2–figure
677 supplement 1; Figure 6–figure supplement 3 and 4) were acquired with an LSM900 (Carl Zeiss)
678 or SP8 (Leica) system. To quantify chloroplast stroma volume, the second rosette leaves of 21-
679 d-old plants accumulating RBCS-mRFP were excised at dawn, infiltrated with 10 mM MES-
680 NaOH, pH 5.5, and incubated for 24 h in the dark at 23°C. The *z*-stack images of the 3D region
681 (159.73 × 159.73 × 30 μm each) were acquired, and the volumes of the respective chloroplasts
682 whose entire bodies were captured in the image and could be separated from neighboring
683 chloroplasts as a single structure were measured using Imaris software (Bitplane). Two different
684 regions of one second rosette leaf were observed in five individual plants. Leaves were observed
685 before incubation in the dark as a control. To quantify chloroplast buds, the second rosette
686 leaves of 21- to 23-d-old plants were excised at dawn, infiltrated with 10 mM MES-NaOH, pH
687 5.5, and incubated for 5 to 9 h in the dark at 23°C. The regions with RBCS-GFP, TOC64-mRFP,
688 KEA1-mRFP, ATPC1-tagRFP, or chlorophyll signals within a chloroplast bud and its
689 neighboring chloroplast or chloroplast envelope were selected as the regions of interest, and the
690 fluorescence intensities per unit area were measured in eight individual plants (Figure 2–figure
691 supplement 1). The number of chloroplast buds surrounded by GFP-ATG8a signal in four *z*-
692 stack images (159.73 × 159.73 × 20 μm each) of one leaf per plant was scored from five to six
693 individual plants (Figure 6–figure supplement 3D and 3E).
694
695
696 **Protein analysis**
697 The second and third rosette leaves of 21-d-old plants were incubated in darkness in 10 mM
698 MES-NaOH, pH 5.5, for 2 d and then frozen in liquid nitrogen. The leaves from 23-d-old,
699 untreated plants were used as control. The frozen leaves were homogenized using a tissue laser
700 (Qiagen) and a zirconium bead, before being resuspended in homogenization buffer containing
701 50 mM HEPES-NaOH, pH 7.5, 16 mM DTT, 10% (v/v) glycerol, and protease inhibitor cocktail
702 (Nacalai). Following centrifugation at 20,630 *g* for 10 min at 4°C, the protein amounts in the
703 supernatants were measured using a 660-nm Protein Assay Reagent (Pierce). The supernatants
704 were then mixed with an equal volume of SDS sample buffer containing 200 mM Tris-HCl, pH
705 8.5, 20% (v/v) glycerol, 2% (w/v) SDS, and 0.1 M DTT, and incubated for 5 min at 95°C. An
706 equal amount of protein was subjected to SDS-PAGE using TGX FastCast acrylamide gels
707 (Bio-Rad) and transferred to nitrocellulose membrane (Trans-blot turbo transfer pack; Bio-Rad).
708 An anti-RFP 1G9 clone antibody (1:2000, M204-3; MBL) and an anti-cFBPase antibody

(1:5000, AS04043; Agrisera) were used as primary antibodies. Goat anti-mouse IgG (H+L) secondary antibody DyLight 800 4X PEG (1:10,000, SA5-35521; Invitrogen) or anti-rabbit HRP secondary antibody (1:10,000, NA934; Cytiba) was used for RFP or cFBPase detection, respectively. The chemiluminescence signals developed with SuperSignal West Dura Extended Duration Substrate (Pierce) and the DyLight 800 fluorescent signals were detected by a ChemiDoc MP system (Bio-Rad). The image processing and the quantification of band intensity were performed using Image Lab Software (Bio-Rad).

H_2O_2 measurements

The amount of H_2O_2 in leaf lysates was measured as previously described (Chakraborty et al., 2016) with an Amplex Red Hydrogen Peroxide/Peroxidase Assay Kit (Invitrogen) and an Infinite 200 PRO plate reader (Tecan).

Statistical analysis

Statistical analysis in this study was performed with JMP14.3.0 software (SAS Institute). Student's *t*-test or Tukey's test was used to compare paired samples or multiple samples, respectively.

Acknowledgements

We thank Emi Sone, Izumi Fukuhara, and Mio Tokuda for their technical support. We thank Dr. Kohki Yoshimoto for the use of *atg*, *sid2*, and NahG plants, Dr. Maureen R. Hanson for the use of *Pro35S:CT-GFP* plants, Dr. Shoji Segami for the use of the *ProVHP1:VHP1-mGFP* construct, and Dr. Tsuyoshi Nakagawa for the use of pGWB vectors.

Figure legends

Figure 1. Chloroplast buds are released in sugar-starved leaves.

Time-lapse observations of 3D-reconstructed chloroplast morphology in Arabidopsis mesophyll cells accumulating chloroplast stroma–targeted fluorescent markers. A leaf from a plant accumulating chloroplast stroma–targeted GFP (CT-GFP) (A), RBCS-mRFP (B), or RBCS-EYFP (C) was incubated in sugar-free solution in darkness for 5 h from dawn (A), 21 h (B), or 24 h from the period in light (C) and then observed through a two-photon excitation microscope equipped with a confocal spinning-disk unit. Second rosette leaves from 20- to 22-d-old plants were used. Images in (A–C) are still frames from Videos 1, 2, and 3, respectively. Time scales above the images indicate the elapsed time from the start of the respective videos. Arrowheads indicate chloroplast budding structures. Scale bars, 5 µm. In (C), green, RBCS-EYFP; magenta, chlorophyll fluorescence. In the merged images, the overlapping regions of RBCS-EYFP and chlorophyll signals appear white.

Figure 1–figure supplement 1. Accumulation of chloroplast stroma components in the vacuole via autophagy.

Confocal images of mesophyll cells from wild-type (A) or *atg7* (B) plants accumulating the chloroplast stroma marker RBCS-mRFP. Second rosette leaves of 21-d-old plants were excised and incubated in 10 mM MES-NaOH containing 1 µM concanamycin A (concA) in darkness for 1 d. Sucrose (Suc) or Murashige and Skoog (MS) salts were added as an energy or nutrient source, respectively. Second rosette leaves from nontreated plants are shown as control. Green, RBCS-mRFP; magenta, chlorophyll fluorescence. Scale bars, 10 µm. The small puncta containing RBCS-mRFP without chlorophyll signal appear green and are Rubisco-containing bodies (RCBs) in the vacuole. (C) Number of accumulated RCBs from the observations described in (A) and (B). Different lowercase letters denote significant differences based on Tukey's test ($P < 0.05$). Values are means ± SE ($n = 4$). Dots represent individual data points.

759
760 **Figure 1–figure supplement 2. The release of chloroplast buds by autophagy contributes to**
761 **the decline in chloroplast stroma volume.**
762 (A) Orthogonal projections produced from *z*-stack images (30 μm in depth) of mesophyll cells
763 from WT or *atg7* leaves accumulating the chloroplast stroma marker RBCS-mRFP. Second
764 rosette leaves of 21-d-old plants were excised at dawn and incubated in 10 mM MES-NaOH in
765 the dark for 24 h. Mesophyll cells were observed before (0 h) and after (Dark 24 h) the
766 treatment. Green, RBCS-mRFP. Scale bars, 10 μm. (B) Violin plot showing the volume of
767 chloroplast stroma labeled by RBCS-mRFP, measured from the observations described in (A).
768 Different lowercase letters denote significant differences based on Tukey's test ($P < 0.05$).
769 Yellow bars indicate mean values. Five individual plants were observed, and the volumes of 564
770 (WT, 0 h), 554 (WT, dark 24 h), 597 (*atg7*, 0 h), and 725 (*atg7*, dark 24 h) chloroplasts were
771 scored.
772
773 **Video 1. Release of a chloroplast bud as visualized by chloroplast stroma–targeted GFP.**
774 The second rosette leaf from a 21-d-old plant accumulating the chloroplast stroma–targeted GFP
775 (CT-GFP) was incubated in sugar-free solution in darkness for time-lapse imaging with a two-
776 photon excitation microscope equipped with a confocal spinning-disk unit. Arrowhead indicates
777 a chloroplast budding structure. 3D-reconstructed images (8 μm in depth) acquired about every
778 3 s are displayed at 10 frames/s. Scale bar, 5 μm. This video was used to generate Figure 1A.
779
780 **Video 2. Release of a chloroplast bud as visualized by RBCS-mRFP**
781 The second rosette leaf from a 22-d-old plant accumulating the chloroplast stroma marker
782 RBCS-mRFP was incubated in sugar-free solution in darkness for time-lapse imaging with a
783 two-photon excitation microscope equipped with a confocal spinning-disk unit. Arrowhead
784 indicates a chloroplast budding structure. 3D-reconstructed images (2 μm in depth) acquired
785 about every 1.2 s are displayed at 10 frames/s. Scale bar, 5 μm. This video was used to generate
786 Figure 1B.
787
788 **Video 3. Tracking of the stroma marker and chlorophyll fluorescence during the release of**
789 **a chloroplast bud.**
790 The second rosette leaf from a 20-d-old plant accumulating the chloroplast stroma marker
791 RBCS-EYFP was incubated in sugar-free solution in darkness for time-lapse imaging with a
792 two-photon excitation microscope equipped with a confocal spinning-disk unit. Arrowhead
793 indicates a chloroplast budding structure. 3D-reconstructed images (8 μm in depth) acquired
794 every 4 s are displayed at 10 frames/s. Scale bar, 5 μm. Green, RBCS-EYFP; magenta,
795 chlorophyll fluorescence. Only the video of the merged channels is shown. The overlapping
796 regions of RBCS-EYFP and chlorophyll signals appear white. This video was used to generate
797 Figure 1C.
798
799 **Figure 2. Chloroplast buds containing stroma and envelope components are released from**
800 **the chloroplasts.**
801 Time-lapse observations of Arabidopsis mesophyll cells accumulating the chloroplast stroma
802 marker along with an envelope marker or a thylakoid membrane marker. Leaves accumulating
803 stromal RBCS-GFP along with outer envelope–bound TOC64-mRFP (A and B) or with
804 thylakoid membrane–bound ATPC1-tagRFP (C and D) were incubated in sugar-free solution in
805 darkness for 5 to 9 h from dawn and then observed. Second rosette leaves from 21- to 22-d-old
806 plants were used. Images in (B) or (D) are still frames from Videos 4 and 6, respectively. Time
807 scales above the images indicate the elapsed time from the start of the respective videos.
808 Arrowheads indicate chloroplast budding structures. Scale bars, 5 μm. Green, TOC64-mRFP or
809 ATPC1-tagRFP; magenta, RBCS-GFP; orange, chlorophyll (Chl) fluorescence. The graphs in

(A and C) show fluorescence intensities along the blue lines (a to b) in the magnified images of the area indicated by dashed blue boxes. The intensities are shown relative to the maximum intensity for each fluorescence channel, set to 1.

Figure 2–figure supplement 1. Chloroplast buds contain stroma and envelope proteins.
Second rosette leaves accumulating stromal RBCS-GFP along with outer envelope membrane–bound TOC64-mRFP (A), inner envelope membrane–bound KEA1-mRFP (B), or thylakoid membrane–bound ATPC1-tagRFP (C) were incubated in sugar-free solution in the dark for 5 to 9 h from dawn, and chloroplast budding structures were observed. Second rosette leaves from 21- to 22-d-old plants were used. Arrowheads indicate chloroplast budding structures. Four representative images of chloroplast buds are shown for each plant line. Scale bars, 5 µm. Green, TOC64-mRFP, KEA1-mRFP, or ATPC1-tagRFP; magenta, RBCS-GFP; orange, chlorophyll (Chl) fluorescence. The graphs show the relative ratio of GFP, RFP, or chlorophyll fluorescence intensity per unit area within chloroplast budding structures vs. their neighboring chloroplasts (bud/chloroplast). The intensities from 33 (A), 32 (B), or 30 (C) chloroplast buds from 8 individual plants were measured. Values are means ± SE (n = 30–33). Dots represent individual data points in each graph.

Figure 2–figure supplement 2. A released chloroplast bud contains an inner envelope marker protein.
Time-lapse observations of Arabidopsis mesophyll cells accumulating the chloroplast stroma marker RBCS-GFP along with inner envelope membrane–bound KEA1-mRFP. The second rosette leaf from a 22-d-old plant was incubated in sugar-free solution in the dark for 6 h from dawn and observed. The images are still frames from Video 5. Time scales above the images indicate the elapsed time from the start of the video. Arrowheads indicate chloroplast budding structures. Scale bars, 5 µm. Green, KEA1-mRFP; magenta, RBCS-GFP; orange, chlorophyll (Chl) fluorescence.

Video 4. A released chloroplast bud contains the outer envelope marker TOC64-mRFP.
The second rosette leaf from a 21-d-old plant accumulating the chloroplast stroma marker RBCS-GFP and the outer envelope marker TOC64-mRFP was incubated in sugar-free solution in darkness for time-lapse imaging. Arrowheads indicate chloroplast budding structures. Images acquired every 2 s are displayed at 10 frames/s. Scale bar, 5 µm. Green, TOC64-mRFP; magenta, RBCS-GFP. The video contains TOC64-mRFP and the merged channels. This video was used to generate Figure 2B.

Video 5. A released chloroplast bud contains the inner envelope marker KEA1-mRFP.
The second rosette leaf from a 22-d-old plant accumulating the chloroplast stroma marker RBCS-GFP and the inner envelope marker KEA1-mRFP was incubated in sugar-free solution in the dark for time-lapse imaging. Arrowheads indicate chloroplast budding structures. Images acquired every 2 s are displayed at 10 frames/s. Scale bar, 5 µm. Green, KEA1-mRFP; magenta, RBCS-GFP. The video contains KEA1-mRFP and the merged channels. This video was used to generate Figure 2–figure supplement 2.

Video 6. A released chloroplast bud does not contain the thylakoid membrane marker ATPC1-tagRFP.
The second rosette leaf from a 21-d-old plant accumulating the chloroplast stroma marker RBCS-GFP and the thylakoid membrane marker ATPC1-tagRFP was incubated in sugar-free solution in darkness for time-lapse imaging. Arrowheads indicate chloroplast budding structures. Images acquired every 2 s are displayed at 10 frames/s. Scale bar, 5 µm. Green, ATPC1-tagRFP; magenta, RBCS-GFP. The video contains ATPC1-tagRFP and the merged channels. This video

861 was used to generate Figure 2D.
862
863 **Figure 3. Tracking the transport of a Rubisco-containing body.**
864 A leaf accumulating chloroplast stroma–targeted GFP (CT-GFP) was incubated in sugar-free
865 solution in darkness for 6 h from dawn, and the transport of a Rubisco-containing body (RCB)
866 was tracked. The second rosette leaf from a 21-d-old plant was used. (A) Confocal images
867 during the periods when the RCB moved quickly (24.4–34.8 and 73.8–90.5 s). Arrowheads
868 indicate an RCB. The images are still frames from Video 7. Time scales above the images
869 indicate the elapsed time from the start of the video. Green, CT-GFP; magenta, chlorophyll
870 (Chl) fluorescence. Scale bar, 5 µm. (B) Calculated speed of the tracked RCB in (A). (C) The
871 track of the RCB. The color of the track line changes over time, as indicated by the color bar.
872 Scale bar, 2 µm.
873
874 **Video 7. Tracking of a Rubisco-containing body marked by CT-GFP.**
875 The second rosette leaf from a 21-d-old plant accumulating chloroplast stroma–targeted GFP
876 (CT-GFP) was incubated in sugar-free solution in darkness for time-lapse monitoring of an RCB
877 marked by CT-GFP. Arrowhead indicates an RCB. Images acquired every 0.52 s are displayed
878 at 20 frames/s. Scale bar, 5 µm. Green, CT-GFP; magenta, chlorophyll fluorescence. Only the
879 video of the merged channels is shown. This video was used to generate Figure 3A.
880
881 **Figure 3–figure supplement 1. Rubisco-containing bodies appear to begin random**
882 **movement during their tracking.**
883 A leaf accumulating RBCS-tagRFP (A) or RBCS-EYFP (B) was incubated in sugar-free
884 solution in the dark for 7 to 8 h from dawn, and the transport of a Rubisco-containing body was
885 tracked. Second rosette leaves from 22-d-old plants were used. Arrowheads indicate a tracked
886 RCB. The images are still frames from Videos 8 (A) or 9 (B), respectively. The images show the
887 time when RCBs appeared to begin random movement (185–197 s in A or 25–33 s in B). Time
888 scales above the images indicate the elapsed time from the start of the respective videos. Green,
889 RBCS-tagRFP or RBCS-EYFP; magenta, chlorophyll fluorescence. Scale bars, 5 µm. The color
890 of the track line changes over time, as indicated by the color bars below the images.
891
892 **Video 8. Tracking of a Rubisco-containing body marked by RBCS-tagRFP.**
893 The second rosette leaf from a 22-d-old plant accumulating stromal RBCS-tagRFP was
894 incubated in sugar-free solution in the dark for time-lapse monitoring of an RCB marked by
895 RBCS-tagRFP. Arrowhead indicates an RCB. Images acquired every 1 s are displayed at 20
896 frames/s. Scale bar, 5 µm. Green, RBCS-tagRFP; magenta, chlorophyll fluorescence. Only the
897 video of the merged channels is shown. This video was used to generate Figure 3–figure
898 supplement 1A.
899
900 **Video 9. Tracking of a Rubisco-containing body marked by RBCS-EYFP.**
901 The second rosette leaf from a 22-d-old plant accumulating stromal RBCS-EYFP was incubated
902 in sugar-free solution in the dark for time-lapse monitoring of an RCB marked by RBCS-EYFP.
903 Arrowhead indicates an RCB. Images acquired every 1 s are displayed at 10 frames/s. Scale bar,
904 5 µm. Green, RBCS-EYFP; magenta, chlorophyll fluorescence. Only the video of the merged
905 channels is shown. This video was used to generate Figure 3–figure supplement 1B.
906
907 **Figure 4. Dynamics of the vacuolar membrane during the incorporation of Rubisco-**
908 **containing bodies.**
909 Leaves accumulating the chloroplast stroma marker RBCS-mRFP along with the vacuolar
910 membrane marker VHP1-mGFP were incubated in sugar-free solution in darkness for 6 to 8 h
911 from dawn, and the behavior of cytosolic RCBs was monitored. Second rosette leaves from 21-

or 23-d-old plants were used. The images when the vacuolar membrane engulfs an RCB (25.4–30.5 s in A and 52.6–57.4 s in B) and when an RCB is incorporated into the vacuolar lumen (47.0–52.0 s in A and 65.3–72.9 s in B) are shown. The images in (A) and (B) are still frames from Videos 10 and 11, respectively. Time scales above the images indicate the elapsed time from the start of the respective videos. Open arrowheads indicate an RCB engulfed by the vacuolar membrane. Closed arrowheads indicate the open site of the vacuolar membrane for the incorporation of an RCB. V indicates the region of the vacuolar lumen. Green, VHP1-mGFP; magenta, RBCS-mRFP. Scale bars, 5 µm.

Video 10. Incorporation of a Rubisco-containing body into the vacuolar lumen.
The second rosette leaf from a 21-d-old plant accumulating the chloroplast stroma marker RBCS-mRFP along with the vacuolar membrane marker VHP1-mGFP was incubated in sugar-free solution in darkness for time-lapse imaging. Arrowhead indicates an RCB incorporated into the vacuolar lumen. Images acquired every 1.27 s are displayed at 10 frames/s. Scale bar, 5 µm. Green, VHP1-mGFP; magenta, RBCS-mRFP. Only the video of the merged channels is shown. This video was used to generate Figure 4A.

Video 11. Video 2 of the vacuolar incorporation of a Rubisco-containing body.
Additional time-lapse data for the experiment described in Figure 4 and Video 10. The second rosette leaf from a 23-d-old plant was used. Arrowhead indicates an RCB incorporated into the vacuolar lumen. Images acquired every 0.317 s are displayed at 25 frames/s. Scale bar, 5 µm. Green, VHP1-mGFP; magenta, RBCS-mRFP. Only the video of the merged channels is shown. This video was used to generate Figure 4B.

Figure 4–figure supplement 1. Additional observations of the incorporation of Rubisco-containing bodies into the vacuolar lumen.
Additional time-lapse data of the experiments described in Figure 4. The second rosette leaves from 21- (A) or 24-d-old (B, C) plants were used. The images in (A), (B), and (C) are still frames from Videos 12, 13, and 14, respectively. Time scales above the images indicate the elapsed time from the start of the respective videos. Open arrowheads indicate an RCB engulfed by the vacuolar membrane. Closed arrowheads indicate the vacuolar membrane structure that engulfs an RCB. V indicates the region of the vacuolar lumen. Green, VHP1-mGFP; magenta, RBCS-mRFP. Scale bars, 5 µm.

Video 12. Video 3 of the vacuolar incorporation of a Rubisco-containing body.
Additional time-lapse data for the experiment described in Figure 4 and Video 10. Arrowhead indicates an RCB incorporated into the vacuolar lumen. Images acquired every 1.5 s are displayed at 10 frames/s. Scale bar, 5 µm. Green, VHP1-mGFP; magenta, RBCS-mRFP. Only the video of the merged channels is shown. This video was used to generate Figure 4–figure supplement 1A.

Video 13. Video 4 of the vacuolar incorporation of a Rubisco-containing body.
Additional time-lapse data for the experiment described in Figure 4 and Video 10. Arrowhead indicates an RCB incorporated into the vacuolar lumen. Images acquired every 1.5 s are displayed at 10 frames/s. Scale bar, 5 µm. Green, VHP1-mGFP; magenta, RBCS-mRFP. Only the video of the merged channels is shown. This video was used to generate Figure 4–figure supplement 1B.

Video 14. Video 5 of the vacuolar incorporation of a Rubisco-containing body.
Additional time-lapse data for the experiment described in Figure 4 and Video 10. Arrowhead indicates an RCB incorporated into the vacuolar lumen. Images acquired every 1.5 s are

displayed at 10 frames/s. Scale bar, 5 μm. Green, VHP1-mGFP; magenta, RBCS-mRFP. Only the video of the merged channels is shown. This video was used to generate Figure 4–figure supplement 1C.

Figure 5. Autophagy deficiency does not increase the number of chloroplast protrusions during a 1-d dark treatment.

Leaves from wild-type (WT), *atg5*, or *atg7* plants accumulating the chloroplast stroma marker RBCS-mRFP were incubated in sugar-free solution containing 1 μM concanamycin A (concA) for 1 d in darkness. Second rosette leaves from 21-d-old plants were used. 2D images of mesophyll cells were acquired (A), and the number of accumulated RCBs in the vacuoles was scored (B). Small puncta containing RBCS-mRFP without the chlorophyll signal appear green and are RCBs in the vacuole. Leaves from untreated plants are shown as control. The appearance of chloroplast protrusions was observed from orthogonal projections created from *z*-stack images (15 μm in depth; C), and the proportion of chloroplasts forming protrusion structures out of 50 chloroplasts was scored (D). Scale bars, 10 μm. Green, RBCS-mRFP; magenta, chlorophyll fluorescence. Only the merged channels are shown. The overlapping regions of RBCS-mRFP and chlorophyll signals appear white. Arrowheads indicate the structures that were counted as a chloroplast protrusion in (D). Different lowercase letters denote significant differences based on Tukey's test ($P < 0.05$). Values are means ± SE ($n = 4$). Dots represent individual data points in each graph.

Figure 5–figure supplement 1. Chloroplast protrusions do not increase in *atg2* or *atg10* mutant leaves during a 1-d dark treatment.

The experiments described in Figure 5 were performed on leaves from wild-type (WT), *atg2*, or *atg10* plants accumulating the chloroplast stroma marker RBCS-mRFP. Scale bars, 10 μm. Green, RBCS-mRFP; magenta, chlorophyll fluorescence. Only the merged channels are shown. The overlapping regions of RBCS-mRFP and chlorophyll signals appear white. Small puncta containing RBCS-mRFP without chlorophyll signal appear green and are RCBs in the vacuole. Arrowheads indicate the structures that were counted as a chloroplast protrusion in (D). Different lowercase letters denote significant differences based on Tukey's test ($P < 0.05$). Values are means ± SE ($n = 4$). Dots represent individual data points in each graph.

Figure 6. The formation of a chloroplast bud and the maturation of the chloroplast-associated isolation membrane occur concomitantly.

Leaves accumulating the chloroplast stroma marker, RBCS-mRFP (A) or CT-DsRed (B), and the isolation membrane marker GFP-ATG8a were incubated in sugar-free solution in darkness for 6 h from dawn (A) or 21 h from the period in light (B) and then observed. Second rosette leaves from 23-d-old plants were used. Arrowheads indicate the position of the chloroplast-associated isolation membrane. Images in (A) and (B) are still frames from Videos 15 and 16, respectively. Time scales above the images indicate the elapsed time from the start of the respective videos. Green, GFP-ATG8a; magenta, RBCS-mRFP or CT-DsRed. Scale bars, 5 μm. (C) Time-dependent changes in the ratio of the major axis to the minor axis in the GFP-ATG8a-labeled isolation membrane (top) or in the area of the chloroplast budding structure (bottom) as measured from the images in (B).

Video 15. Budding of the isolation membrane–associated site within a chloroplast.

The second rosette leaf from a 23-d-old plant accumulating the chloroplast stroma marker RBCS-mRFP and the isolation membrane marker GFP-ATG8a was incubated in sugar-free solution in darkness for time-lapse imaging. Arrowheads indicate the portion of the chloroplast-associated isolation membrane. Images acquired every 4 s are displayed at 10 frames/s. Scale bar, 5 μm. Green, GFP-ATG8a; magenta, RBCS-mRFP. The video contains RBCS-mRFP and

1014 the merged channels. This video was used to generate Figure 6A.
1015
1016 **Video 16. Autophagosome development and chloroplast segmentation occur concomitantly.**
1017 The second rosette leaf from a 23-d-old plant accumulating the chloroplast stroma–targeted
1018 DsRed (CT-DsRed) and the isolation membrane marker GFP-ATG8a was incubated in sugar-
1019 free solution in darkness for time-lapse imaging. Arrowhead indicates the portion of the
1020 chloroplast-associated isolation membrane. Images acquired every 1 s are displayed at 20
1021 frames/s. Scale bar, 5 µm. Green, GFP-ATG8a; magenta, CT-DsRed. Only the video of the
1022 merged channels is shown. This video was used to generate Figure 6B.
1023
1024 **Figure 6–figure supplement 1. Another observation of the budding of the isolation**
1025 **membrane–associated site in a chloroplast.**
1026 A leaf accumulating the chloroplast stroma marker CT-DsRed and the isolation membrane
1027 marker GFP-ATG8a was incubated in sugar-free solution in darkness for 6 h from dawn and
1028 then observed. A second rosette leaf from a 22-d-old plant was used. Arrowheads indicate the
1029 position of the chloroplast-associated isolation membrane. The images are still frames from
1030 Video 17. Time scales above the images indicate the elapsed time from the start of the video.
1031 Green, GFP-ATG8a; magenta, CT-DsRed. Scale bars, 5 µm. (B) Time-dependent changes in the
1032 ratio of the major axis to the minor axis in the GFP-ATG8a-labeled isolation membrane (top) or
1033 in the area of the chloroplast budding structure (bottom), as measured from the images in (A).
1034
1035 **Figure 6–figure supplement 2. Chloroplast buds surrounded by the isolation membrane**
1036 **appear in multiple chloroplasts.**
1037 A leaf accumulating the chloroplast stroma marker RBCS-tagRFP and the isolation membrane
1038 marker GFP-ATG8a was incubated in sugar-free solution in darkness for 5 h from dawn and
1039 then observed. A second rosette leaf from a 21-d-old plant was used. White, yellow, and blue
1040 arrowheads indicate the isolation membrane–associated site in different chloroplasts,
1041 respectively. The images are still frames from Video 18. Time scales above the images indicate
1042 the elapsed time from the start of the video. Green, GFP-ATG8a; magenta, RBCS-tagRFP;
1043 orange, chlorophyll (Chl) fluorescence. Scale bars, 5 µm.
1044
1045 **Video 17. Another time-lapse assay showing the concomitant progression of**
1046 **autophagosome development and chloroplast segmentation.**
1047 The second rosette leaf from a 22-d-od plant accumulating the chloroplast stroma–targeted
1048 DsRed (CT-DsRed) and the isolation membrane marker GFP-ATG8a was incubated in sugar-
1049 free solution in darkness for time-lapse imaging. Arrowhead indicates the portion of the
1050 chloroplast-associated isolation membrane. Images acquired every 2 s are displayed at 10
1051 frames/s. Scale bar, 5 µm. Green, GFP-ATG8a; magenta, CT-DsRed. Only the video of the
1052 merged channels is shown. This video was used to generate Figure 6–figure supplement 1.
1053
1054 **Video 18. Autophagy-related chloroplast segmentation occurs in sequence.**
1055 The second rosette leaf from a 21-d-old plant accumulating the chloroplast stroma marker
1056 RBCS-tagRFP and the isolation membrane marker GFP-ATG8a was incubated in sugar-free
1057 solution in darkness for time-lapse imaging. White, yellow, and blue arrowheads indicate the
1058 isolation membrane–associated sites in different chloroplasts. Images acquired every 2 s are
1059 displayed at 10 frames/s. Scale bar, 5 µm. Green, GFP-ATG8a; magenta, RBCS-tagRFP. Only
1060 the video of the merged channels is shown. This video was used to generate Figure 6–figure
1061 supplement 2.
1062
1063 **Figure 6–figure supplement 3. Proportion of chloroplast buds engulfed by GFP-ATG8a-**
1064 **labeled isolation membranes.**

1065 Leaves accumulating the chloroplast stroma marker RBCS-mRFP and the isolation membrane
1066 marker GFP-ATG8a were incubated in sugar-free solution in the dark for 5 to 9 h from dawn,
1067 and chloroplast budding structures were observed. Second rosette leaves from 22- to 23-d-old
1068 plants were used. (A and B) Four representative images of chloroplasts buds that are surrounded
1069 by GFP-ATG8a signals (A) or two representative images of chloroplast buds that are not labeled
1070 by GFP-ATG8a signals (B) are shown. Arrowheads indicate chloroplast budding structures.
1071 Green, GFP-ATG8a; magenta, RBCS-mRFP. Scale bars, 5 μm. (C) The proportions of
1072 chloroplast buds that are labeled by GFP-ATG8a signals (+) or not (−) were calculated from
1073 observations of 58 chloroplast buds from 8 individual plants. (D) The number of GFP-ATG8a-
1074 positive chloroplast buds, as shown in (A), were counted in the fixed regions from leaves
1075 incubated in the dark for 5 to 9 h from dawn (Dark) or from untreated leaves of plants grown
1076 under normal conditions (Control). Five individual plants were observed. (E) Leaves from wild-
1077 type (WT) or *atg7* plants accumulating RBCS-mRFP and GFP-ATG8a were incubated in the
1078 dark for 5 to 9 h from dawn, and the number of GFP-ATG8a-positive chloroplast buds was
1079 counted. Six individual plants were observed. Values are means ± SE (n = 5–6). Asterisks
1080 denote significant differences based on t-test (***, $P < 0.001$). Dots represent individual data
1081 points in each graph.
1082
1083 **Figure 6–figure supplement 4. Proportion of GFP-ATG8a-labeled structures that are**
1084 **associated with chloroplasts.**
1085 Leaves accumulating the chloroplast stroma marker RBCS-mRFP and the isolation membrane
1086 marker GFP-ATG8a were incubated in sugar-free solution in the dark for 5 to 9 h from dawn,
1087 and GFP-ATG8a-labeled structures in mesophyll cells were observed. Second rosette leaves
1088 from 22-d-old plants were used. (A to C) GFP-ATG8a-positive structures were classified into
1089 three types: flattened structures associated with the chloroplast surface (A), spherical or curved
1090 structures associated with chloroplast budding structures (B), and other structures (C). Four
1091 representative images of each type are shown. Green, GFP-ATG8a; magenta, RBCS-mRFP.
1092 Scale bars, 5 μm. (D) The proportions of the three types of GFP-ATG8a-labeled structures were
1093 calculated from observations of 157 GFP-ATG8a-labeled structures from 13 individual plants.
1094
1095 **Figure 7. Diminished salicylic acid signal suppresses stromule formation in autophagy-**
1096 **deficient mutants.**
1097 (A) Orthogonal projections produced from z-stack images (10 μm in depth) of guard cells from
1098 wild-type (WT), *atg5*, NahG, and *atg5* NahG leaves accumulating chloroplast stroma–targeted
1099 GFP (CT-GFP). Second rosette leaves from 13-d-old plants were used. Scale bars, 10 μm. (B)
1100 Percentage of chloroplasts forming stromules in 10 stomata, from the observations described in
1101 (A). (C) Orthogonal projections produced from z-stack images (10 μm in depth) of guard cells
1102 from WT, *atg5*, *atg7*, *sid2*, *sid2 atg5*, and *sid2 atg7* leaves accumulating CT-GFP. Scale bars, 10
1103 μm. (D) Percentage of chloroplasts forming stromules in 10 stomata, from the observations
1104 described in (C). (E) Orthogonal projections produced from z-stack images (15 μm in depth) of
1105 mesophyll cells from WT, *atg5*, *atg7*, *sid2*, *sid2 atg5*, and *sid2 atg7* leaves accumulating CT-
1106 GFP. Third rosette leaves from 36-d-old plants were observed. Green, CT-GFP; magenta,
1107 chlorophyll fluorescence. Only the merged channels are shown. Scale bars, 20 μm. (F)
1108 Percentage of chloroplasts forming stromules out of 50 chloroplasts in mesophyll cells, from the
1109 observations described in (E). (G) Hydrogen peroxide (H_2O_2) content in third rosette leaves
1110 from 36-d-old WT, *atg5*, *atg7*, *sid2*, *sid2 atg5*, and *sid2 atg7* plants. Different lowercase letters
1111 denote significant differences based on Tukey's test ($P < 0.05$). Values are means ± SE (n = 3 in
1112 B and D or 4 in F and G). Dots represent individual data points in each graph.
1113
1114 **Figure 7–figure supplement 1. Autophagy deficiency activates stromule formation from**
1115 **mesophyll chloroplasts accumulating RBCS-mRFP in senescing leaves.**

1116 (A) Orthogonal projections produced from *z*-stack images (15 μm in depth) of mesophyll cells
1117 from leaves of WT, *atg5*, and *atg7* plants accumulating RBCS-mRFP. Third rosette leaves from
1118 36-d-old plants were observed. Green, RBCS-mRFP; magenta, chlorophyll fluorescence. Only
1119 the merged channels are shown. Spherical bodies only exhibiting chlorophyll signal represent a
1120 portion of chloroplasts in pavement cells. Scale bars, 20 μm. (B) Percentage of chloroplasts
1121 forming stromules out of 50 chloroplasts in mesophyll cells, from the observations described in
1122 (A). Different lowercase letters denote significant differences based on Tukey's test ($P < 0.05$).
1123 Values are means ± SE ($n = 4$). Dots represent individual data points in the graph.
1124
1125 **Figure 7–figure supplement 2. Autophagy deficiency does not activate stromule formation**
1126 **from mesophyll chloroplasts in young leaves.**
1127 Orthogonal projections produced from *z*-stack images (15 μm in depth) of mesophyll cells from
1128 WT, *atg5*, *atg7*, *sid2*, *sid2 atg5*, and *sid2 atg7* leaves accumulating CT-GFP. Third rosette leaves
1129 from 20-d-old plants were observed. Green, CT-GFP; magenta, chlorophyll fluorescence. Only
1130 the merged channels are shown. Scale bars, 20 μm.
1131
1132 **Figure 7–figure supplement 3. NahG expression does not counteract the increase in**
1133 **hydrogen peroxide content produced by the *atg5* mutation.**
1134 Hydrogen peroxide (H_2O_2) contents in third rosette leaves from 36-d-old plants. WT plants
1135 without any transgenic construct and CT-GFP-expressing plants in the WT, *atg5*, NahG, and
1136 *atg5* NahG backgrounds were used. Different lowercase letters denote significant differences
1137 based on Tukey's test ($P < 0.05$). Values are means ± SE ($n = 4$). Dots represent individual data
1138 points.
1139
1140 **Figure 8. DRP5b is dispensable for chloroplast autophagy in sugar-starved leaves.**
1141 (A) Confocal images of mesophyll cells from wild-type (WT) and *drp5b* leaves accumulating
1142 the stroma marker RBCS-mRFP. Second rosette leaves from 21-d-old plants were incubated in
1143 sugar-free solution containing 1 μM concanamycin A (concA) in darkness for 1 d. Green,
1144 RBCS-mRFP; magenta, chlorophyll fluorescence. Scale bars, 10 μm. (B) Number of
1145 accumulated RCBs in WT, *drp5b*, *atg5*, and *atg7* leaves, counted from the observations of
1146 leaves incubated in the dark with concA described in (A). Different lowercase letters denote
1147 significant differences based on Tukey's test ($P < 0.05$). Values are means ± SE ($n = 4$–5). (C)
1148 Biochemical detection of autophagy flux for chloroplast stroma based on a free RFP assay. RFP
1149 and cFBPase (loading control) were detected by immunoblotting of soluble protein extracts
1150 from leaves of WT, *drp5b*, *atg5*, and *atg7* plants accumulating RBCS-mRFP. Protein extracts
1151 from either untreated control leaves (cont) or leaves after 2 d of incubation in darkness (dark)
1152 were used. Total protein was detected by Coomassie Brilliant Blue (CBB) staining as a loading
1153 control. The filled arrowhead indicates RBCS-mRFP fusion, and the open arrowhead indicates
1154 free mRFP derived from the cleavage of RBCS-mRFP. (D) Quantification of the free
1155 mRFP/RBCS-mRFP ratio shown relative to that of untreated WT plants, which was set to 1.
1156 Asterisks denote significant differences based on *t*-test (***, $P < 0.001$; n.s., not significant).
1157 Values are means ± SE ($n = 4$). Dots represent individual data points in each graph.
1158
1159 **Figure 8–figure supplement 1. Production of Rubisco-containing bodies in *drp5b* mutants**
1160 **is ATG5 dependent.**
1161 (A) Confocal images of mesophyll cells from wild-type (WT), *atg5*, *drp5b*, and *drp5b atg5*
1162 leaves accumulating the stroma marker CT-GFP. Second rosette leaves from 21-d-old plants
1163 were incubated in sugar-free solution containing 1 μM concanamycin A (concA) in darkness for
1164 1 d. Second rosette leaves from untreated plants were used as control. Green, CT-GFP; magenta,
1165 chlorophyll fluorescence. Only the merged channels are shown. Small puncta containing CT-
1166 GFP without chlorophyll signal appear as green and are RCBs in the vacuole. Scale bars, 10 μm.

(B) Number of accumulated RCBs, counted from the observations of leaves incubated in the dark with concA described in (A). Different lowercase letters denote significant differences based on Tukey's test ($P < 0.05$). Values are means ± SE ($n = 5$). Dots represent individual data points.

Figure 8–figure supplement 2. Vacuolar accumulation of stromal marker proteins in sugar-starved leaves.
(A) Confocal images of mesophyll cells from wild-type (WT), *drp5b*, *atg5*, and *atg7* leaves accumulating the stroma marker RBCS-mRFP. Second rosette leaves from 21-d-old plants were incubated in sugar-free solution in darkness for 2 d. Second rosette leaves from untreated plants are shown as control. Green, RBCS-mRFP; magenta, chlorophyll fluorescence. Scale bars, 20 µm. (B) RFP intensity in the vacuolar lumen, as measured from the observations described in (A) and shown relative to that of untreated WT plants, which was set to 1. Asterisks denote significant differences based on *t*-test (***, $P < 0.001$; n.s., not significant). Values are means ± SE ($n = 4$). Dots represent individual data points.

Figure 9. Formation and segmentation of chloroplast buds in leaves of the *drp5b* mutant.
(A) A leaf from the *drp5b* mutant accumulating the stroma marker RBCS-mRFP was incubated in sugar-free solution in darkness for 5 h from dawn and then observed. Arrowheads indicate a chloroplast bud. Green, RBCS-mRFP; magenta, chlorophyll fluorescence (Chl). (B) A leaf from the *drp5b* mutant accumulating the stroma marker RBCS-mRFP and the isolation membrane marker GFP-ATG8a were incubated in sugar-free solution in darkness for 6 h from dawn and then observed. Second rosette leaves from 21- to 22-d-old plants were used. Arrowheads indicate the position of the chloroplast-associated isolation membrane. White and blue arrowheads indicate different isolation membrane–associated sites in a chloroplast. Images in (A) and (B) are still frames from Videos 19 and 20, respectively. Time scales above the images indicate the elapsed time from the start of the respective videos. Green, GFP-ATG8a; magenta, RBCS-mRFP; orange, chlorophyll (Chl) fluorescence. Scale bars, 5 µm.

Video 19. Release of a chloroplast bud in a sugar-starved leaf of the *drp5b* mutant.
The second rosette leaf from a 21-d-old *drp5b* plant accumulating the chloroplast stroma marker RBCS-mRFP was incubated in sugar-free solution in darkness for time-lapse imaging. Arrowhead indicates a chloroplast bud. Images acquired every 1 s are displayed at 20 frames/s. Scale bar, 5 µm. Green, RBCS-mRFP; magenta, chlorophyll fluorescence. Only the video of the merged channels is shown. This video was used to generate Figure 9A.

Video 20. An enlarged chloroplast caused by the *drp5b* mutation forms RCBs along the isolation membrane–associated sites.
The second rosette leaf from a 22-d-old *drp5b* plant accumulating the chloroplast stroma marker RBCS-mRFP and the isolation membrane marker GFP-ATG8a was incubated in sugar-free solution in darkness for time-lapse imaging. White or blue arrowheads indicate different isolation membrane–associated sites in a chloroplast. Images acquired every 2 s are displayed at 20 frames/s. Scale bar, 5 µm. Green, GFP-ATG8a; magenta, RBCS-mRFP. Only the video of the merged channels is shown. This video was used to generate Figure 9B.

References

Abeliovich H, Zarei M, Rigbolt KTG, Youle RJ, Dengjel J (2013) Involvement of mitochondrial dynamics in the segregation of mitochondrial matrix proteins during stationary phase mitophagy. Nat Commun **4:** 2789

Barros JAS, Cavalcanti JHF, Pimentel KG, Magen S, Soroka Y, Weiss S, Medeiros DB,

Nunes-Nesi A, Fernie AR, Avin-Wittenberg T, Araújo WL (2023) The interplay between autophagy and chloroplast vesiculation pathways under dark-induced senescence. Plant Cell Environ **46:** 3721-3736.

Brunkard JO, Runkel AM, Zambryski PC (2015) Chloroplasts extend stromules independently and in response to internal redox signals. Proc Natl Acad Sci U S A **112:** 10044-10049.

Caplan JL, Kumar AS, Park E, Padmanabhan MS, Hoban K, Modla S, Czymmek K, Dinesh-Kumar SP (2015) Chloroplast stromules function during innate immunity. Dev Cell **34:** 45-57

Chakraborty S, Hill AL, Shirsekar G, Afzal AJ, Wang GL, Mackey D, Bonello P (2016) Quantification of hydrogen peroxide in plant tissues using Amplex Red. Methods **109:** 105-113

Chen C, MacCready JS, Ducat DC, Osteryoung KW (2018) The molecular machinery of chloroplast division. Plant Physiol **176:** 138-151

Chen YF, Culetto E, Legouis R (2022) The strange case of Drp1 in autophagy: Jekyll and Hyde? Bioessays **44:** e2100271

Chiba A, Ishida H, Nishizawa NK, Makino A, Mae T (2003) Exclusion of ribulose-1,5-bisphosphate carboxylase/oxygenase from chloroplasts by specific bodies in naturally senescing leaves of wheat. Plant Cell Physiol **44:** 914-921

Clough SJ, Bent AF (1998) Floral dip: a simplified method for Agrobacterium-mediated transformation of Arabidopsis thaliana. Plant J **16:** 735-743

Delaney TP, Uknes S, Vernooij B, Friedrich L, Weymann K, Negrotto D, Gaffney T, Gutrella M, Kessmann H, Ward E, Ryals J (1994) A central role of salicylic-acid in plant-disease resistance. Science **266:** 1247-1250

Doelling JH, Walker JM, Friedman EM, Thompson AR, Vierstra RD (2002) The APG8/12-activating enzyme APG7 is required for proper nutrient recycling and senescence in *Arabidopsis thaliana*. J Biol Chem **277:** 33105-33114

Farre JC, Subramani S (2016) Mechanistic insights into selective autophagy pathways: lessons from yeast. Nat Rev Mol Cell Bio **17:** 537-552

Fukuda T, Ebi Y, Saigusa T, Furukawa K, Yamashita SI, Inoue K, Kobayashi D, Yoshida Y, Kanki T (2020) Atg43 tethers isolation membranes to mitochondria to promote starvation-induced mitophagy in fission yeast. Elife **9:** e61245

Fukuda T, Furukawa K, Maruyama T, Yamashita SI, Noshiro D, Song C, Ogasawara Y, Okuyama K, Alam JM, Hayatsu M, Saigusa T, Inoue K, Ikeda K, Takai A, Chen L, Lahiri V, Okada Y, Shibata S, Murata K, Klionsky DJ, Noda NN, Kanki T (2023) The mitochondrial intermembrane space protein mitofissin drives mitochondrial fission required for mitophagy. Mol Cell **83:** 2045-2058 e2049

Giacomello M, Pyakurel A, Glytsou C, Scorrano L (2020) The cell biology of mitochondrial membrane dynamics. Nat Rev Mol Cell Bio **21:** 204-224

Hanson MR, Sattarzadeh A (2008) Dynamic morphology of plastids and stromules in angiosperm plants. Plant Cell Environ **31:** 646-657

Hanson MR, Sattarzadeh A (2011) Stromules: recent insights into a long neglected feature of plastid morphology and function. Plant Physiol **155:** 1486-1492.

He YL, Gao JY, Luo MQ, Gao CJ, Lin YS, Wong HY, Cui Y, Zhuang XH, Jiang LW (2022) VAMP724 and VAMP726 are involved in autophagosome formation in Arabidopsis thaliana. Autophagy **19:**1406-1423

Hirota T, Izumi M, Wada S, Makino A, Ishida H (2018) Vacuolar protein degradation via autophagy provides substrates to amino acid catabolic pathways as an adaptive response to sugar starvation in *Arabidopsis thaliana*. Plant Cell Physiol **59:** 1363-1376

Ishida H, Izumi M, Wada S, Makino A (2014) Roles of autophagy in chloroplast recycling. Biochim Biophys Acta **1837:** 512-521

Ishida H, Okashita Y, Ishida H, Hayashi M, Izumi M, Makino A, Bhuiyan NH, van Wijk KJ (2021) GFS9 Affects Piecemeal Autophagy of Plastids in Young Seedlings of Arabidopsis thaliana. Plant Cell Physiol **62:** 1372-1386

Ishida H, Yoshimoto K, Izumi M, Reisen D, Yano Y, Makino A, Ohsumi Y, Hanson MR, Mae T (2008) Mobilization of rubisco and stroma-localized fluorescent proteins of chloroplasts to the vacuole by an ATG gene-dependent autophagic process. Plant Physiol **148:** 142-155

Ishida H, Yoshimoto K (2008) Chloroplasts are partially mobilized to the vacuole by autophagy. Autophagy **4:** 961-962

Itakura E, Kishi-Itakura C, Mizushima N (2012) The hairpin-type tail-anchored SNARE Syntaxin 17 targets to autophagosomes for fusion with endosomes/lysosomes. Cell **151:** 1256-1269

Ito E, Uemura T (2022) RAB GTPases and SNAREs at the trans-Golgi network in plants. J Plant Res **135:** 389–403

Izumi M, Hidema J, Wada S, Kondo E, Kurusu T, Kuchitsu K, Makino A, Ishida H (2015) Establishment of monitoring methods for autophagy in rice reveals autophagic recycling of chloroplasts and root plastids during energy limitation. Plant Physiol **167:** 1307-1320

Izumi M, Ishida H, Nakamura S, Hidema J (2017) Entire photodamaged chloroplasts are transported to the central vacuole by autophagy. Plant Cell **29:** 377-394

Izumi M, Wada S, Makino A, Ishida H (2010) The autophagic degradation of chloroplasts via rubisco-containing bodies is specifically linked to leaf carbon status but not nitrogen status in Arabidopsis. Plant Physiol **154:** 1196-1209

Kohler RH, Cao J, Zipfel WR, Webb WW, Hanson MR (1997) Exchange of protein molecules through connections between higher plant plastids. Science **276:** 2039-2042

Kusano S, Nakamura S, Izumi M, Hagihara S (2023) A fluorescent molecular probe for live-cell imaging of starch granules. ChemRxib

Law SR, Chrobok D, Juvany M, Delhomme N, Linden P, Brouwer B, Ahad A, Moritz T, Jansson S, Gardestrom P, Keech O (2018) Darkened leaves use different metabolic strategies for senescence and survival. Plant Physiol **177:** 132-150

Lazarou M, Sliter DA, Kane LA, Sarraf SA, Wang CX, Burman JL, Sideris DP, Fogel AI, Youle RJ (2015) The ubiquitin kinase PINK1 recruits autophagy receptors to induce mitophagy. Nature **524:** 309-314.

Lee HN, Chacko JV, Solis AG, Chen KE, Barros JA, Signorelli S, Millar AH, Vierstra RD, Eliceiri KW, Otegui MS, Benitez-Alfonso Y (2023) The autophagy receptor NBR1 directs the clearance of photodamaged chloroplasts. Elife **12:** e86030.

Mae T, Kai N, Makino A, Ohira K (1984) Relation between ribulose bisphosphate carboxylase content and chloroplast number in naturally senescing primary leaves of wheat. Plant Cell Physiol **25:** 333-336

Makino A, Osmond B (1991) Effects of nitrogen nutrition on nitrogen partitioning between chloroplasts and mitochondria in pea and wheat. Plant Physiol **96:** 355-362

Martinoia E, Heck U, Dalling MJ, Matile P (1983) Changes in chloroplast number and chloroplast constituents in senescing barley leaves. Biochem Physiol Pfl **178:** 147-155

Matsui T, Jiang PD, Nakano S, Sakamaki Y, Yamamoto H, Mizushima N (2018) Autophagosomal YKT6 is required for fusion with lysosomes independently of syntaxin 17. J Cell Biol **217:** 2633-2645

Miyagishima SY, Froehlich JE, Osteryoung KW (2006) PDV1 and PDV2 mediate recruitment of the dynamin-related protein ARC5 to the plastid division site. Plant Cell **18:** 2517-2530

Mochida K, Oikawa Y, Kimura Y, Kirisako H, Hirano H, Ohsumi Y, Nakatogawa H (2015) Receptor-mediated selective autophagy degrades the endoplasmic reticulum and the nucleus. Nature **522:** 359-362

Mochida K, Otani T, Katsumata Y, Kirisako H, Kakuta C, Kotani T, Nakatogawa H (2022) Atg39 links and deforms the outer and inner nuclear membranes in selective autophagy of the nucleus. J Cell Biol **221:** e202103178

Nakagawa T, Suzuki T, Murata S, Nakamura S, Hino T, Maeo K, Tabata R, Kawai T, Tanaka K, Niwa Y, Watanabe Y, Nakamura K, Kimura T, Ishiguro S (2007) Improved Gateway binary vectors: high-performance vectors for creation of fusion constructs in transgenic analysis of plants. Bioscience, biotechnology, and biochemistry **71:** 2095-2100

Nakamura S, Hagihara S, Izumi M (2021a) Mitophagy in plants. BBA-Gen Subjects **1865:** 129916

Nakamura S, Hagihara S, Otomo K, Ishida H, Hidema J, Nemoto T, Izumi M (2021b) Autophagy contributes to the quality control of leaf mitochondria. Plant Cell Physiol **62:** 229–247

Nakamura S, Hidema J, Sakamoto W, Ishida H, Izumi M (2018) Selective elimination of membrane-damaged chloroplasts via microautophagy. Plant Physiol **177:** 1007-1026

Nakamura S, Izumi M (2018) Regulation of chlorophagy during photoinhibition and senescence: lessons from mitophagy. Plant Cell Physiol **59:** 1135-1143

Nakatogawa H (2020) Mechanisms governing autophagosome biogenesis. Nat Rev Mol Cell Bio **21:** 439-458

Oikawa K, Goto-Yamada S, Hayashi Y, Takahashi D, Kimori Y, Shibata M, Yoshimoto K, Takemiya A, Kondo M, Hikino K, Kato A, Shimoda K, Ueda H, Uemura M, Numata K, Ohsumi Y, Hara-Nishimura I, Mano S, Yamada K, Nishimura M (2022) Pexophagy suppresses ROS-induced damage in leaf cells under high-intensity light. Nat Commun **13:** 7493

Onishi M, Yamano K, Sato M, Matsuda N, Okamoto K (2021) Molecular mechanisms and physiological functions of mitophagy. EMBO J **40:** e104705.

Ono Y, Wada S, Izumi M, Makino A, Ishida H (2013) Evidence for contribution of autophagy to rubisco degradation during leaf senescence in *Arabidopsis thaliana*. Plant Cell Environ **36:** 1147-1159

Osteryoung KW, Pyke KA (2014) Division and dynamic morphology of plastids. Annu Rev Plant Biol **65:** 443-472

Otomo K, Hibi T, Murata T, Watanabe H, Kawakami R, Nakayama H, Hasebe M, Nemoto T (2015) Multi-point scanning two-photon excitation microscopy by utilizing a high-peak-power 1042-nm laser. Anal Sci **31:** 307-313

Pan T, Liu YX, Hu XF, Li PW, Lin CC, Tang YY, Tang W, Liu YS, Guo L, Kim C, Fang J, Lin HH, Wu ZH, Blumwald E, Wang SH (2023) Stress-induced endocytosis from chloroplast inner envelope membrane is mediated by CHLOROPLAST VESICULATION but inhibited by GAPC. Cell Rep **42:** 113208.

Phillips AR, Suttangkakul A, Vierstra RD (2008) The ATG12-conjugating enzyme ATG10 is essential for autophagic vesicle formation in *Arabidopsis thaliana*. Genetics **178:** 1339-1353

Pyke KA, Leech RM (1994) A Genetic-Analysis of Chloroplast Division and Expansion in *Arabidopsis thaliana*. Plant Physiol **104:** 201-207

Rambold AS, Kostelecky B, Elia N, Lippincott-Schwartz J (2011) Tubular network formation protects mitochondria from autophagosomal degradation during nutrient starvation. Proc Natl Acad Sci U S A **108:** 10190-10195

Sasaki T, Tsutsumi M, Otomo K, Murata T, Yagi N, Nakamura M, Nemoto T, Hasebe M, Oda Y (2019) A novel katanin-tethering machinery accelerates cytokinesis. Curr Biol **29:** 4060-+

Segami S, Makino S, Miyake A, Asaoka M, Maeshima M (2014) Dynamics of vacuoles and H+-pyrophosphatase visualized by monomeric green fluorescent protein in Arabidopsis:

1370 artifactual bulbs and native intravacuolar spherical structures. Plant Cell **26:** 3416-3434
1371 **Smith AM, Stitt M** (2007) Coordination of carbon supply and plant growth. Plant Cell Environ
1372 **30:** 1126-1149.
1373 **Spitzer C, Li FQ, Buono R, Roschzttardtz H, Chung TJ, Zhang M, Osteryoung KW,**
1374 **Vierstra RD, Otegui MS** (2015) The endosomal protein CHARGED
1375 MULTIVESICULAR BODY PROTEIN1 regulates the autophagic turnover of plastids
1376 in Arabidopsis. Plant Cell **27:** 391-402
1377 **Svenning S, Lamark T, Krause K, Johansen T** (2011) Plant NBR1 is a selective autophagy
1378 substrate and a functional hybrid of the mammalian autophagic adapters NBR1 and
1379 p62/SQSTM1. Autophagy **7:** 993-1010.
1380 **Thompson AR, Doelling JH, Suttangkakul A, Vierstra RD** (2005) Autophagic nutrient
1381 recycling in Arabidopsis directed by the ATG8 and ATG12 conjugation pathways. Plant
1382 Physiol **138:** 2097-2110
1383 **Tsuboyama K, Koyama-Honda I, Sakamaki Y, Koike M, Morishita H, Mizushima N**
1384 (2016) The ATG conjugation systems are important for degradation of the inner
1385 autophagosomal membrane. Science **354:** 1036-1041
1386 **Twig G, Elorza A, Molina AJA, Mohamed H, Wikstrom JD, Walzer G, Stiles L, Haigh SE,**
1387 **Katz S, Las G, Alroy J, Wu M, Py BF, Yuan J, Deeney JT, Corkey BE, Shirihai OS**
1388 (2008) Fission and selective fusion govern mitochondrial segregation and elimination
1389 by autophagy. EMBO J **27:** 433-446
1390 **Vitha S, Froehlich JE, Koksharova O, Pyke KA, van Erp H, Osteryoung KW** (2003) ARC6
1391 is a J-domain plastid division protein and an evolutionary descendant of the
1392 cyanobacterial cell division protein Ftn2. Plant Cell **15:** 1918-1933
1393 **Wada S, Ishida H, Izumi M, Yoshimoto K, Ohsumi Y, Mae T, Makino A** (2009) Autophagy
1394 plays a role in chloroplast degradation during senescence in individually darkened
1395 leaves. Plant Physiol **149:** 885-893
1396 **Wan C, Zhang H, Cheng HY, Sowden RG, Cai WJ, Jarvis RP, Ling QH** (2023) Selective
1397 autophagy regulates chloroplast protein import and promotes plant stress tolerance.
1398 EMBO J **42:** e112534.
1399 **Wang SH, Blumwald E** (2014) Stress-induced chloroplast degradation in Arabidopsis is
1400 regulated via a process independent of autophagy and senescence-associated vacuoles.
1401 Plant Cell **26:** 4875-4888.
1402 **Wang WH, Li JY, Sun QQ, Yu XY, Zhang WW, Jia N, An CJ, Li YQ, Dong YN, Han FJ,**
1403 **Chang N, Liu XM, Zhu ZL, Yu Y, Fan SL, Yang MJ, Luo SZ, Gao HB, Feng Y**
1404 (2017) Structural insights into the coordination of plastid division by the ARC6-PDV2
1405 complex. Nat Plants **3:** 17011
1406 **Weaver LM, Amasino RM** (2001) Senescence is induced in individually darkened Arabidopsis
1407 leaves but inhibited in whole darkened plants. Plant Physiol **127:** 876-886
1408 **Yamashita S, Jin XL, Furukawa K, Hamasaki M, Nezu A, Otera H, Saigusa T, Yoshimori**
1409 **T, Sakai Y, Mihara K, Kanki T** (2016) Mitochondrial division occurs concurrently
1410 with autophagosome formation but independently of Drp1 during mitophagy. J Cell
1411 Biol **215:** 649-665
1412 **Yoshimoto K, Hanaoka H, Sato S, Kato T, Tabata S, Noda T, Ohsumi Y** (2004) Processing
1413 of ATG8s, ubiquitin-like proteins, and their deconjugation by ATG4s are essential for
1414 plant autophagy. Plant Cell **16:** 2967-2983
1415 **Yoshimoto K, Jikumaru Y, Kamiya Y, Kusano M, Consonni C, Panstruga R, Ohsumi Y,**
1416 **Shirasu K** (2009) Autophagy negatively regulates cell death by controlling NPR1-
1417 dependent salicylic acid signaling during senescence and the innate immune response in
1418 *Arabidopsis*. Plant Cell **21:** 2914-2927
1419 **Yoshimoto K, Ohsumi Y** (2018) Unveiling the molecular mechanisms of plant autophagy-from
1420 autophagosomes to vacuoles in plants. Plant Cell Physiol **59:** 1337-1344

1421